Alma Mater Studiorum – Università di Bologna

DOTTORATO DI RICERCA IN

Meccanica e Scienze Avanzate dell'Ingegneria

Ciclo XXVII

Settore Concorsuale di afferenza: 09/C2

Settore Scientifico disciplinare: ING-IND/18

MODELLING, DIAGNOSTICS AND EXPERIMENTAL ANALYSIS OF PLASMA ASSISTED PROCESSES FOR MATERIAL TREATMENT

Presentata da: Marco Boselli

Coordinatore Dottorato

Prof. Vincenzo Parenti Castelli

Relatori

Prof. Vittorio Colombo
Prof. Emanuele Ghedini

Esame finale anno 2015

Index

Introduction

Atmospheric pressure plasmas have an important role in several industrial processes, from plasma arc torches for cutting and welding of metals to the synthesis of enhanced value materials such as nanopowders. Plasma systems have usually a high degree of freedom in operating conditions and setups in order to accomplish optimal performances. Nonetheless many processes cannot be easily controlled or characterized, due to usual high temperatures, micro-second phenomena and high velocity fields. In order to investigate these plasmas many advanced diagnostics techniques can be used, such as high speed imaging, optical emission spectroscopy and Schlieren imaging. These methods can give strong insights on these processes but there are still many parameters that cannot be monitored. Therefore an analysis through computational thermo-fluid-dynamics modelling of such processes is nowadays the only method to recover such parameters. The combined practice of diagnostics and modelling is an acknowledged tool for design and optimization of industrial processes.

In this thesis are presented some of the works developed during my three years of Ph.D. into the Research Group for Industrial Applications of Plasmas of University of Bologna and AlmaPlasma S.r.l.. Activities have been performed into the framework of research contracts with companies such as Umicore Research (BE), AirLiquide-CTAS (FR) and Cebora (IT). They have also been performed into the framework of FP7-NMP European project SIMBA “Scaling-up of ICP technology for continuous production of Metallic nanopowders for Battery Applications”, European networking projects MPNS COST Action MP1101 “Bio-Plasma - Biomedical Applications of Atmospheric Pressure Plasma Technology” and MPNS COST Action TD1208 “Electrical discharges with liquids for future applications”.

This work presents results from experimental investigations of several different atmospheric pressure plasmas applications, such as Metal Inert Gas (MIG) welding and Plasma Arc Cutting (PAC) and Welding (PAW) sources, as well as Inductively Coupled Plasma (ICP) torches. The main diagnostic tool that has been used is High Speed Imaging (HSI), often assisted by Schlieren imaging to analyse non-visible phenomena. Furthermore, starting from thermo-fluid-dynamic models developed by the University of Bologna group, such plasma processes have been studied also with new advanced models, focusing for instance on the interaction between a melting metal wire and a plasma, or considering non-equilibrium phenomena for diagnostics of plasma arcs.

Some of the results here described have been presented in the following papers:

- M. Boselli, V. Colombo, E. Ghedini, M. Gherardi, P. Sanibondi, *"Dynamic analysis of droplet transfer in GMAW: modelling and experiments"*, Plasma Sources Science and Technology (2012)
- V. Colombo, A. Concetti, E. Ghedini, F. Rotundo, P. Sanibondi, M. Boselli, S. Dallavalle, M. Gherardi, V. Nemchinsky, M. Vancini, *"Advances in Plasma Arc Cutting Technology: the Experimental Part of an Integrated Approach"*, Plasma Chemistry and Plasma Processing (2012)
- M. Boselli, V. Colombo, E. Ghedini, M. Gherardi, P. Sanibondi, *"Two-temperature modelling and optical emission spectroscopy of a constant current plasma arc welding process*" J. Phys. D: Appl. Phys. 46 224009 (2013)
- M. Boselli, V. Colombo, E. Ghedini, M. Gherardi, P. Sanibondi, *"Two-dimensional time-dependent modelling of fume formation in a pulsed gas metal arc welding process*" J. Phys. D: Appl. Phys. 46 224006 (2013)
- M. Boselli, V. Colombo, E. Ghedini, M. Gherardi, F. Rotundo, P. Sanibondi, "*High-speed imaging investigation of transient phenomena impacting plasma arc cutting process optimization*" J. Phys. D: Appl. Phys. 46 224010 (2013)
- M. Boselli, V. Colombo, E. Ghedini, M. Gherardi, F. Rotundo, P. Sanibondi, "*Investigation of Thermal Nonequilibrium in a Plasma Arc Welding Process: Modeling and Diagnostics*", IEEE Transactions on Plasma Science (2014)

and in the following congresses:

- Boselli M, Colombo V, Ghedini E, Gherardi M, Sanibondi P, Delval C, Jaeggi C, Leparoux M, Put S, Nelis D, Caillon G, Jordy C, *"Radio-frequency induction thermal plasma system for continuous production of silicon nanopowders for battery application"*, oral presentation at NanotechItaly 2012, Venice, Italy, 21-23 November 2012
- Boselli M, Colombo V, Daniëls N, Delval C, Ghedini E, Gherardi M, Jaeggi C, Leparoux M, Put S, Sanibondi P, "*Influence of processing parameters on the properties of silicon nanoparticles synthesized by radio-frequency induction thermal plasma"*, oral presentation at ICOPS 2012, Edinburgh, Scotland, 8-12 July 2012
- Boselli M, Colombo V, Daniëls N, Delval C, Ghedini E, Gherardi M, Jaeggi C, Leparoux M, Put S, Sanibondi P, "*Influence of processing parameters on the properties of silicon nanoparticles synthesized by radio-frequency induction thermal plasma"*, oral presentation at HTPP12, Bologna, Italia, 24-29 June 2012
- Boselli M, Colombo V, Ghedini E, Gherardi M, Sanibondi P, "*Two-temperature modelling and optical emission spectroscopy of a constant current plasma arc welding process"*, invited oral presentation at PPPS2013, San Francisco (CA), USA, 16-21 June 2013
- Boselli M, Colombo V, Ghedini E, Gherardi M, Sanibondi P, "*Two-dimensional time-dependent modelling of fume formation in a pulsed gas metal arc welding*

process", oral presentation at PPPS2013, San Francisco (CA), USA, 16-21 June 2013

- Boselli M, Colombo V, Ghedini E, Gherardi M, Sanibondi P, "*Three-dimensional modeling of silicon nanoparticles synthesis in the downstream region of a dc non-transferred arc plasma torch*", poster presentation at PPPS2013, San Francisco (CA), USA, 16-21 June 2013
- Boselli M, Colombo V, Ghedini E, Gherardi M, Rotundo F, Sanibondi P, "*Comparison between net emission coefficient and P-1 methods in modelling radiation in a plasma arc welding torch*", poster presentation at PPPS2013, San Francisco (CA), USA, 16-21 June 2013
- Boselli M, Colombo V, Ghedini E, Gherardi M, Sanibondi P, "*Modelling of Si nanoparticle synthesis by inductively coupled thermal plasma: optimization of curtain gas injection in a conical reaction chamber*", poster presentation at PPPS2013, San Francisco (CA), USA, 16-21 June 2013
- Boselli M, Colombo V, Ghedini E, Gherardi M, Lo Iacono F, Rotundo F, Sanibondi P, Traldi E, "*Control of nanoparticle size in RF thermal plasma synthesis of silicon oxide starting from solid and liquid precursors*", poster presentation at ISPC21, Cairns, Australia, 4-9 August 2013
- Boselli M, Colombo V, Ghedini E, Gherardi M, Sanibondi P, "*Prediction of fume formation in a pulsed gas metal arc welding process by means of a 2D time-dependent arc model coupled with nanoparticle tracking*", oral presentation at ISPC21, Cairns, Australia, 4-9 August 2013
- Boselli M, Colombo V, Ghedini E, Gherardi M, Rotundo F, Sanibondi P, "*High-speed imaging investigation of transient phenomena impacting plasma arc cutting process optimization*", poster presentation at ISPC21, Cairns, Australia, 4-9 August 2013
- Boselli M, Colombo V, Ghedini E, Gherardi M, Rotundo F, Sanibondi P, "*Experimental investigation on the effects of the gas mixtures in plasma arc cutting of stainless steel*", poster presentation at ISPC21, Cairns, Australia, 4-9 August 2013
- Boselli M, Colombo V, Ghedini E, Gherardi M, Sanibondi P, "*Investigation of Silicon nanoparticles synthesis in the downstream region of a DC non-transferred arc plasma torch by three-dimensional modelling*", poster presentation at ISPC21, Cairns, Australia, 4-9 August 2013
- Boselli M, Colombo V, Ghedini E, Gherardi M, Sanibondi P, "*Optimization of curtain gas injection position and flow rate in a conical reaction chamber for Si nanoparticle synthesis by inductively coupled thermal plasmas*", poster presentation at ISPC21, Cairns, Australia, 4-9 August 2013
- Boselli M, Colombo V, Ghedini E, Gherardi M, Sanibondi P, "*Modelling for the optimization of the reaction chamber in silicon nanoparticle synthesis by a radio-frequency induction thermal plasma*", oral presentation at ISPC21, Cairns, Australia, 4-9 August 2013
- Boselli M, Colombo V, Ghedini E, Gherardi M, Sanibondi P, "*Investigation of a constant current plasma arc welding process by means of two-temperature modelling and optical emission spectroscopy*", oral presentation at ISPC21, Cairns, Australia, 4-9 August 2013
- Boselli M, Ceschini L, Colombo V, Ghedini E, Gherardi M, Morri A, Rotundo F, Sanibondi P, Toschi S, "*RF inductively coupled thermal plasma synthesis of ceramic nanoparticles for the production of Al-based metal matrix*

nanocomposites", poster presentation at ISPC21, Cairns, Australia, 4-9 August 2013

- Boselli M, Carotti F, Colombo V, Ghedini E, Gherardi M, Keszler A M, Klebert Sz, Karoly Z, Sanibondi P, "*Influence of reaction chamber geometry on fullerene synthesis in RF inductively coupled thermal plasmas*", oral presentation at CESPC5, Balatonalmádi, Hungary, 25-29 August 2013
- Boselli M, Ceschini L, Colombo V, Ghedini E, Gherardi M, Morri A, Rotundo F, Sanibondi P, Toschi S, *"Cast Al-based nanocomposites reinforced with thermal plasma--synthesized ceramic nanoparticles"*, poster presentation to be presented at THERMEC 2013, Las Vegas, USA, 2-6 December 2013
- Balestri G, Boselli M, Carotti F, Colombo V, Ghedini E, Gherardi M, Keszler A M, Klebert Sz, Karoly Z, Sanibondi P, *"Fullerene synthesis in radio-frequency inductively coupled thermal plasmas"*,oral presentation at High-tech Plasma Processes 13 - (HTPP13) – 22-27 giugno 2014, Tolouse, France

Additionally, the experimental diagnostic tools that have been developed for industrial thermal plasmas have been used also for the characterization of innovative low temperature atmospheric pressure non equilibrium plasmas, such as dielectric barrier discharges (DBD) and Plasma Jets. These sources are controlled by few kV voltage pulses with pulse rise time of few nanoseconds to avoid the formation of a plasma arc, with interesting applications in surface functionalization of thermosensitive materials. In order to investigate also bio-medical applications of thermal plasma, a self-developed quenching device has been connected to an ICP torch. Such device has allowed inactivation of several kinds of bacteria spread on petri dishes, by keeping the substrate temperature lower than 40 degrees, which is a strict requirement in order to allow the treatment of living tissues.
The activities on these sources have brought to the deposit of two patents:

- V. Colombo et al., "*Device and methods for generating reactive species by means of a plasma at atmospheric pressure*", WO2015019240, Università di Bologna (2015)
- V. Colombo et al., "*Apparato di disinfezione di apparecchi elettronici portatili mediante plasma*", BO2014A000502, AlmaPlasma s.r.l. (2014)

In addition on that, results have been presented in the following papers:

- M. Boselli, V. Colombo, E. Ghedini, M. Gherardi, R. Laurita, A. Liguori, P. Sanibondi, A. Stancampiano, "*High-Speed Multi-Imaging of Repetitive Unipolar Nanosecond-Pulsed DBDs*", IEEE Transactions on Plasma Science – 7th Triennial special issue on Images in Plasma Science (2014)
- M. Boselli, F. Cavrini, V. Colombo, E. Ghedini, M. Gherardi, R. Laurita, A. Liguori, P. Sanibondi, A. Stancampiano, "*High-speed and Schlieren imaging of a low power inductively coupled plasma source for potential biomedical applications"*, IEEE Transactions on Plasma Science – 7th Triennial special issue on Images in Plasma Science (2014)

- M. Boselli, V. Colombo, E. Ghedini, M. Gherardi, R. Laurita, A. Liguori, P. Sanibondi, A. Stancampiano, *"Schlieren High-Speed Imaging of a Nanosecond Pulsed Atmospheric Pressure Non-equilibrium Plasma Jet*", Plasma Chemistry and Plasma Processing, 1-17 (2014)
- M. Boselli, V. Colombo, M. Gherardi, R. Laurita, A. Liguori, P. Sanibondi, E. Simoncelli, A. Stancampiano, *"Characterization of a cold atmospheric pressure plasma jet device driven by nanosecond voltage pulses",* IEEE Trans. Plasma Sci., Special issue on Atmospheric Pressure Plasma Jets and their Applications, (2015)

and to these international conferences:

- Boselli M, Colombo V, Ghedini E, Gherardi M, Laurita R, Sanibondi P, *"Optimization oriented characterization of a dual gas plasma needle device for biomedical applications: effluent composition, thermal output and fluid dynamics"*, poster presentation at GRC - Plasma Processing Science and Societal Grand Challenges, Bryant University, Smithfield, USA, 22-27 July 2012
- Boselli M, Colombo V, Ghedini E, Gherardi M, Laurita R, Sanibondi P, *"Optimization oriented characterization of a dual gas plasma needle device for biomedical applications: effluent composition, thermal output and fluid dynamics"*, oral presentation at GRS - Plasmas in Biology and Medicine, Plasma Processing and Plasma Analysis and Diagnostics, Bryant University, Smithfield, USA, 22-27 July 2012
- Boselli M, Colombo V, Ghedini E, Gherardi M, Laurita R, Rotundo F, Sanibondi P, *"Multi-imaging techniques for the characterization of a nanopulsed DBD system for biomedical applications"*, oral presentation at GRS - Plasmas in Biology and Medicine, Plasma Processing and Plasma Analysis and Diagnostics, Bryant University, Smithfield, USA, 22-27 July 2012
- Boselli M, Colombo V, Ghedini E, Gherardi M, Laurita R, Liguori A, Rotundo, Sanibondi P, Stancampiano A, *"Fluid-dynamic characterization of atmospheric pressure non-equilibrium plasma sources for biomedical applications"*, poster presentation at ICOPS 2012, Edinburgh, Scotland, 8-12 July 2012
- Boselli M, Colombo V, De Angelis M G, Ghedini E, Gherardi M, Laurita R, Minelli M, Rotundo F, Sanibondi P, Stancampiano A, *"Comparing the effects of different atmospheric pressure non-equilibrium plasma sources on PLA oxygen permeability"*, poster presentation at ICOPS 2012, Edinburgh, Scotland, 8-12 July 2012
- Boselli M, Colombo V, Ghedini E, Gherardi M, Laurita R, Liguori A, Rotundo F, Sanibondi P, Stancampiano A, *"Multi-imaging techniques for the characterization of a nanopulsed DBD system for biomedical applications"*, oral presentation at HTPP12, Bologna, Italia, 24-29 June 2012
- Boselli M, Colombo V, Ghedini E, Gherardi M, Laurita R, Liguori A, Sanibondi P, Stancampiano A, *"Fluid-dynamic characterization of atmospheric pressure non-equilibrium plasma sources for biomedical applications"*, poster presentation at HTPP12, Bologna, Italia, 24-29 June 2012
- Boselli M, Colombo V, De Angelis M G, Ghedini E, Gherardi M, Laurita R, Minelli M, Sanibondi P, Stancampiano A, *"Comparing the effects of different*

atmospheric pressure non-equilibrium plasma sources on PLA oxygen permeability", poster presentation at HTPP12, Bologna, Italia, 24-29 June 2012

- Boselli M, Colombo V, Ghedini E, Gherardi M, Laurita R, Liguori A, Sanibondi P, Stancampiano A, *"Transition from non-uniform to uniform discharge in nanosecond pulsed FE-DBD and linear corona non-equilibrium plasmas"*, poster presentation at HTPP12, Bologna, Italia, 24-29 June 2012
- Boselli M, Colombo V, Ghedini E, Gherardi M, Laurita R, Liguori A, Sanibondi P, Stancampiano A, *"Effluent composition, thermal output and fluid-dynamics of a dual gas plasma needle device for biomedical applications: Part II"*, poster presentation at HTPP12, Bologna, Italia, 24-29 June 2012
- Boselli M, Colombo V, Ghedini E, Gherardi M, Laurita R, Liguori A, Sanibondi P, Stancampiano A, *"Effluent composition, thermal output and fluid-dynamics of a dual gas plasma needle device for biomedical applications: Part I"*, poster presentation at HTPP12, Bologna, Italia, 24-29 June 2012
- Boselli M, Colombo V, Ghedini E, Gherardi M, Laurita R, Liguori A, Rotundo F, Sanibondi P, Stancampiano A, *"Multi-imaging techniques for the characterization of a nanopulsed DBD system for biomedical applications"*, oral presentation at 5P Plasma Processes: Past. Present and Perspectives, Bari, Italia, 21-23 June 2012
- Boselli M, Colombo V, Ghedini E, Gherardi M, Laurita R, Liguori A, Rotundo F, Sanibondi P, Stancampiano A, *"Effluent composition, thermal output and fluid-dynamics of a dual gas plasma needle device for biomedical applications: Part I"*, poster presentation at ICPM4, Orléans, France, 17-21 June 2012
- Boselli M, Colombo V, Ghedini E, Gherardi M, Laurita R, Liguori A, Rotundo F, Sanibondi P, Stancampiano A, *"Effluent composition, thermal output and fluid-dynamics of a dual gas plasma needle device for biomedical applications: Part II"*, poster presentation at ICPM4, Orléans, France, 17-21 June 2012
- Boselli M, Colombo V, Ghedini E, Gherardi M, Laurita R, Liguori A, Rotundo F, Sanibondi P, Stancampiano A, *"Transition from non-uniform to uniform discharge in nanosecond pulsed FE-DBD and linear corona non-equilibrium plasmas"*, poster presentation at ICPM4, Orléans, France, 17-21 June 2012
- Boselli M, Chiavari C, Colombo V, Ghedini E, Gherardi M, martini C, Rotundo F, Sanibondi P, "*Cleaning of 19th century daguerreotypes by means of atmospheric pressure cold plasma jet*", poster presentation at PPPS2013, San Francisco (CA), USA, 16-21 June 2013
- Boselli M, Chiavari C, Colombo V, Ghedini E, Gherardi M, Martini C, Rotundo F, Sanibondi P, *"Atmospheric pressure non-thermal plasma cleaning of 19th century daguerreotypes*", poster presentation at ISPC21, Cairns, Australia, 4-9 August 2013
- Boselli M, Colombo V, Gherardi M, Laurita R, Liguori A, Sanibondi P, Stancampiano A, "*High speed imaging characterization of a Dielectric Barrier Discharge Roller plasma source*", poster presentation at ISPC21, Cairns, Australia, 4-9 August 2013
- Boselli M, Colombo V, Gherardi M, Laurita R, Liguori A, Sanibondi P, Stancampiano A, "*Characterization of a plasma jet for biomedical applications: composition, temperature, fluid dynamics and plasma structure*", poster presentation at ISPC21, Cairns, Australia, 4-9 August 2013
- Boselli M, Colombo V, Gherardi M, Laurita R, Liguori A, Sanibondi P, Stancampiano A, *"Study of the role of dielectric material in a dielectric barrier*

discharge (DBD) plasma source for dermatological application", poster presentation at ISPC21, Cairns, Australia, 4-9 August 2013

- Boselli M, Chiavari C, Colombo V, Ghedini E, Gherardi M, Martini C, Rotundo F, Sanibondi P, *"Corrosion of daguerreotypes: atmospheric pressure non-thermal plasma for the reduction of silver tarnish"*, poster presentation at EUROCORR 2013, Estoril, Portugal, 1-5 September 2013
- Barbieri D, Boselli M, Cavrini F, Colombo V, Gherardi M, Landini M P, Laurita R, Liguori A, Sanibondi P, Stancampiano A, *Investigation of the effectiveness of a low power inductively coupled plasma source for biomedical application,* invited presentation at ICPM5, Nara, Japan, May 2014
- Boselli M, Colombo V, Gherardi M, Laurita R, Liguori A, Sanibondi P, Stancampiano A, *"Diagnostic of a low power inductively coupled plasma source for biomedical applications"* poster presentation ICPM5, Nara, Japan, May 2014
- Anceschi G, Barbieri D, Boselli M, Cavrini F, Colombo V, Gherardi M, Landini M P, Laurita R, Liguori A, Sanibondi P, Stancampiano A, *"Antimicrobial activity of a low power inductively coupled plasma at safe levels for eukaryotic cells,* poster presentation ICPM5, Nara, Japan, May 2014
- Barbieri D, Boselli M, Cavrini F, Colombo V, Gherardi M, Landini M P, Laurita R, Liguori A, Sanibondi P, Stancampiano *"Non-equilibrium plasma sources and processes with a focus on antibacterial applications and sterilization",* keynote lecture at 14th International conference on plasma surface Engineering, Garmisch- Partenkirchen, Germany, September 2014

CHAPTER 1
Gas metal arc welding process: experiments and modelling of droplet transfer and fume formation

1. Volume of fluid method: melted wire shape tracking

1.1 Introduction

Gas-metal arc welding (GMAW) [1, 2] is a long-established process used for joining metals, as mild or stainless steel and aluminium. Main process parameters are the arc current time-profile, the total voltage, the wire-feeding rate, the shielding gas flow rate, the welding speed, the wire diameter and material. Depending on the combination of these parameters, the metal transfer to the workpiece can be obtained in different modes: globular, spray, pulsed and short-circuit [3-6].
Both modelling and experimental activities play an important role in the optimization of GMAW: the first highlights fundamental processes occurring during metal transfer, which can give insights on the optimal design of the experiments [7-10]; the second is essential to test several combinations of operating conditions and to check the overall quality of the process, for instance the insurgence of welding sputter [11-19]. Thermo-fluid-dynamic modelling plays an important role in understanding the relative importance of different operating conditions of GMAW and in highlighting physical phenomena acting during metal transfer (Lorentz forces, surface tension, plasma fluid-dynamics, metal vapour diffusion, etc.) [20-25].
It has been recently shown [26] that vapours coming from the over-heated wire tip can greatly influence the arc behaviour, with an increased radiation emission that results in an increased cooling of the arc at the centreline. The most advanced models for GMAW include either the time-dependent droplet detachment surface tracking through volume-of-fluid (VoF) approach [27], or the accurate description of the metal vapour diffusion process under steady-state conditions (fixed wire shape), taking into account demixing effects using the combined diffusion approach developed by Murphy [26].
In a previous work by the Authors [28], a time-dependent axi-symmetric 2-D model has been developed in the FLUENT environment to take into account both the droplet detachment using a VoF model as well as the production and diffusion of metal vapour through a simplified diffusion model (neglecting demixing effects). In this work it has been applied to the case of the pulsed welding process. Besides modelling, the same process has been recorded using high-speed camera to validate the modelling results and study the overall dynamics of the metal transfer. This integrated approach gives new insights in understanding pulsed GMAW and it can be used as the basis of an efficient tool to optimize the process. The results presented in the following pages have been published in [29].

1.2 Experimental setup

A shadowgraph setup (figure 1) composed by a high speed camera (NAC K3) and a DC operated Xenon Short Arc Lamp have been used to study the droplet transfer obtained by means of a welding torch linked to a pulsed welding power source (Cebora SOUND MIG 5040/TD DOUBLE PULSE). The lamp operates in a continuous-output mode, allowing the tracking of the shadows of solid and liquid metal even in presence of the strong plasma arc light emission.

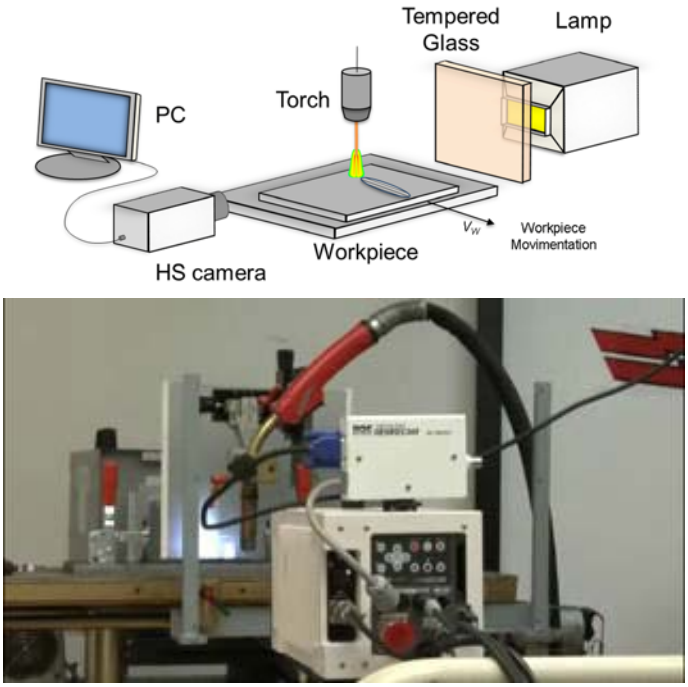

Figure 1 Schematic and picture of the experimental setup. [29]

Metal droplets have been continuously transferred on a mild steel workpiece 3 mm in thickness. To avoid piercing or metal accumulation on the workpiece and to reproduce a setup similar to common robot welding, the workpiece has been moved sideways to the high-speed camera at a constant speed of 0.8 m/min. A sheet of tempered glass has been used to protect the lamp from welding spatter with low impact on light dampening The experiment was performed with a wire feed rate of 5 m/min and a mild steel SG2 wire of 1 mm diameter. The distance between the surface of the workpiece and the contact tip of the torch was nearly 15 mm, with granted an average arc length of 4 mm and a stick out length of 11 mm. As shielding gas it was used argon with a constant flow rate of 10 l/min. The pulsed current waveform [30] used for experiment had a period of 9 ms, with peaks of current of nearly 360 A and a background current of 30 A. The high-speed camera video was shot with a frequency of 8000 fps, 1/20000 s shutter time and with the aid of some neutral density filter.

1.3 Modelling approach

The model implies the solution of the following equations:

Mass continuity

$$\frac{\partial \rho}{\partial t} + \nabla \cdot (\rho \vec{u}) = 0 \tag{1.1}$$

Momentum conservation

$$\frac{\partial \rho \vec{u}}{\partial t} + \nabla \cdot (\rho \vec{u}\vec{u}) = -\nabla p + \nabla \cdot \bar{\bar{\tau}} + \rho \vec{g} + \vec{j} \times \vec{B} + \vec{F}_S - K\vec{u} \tag{1.2}$$

Energy conservation

$$\frac{\partial \rho e}{\partial t} + \nabla \cdot \left((\rho e + p)\vec{u}\right) = \nabla \cdot (k \nabla T) + \vec{j} \cdot \vec{E} - Q_{rad} + S \tag{1.3}$$

Metal vapour mass conservation

$$\frac{\partial \rho y_{VAP}}{\partial t} + \nabla \cdot (\vec{u} \rho y_{VAP}) = \nabla \cdot \rho D_{VAP} \nabla y_{VAP} + S_{vap} \tag{1.4}$$

Volume of fluid conservation

$$\frac{\partial F}{\partial t} + \vec{u} \cdot \nabla F = 0 \tag{1.5}$$

where ρ is the plasma density, t is the time, $\vec{u}$ is the velocity vector, p is the pressure, $\bar{\bar{\tau}}$ is the viscous stress tensor, $\vec{j}$ is the current density, $\vec{B}$ is the magnetic induction, $\vec{g}$ is the gravitational force, e is the specific energy, k is the thermal conductivity, T is the temperature, $\vec{E}$ is the electric field, y_{VAP} is the metal vapour concentration, D_{VAP} is the metal vapour diffusivity, Q_{rad} is the energy loss by radiation, S_{vap} is the production of metal vapour from liquid surfaces and F is the volume of fluid fraction..

The presence of both plasma and metal is taken into account by adding different source terms for momentum and energy equations. $\vec{F}_S$ represents the forces acting on the surface of the liquid, which are the surface tension force and the Marangoni force [31]. K is function of metal temperature that represents the drag term during melting phase [27].
The energy source term S for the surface of the metal includes electron heating due to the work function of metal and radiative cooling using Stefan Boltzmann law [32] and an emission coefficient of 0.25. The latent heat of fusion is considered through variations of liquid fraction ratio. The source term for the plasma includes radiation losses and Thomson effect.

Diffusion of metal vapour from the molten metal has been taken in account using a simplified diffusion model, allowing the use of plasma properties weighted on the mass fraction of shielding gas and metal vapour. The production of metal vapour S_{VAP} has been self-consistently calculated on the surface of the wire through the net vapour mass flux J_{VAP} at the liquid-gas interface on anode, on cathode and on detached droplets using Hertz-Knudsen-Langmuir equation [2,33],

$$J_{VAP} = \left(\frac{m_{METAL}}{2\pi k_{BOL} T_{METAL}} \right)^{0.5} P_{VAP} \tag{1.6}$$

where m_{METAL} is the atomic mass of the metal material, k_{BOL} is the Boltzmann's constant, T_{METAL} is the metal surface temperature and P_{VAP} is the metal vapour pressure.
Additionally J_{VAP} is used to add the heat of vaporization cooling effect into the energy conservation equation; to grant a stable cathode arc attachment it is imposed on the workpiece an exponential temperature profile [21]

$$T(r) = 2700 \cdot e^{-\left(\frac{r}{1.4 \cdot R_{wire}}\right)^3} + 300 \tag{1.7}$$

where r is the distance from the axis of symmetry and R_{wire} is the radius of the metal wire. This temperature distribution allows us to add an imposed vapour mass flow on the workpiece. On all the other surfaces the temperature is fixed at 300 K with imposed zero diffusive flow of metal vapour. Zero metal vapour concentration is imposed on both shield gas inlet and outlet surfaces. The initial iron mass fraction was zero in the whole domain. Turbulent effects on flow have been neglected. An Argon flow rate of

10 l/min is imposed at the shield gas inlet. The boundary condition for the inlet of solid metal is set to a constant speed of 5 m/min.
The electromagnetic field equations have been solved in their vector potential form *A* using the extended field approach [34]:

$$\nabla \cdot \sigma \nabla V = 0 \tag{1.8}$$

$$\vec{E} = -\nabla V \tag{1.9}$$

$$\nabla^2 \vec{A} - \mu_0 \sigma \vec{E} = 0 \tag{1.10}$$

$$\vec{B} = \nabla \times \vec{A} \tag{1.11}$$

where σ is the electrical conductivity, V is the electric potential and μ_0 is the vacuum permeability.
As a function of the time-dependent current I a uniform profile of current flux j on the wire inlet section (ϕ = 1 mm) is given as a boundary condition using the relation:

$$j(t) = \frac{I(t)}{\frac{\pi}{4}\phi^2} \tag{1.12}$$

On the workpiece surface, that works as cathode, the electrical potential is assumed to be zero, while on all the other surfaces of the model the current flux is assumed to be zero. A=0 as boundary condition on the side of the outlet surface is fixed, with no flux on all the other boundaries.
Thermodynamic and transport properties of pure argon and iron vapours have been computed using fourth order Chapman-Enskog method [35], whereas radiative emission losses data for pure gases have been taken from [26]. Properties for different Ar-Fe mixtures have calculated using mixing rules [36]. Temperature dependent density of molten mild steel has been implemented in the model, whereas other properties have been assumed constant [27]. Even if a constant surface tension value has been used for surface tension force calculation, the Marangoni effect has been taken into account by evaluating the temperature gradient along the surface of the liquid and assuming a linear dependence of the liquid iron surface tension on the temperature.
In figure. 2 a schematic of the computational domain is displayed.

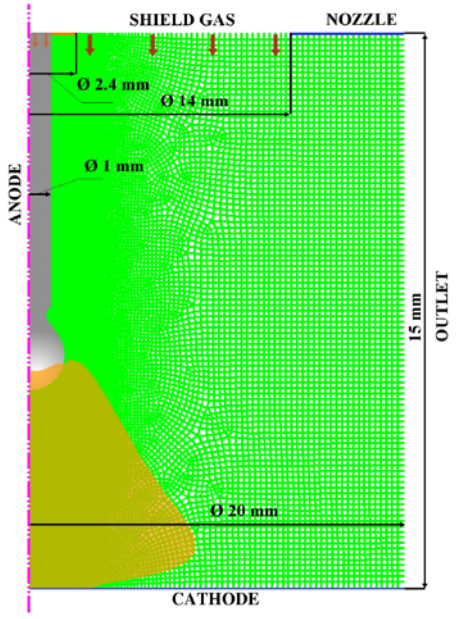

Figure 2 Schematic of computational domain (dimensions in mm). [29]

1.4 Results

Numerical simulation have been executed in the FLUENT environment on the same operating conditions of the experimental setup: a steel wire with a 1 mm diameter fed at a 5 m/min rate, with a 10 l/min flow rate of argon and the same experimental current profile (figure 3). If the electric pulse is well tuned, after a transient start-up of some tens of pulses, the droplet detachment and metal transfer assumes a periodic behaviour. Results for a single droplet transfer in the periodic behaviour obtained after more than one hundred pulses are reported. Results for the temperature and iron mass fraction fields at different time steps are reported (figures 4-6). On top right of each picture a high speed image of the process at the same relative time step from the beginning of the pulse and with the same electric current of the numerical simulation can be used for comparisons. Time step (a), which is shown in figure. 4, is characterized by a current of 30 A with overall low iron vapour concentration. In this phase, a temperature peak on the axis has been obtained because of the low values of iron mass fraction. In figure 5 it is shown that with 360 A of current there is a massive increase in iron vapour concentration along the axis of the discharge, due to both a temperature on the surface of the wire close to boiling point (≈3100 K) which increases vapour production and to an increase of plasma axial velocity due to magnetic pumping [26]. The off-axis displacement of the maximum in temperature could be explained by the increase of radiative dissipation due to iron vapour concentration [2] in the region close to anode surface. In the axis region, the saturation of iron vapour is almost reached, whereas in the maximum temperature region vapour concentration is approximately one order of magnitude lower. Figure 6 shows that even with a lower current (180 A), half compared to the 360 A of the peak, in frame (d) the droplet has been stretched enough to obtain afterwards the detachment, as it can be seen in frame (e). Even with lower currents the production of metal vapour is kept high by the increase in the surface of the liquid metal, both before and after the detachment. A comparison with the experimental images in the top right of each frame shows that the overall dynamic behaviour of the droplet detachment is well represented.

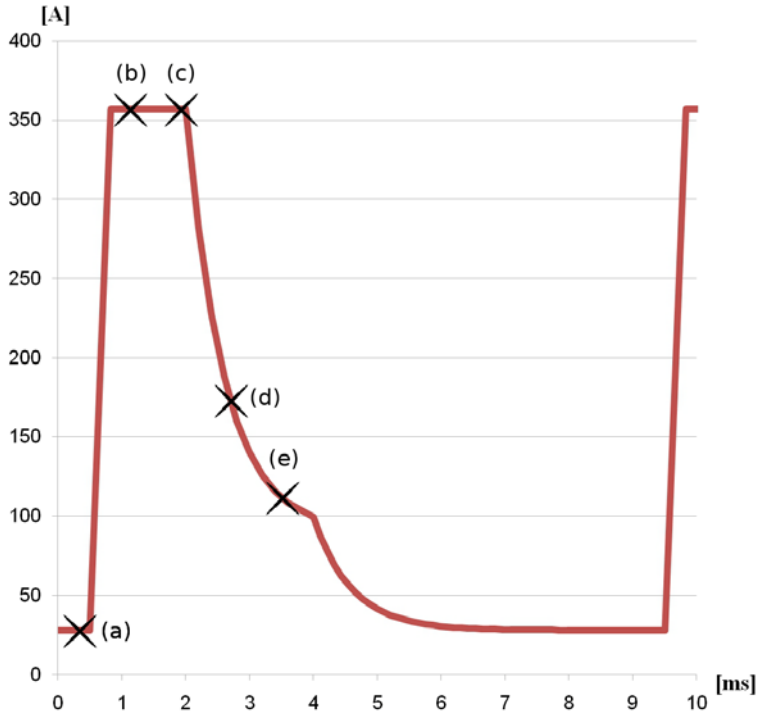

Figure 3 Electric current waveform imposed on both experiment and numerical simulation. [29]

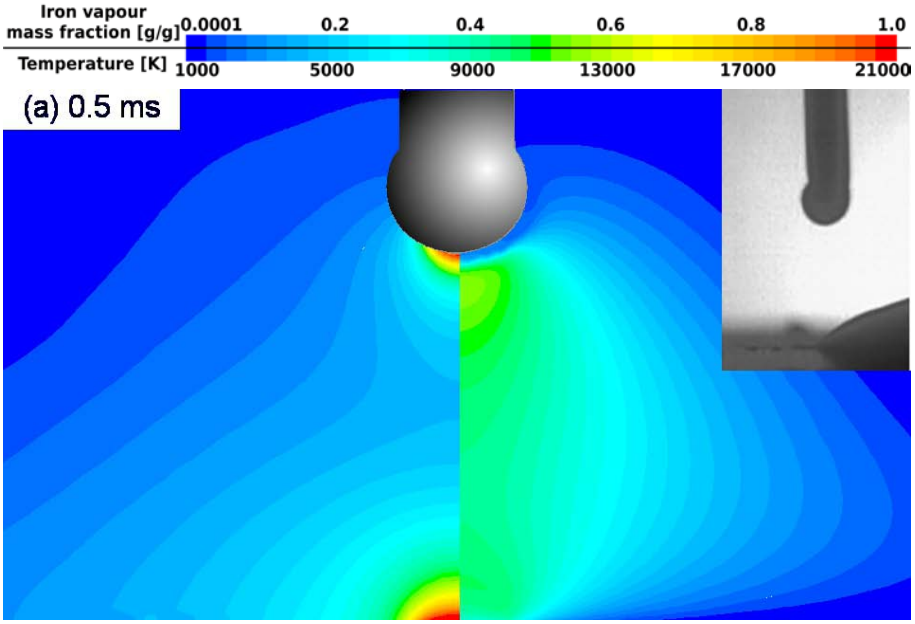

Figure 4 Iron vapour mass fraction [g/g] (left) and plasma temperature [K] (right) during background current phase. On top-right, a high-speed image of the process with the same conditions of the simulation. [29]

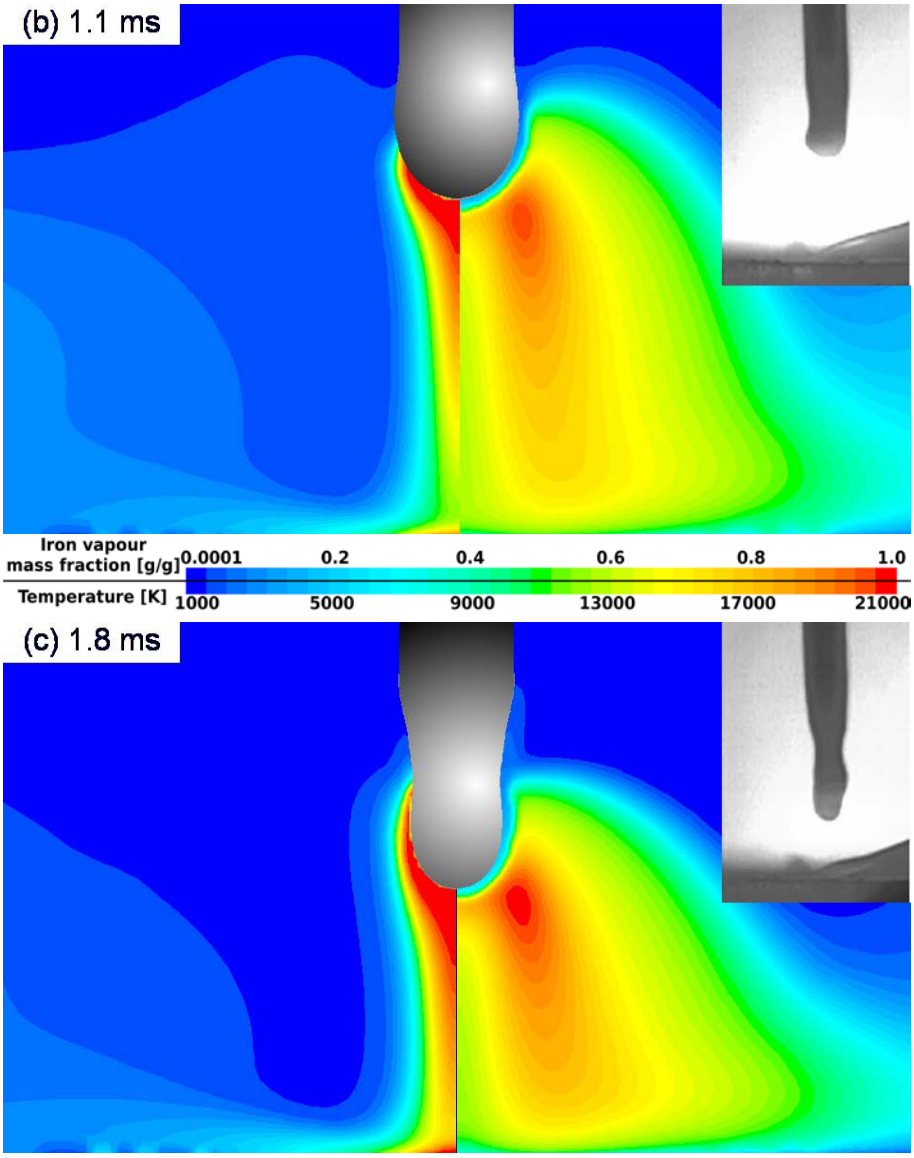

Figure 5 Iron vapour mass fraction [g/g] (left) and plasma temperature [K] (right) at different time steps during peak current phase. On top-right of each picture, a high-speed image of the process with the same conditions of the simulation. [29]

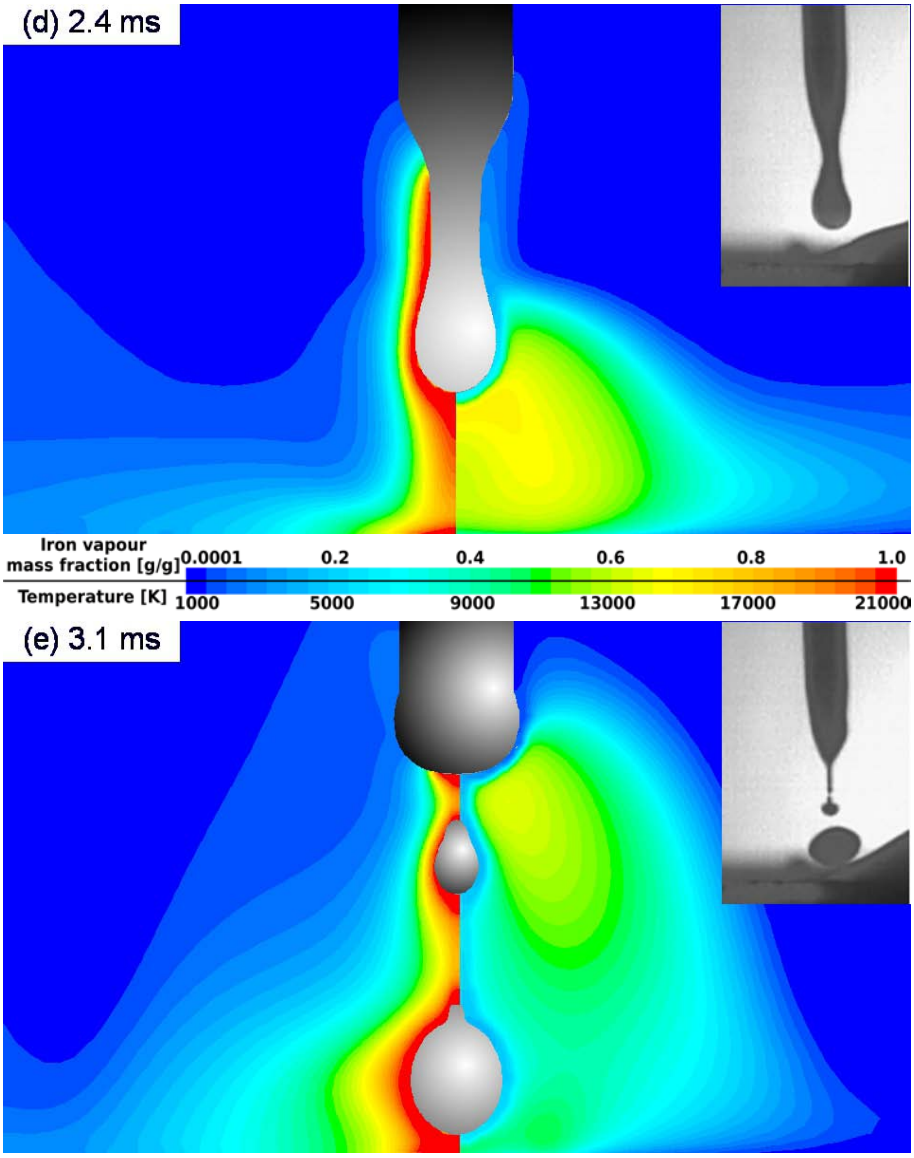

Figure 6 Iron vapour mass fraction [g/g] (left) and plasma temperature [K] (right) at different time steps during current slope-down phase. On top-right of each picture, a high-speed image of the process with the same conditions of the simulation. [29]

Results for the electric potential, tangential magnetic, current density and Lorentz force fields at different time steps are reported (figures 7-9). The anodic and the cathodic voltage drops are not included in the electromagnetic equations and in the calculated voltage distribution in the plasma: with this approximation the total voltage drop is underestimated by approximately 15 V. In figure 7 it is shown that with a current of 30 A there is an overall low magnetic field induction on the surface of the wire ($\approx$0.01 T). Lorentz forces are mostly centripetal, with an axial component due to variation in the current cross section. Current density distribution has a maximum slightly off axis, due to the high concentration of iron vapour on the surface even with low current. With 360 A of current there is an almost linear increase in magnetic field ($\approx$0.17 T) as shown in figure 8. As there is an increase in current density of the same order of the magnetic field one, Lorentz forces, especially in the proximity of the surface of the wire ($\approx$2.4e6 A/m^2), show an order two increase compared to frame (a). It's interesting to note that Lorentz forces have a strong tangential component on the surface of the molten wire that oppose the Marangoni force flow. As the molten liquid starts to move forward, the

conductive cross section of the wire reduces, moreover increasing current density and magnetic field, as shown on frame (b). In figure 9 is shown that the reduction in the wire cross section allows to keep a strong pinching effect even with a lower current, like 180 A of frame (d), as the Lorentz forces reaches an even higher intensity (≈2.4e8 A/m^2). After the droplet detachment at frame (e) the Lorentz Forces are considerably lower due to the absence of stretching of the wire and lower currents. The presence of in-flight droplets of liquid influences the voltage distribution and current density distribution.

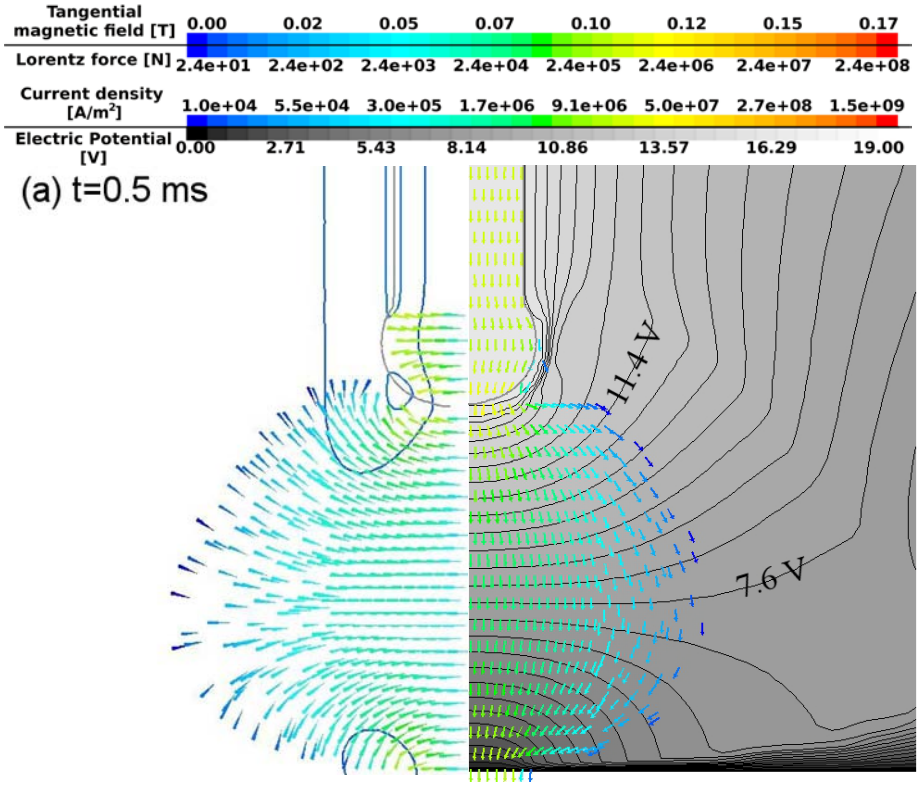

Figure 7 Magnetic field contours [T] (left, interval 4.9 mT) and electric potential contours [V] (right, interval 0.54 V) with superimposed Lorentz forces [N] (cones on the left) and current density [A/m^2] (arrows on the right) versors during background current phase. [29]

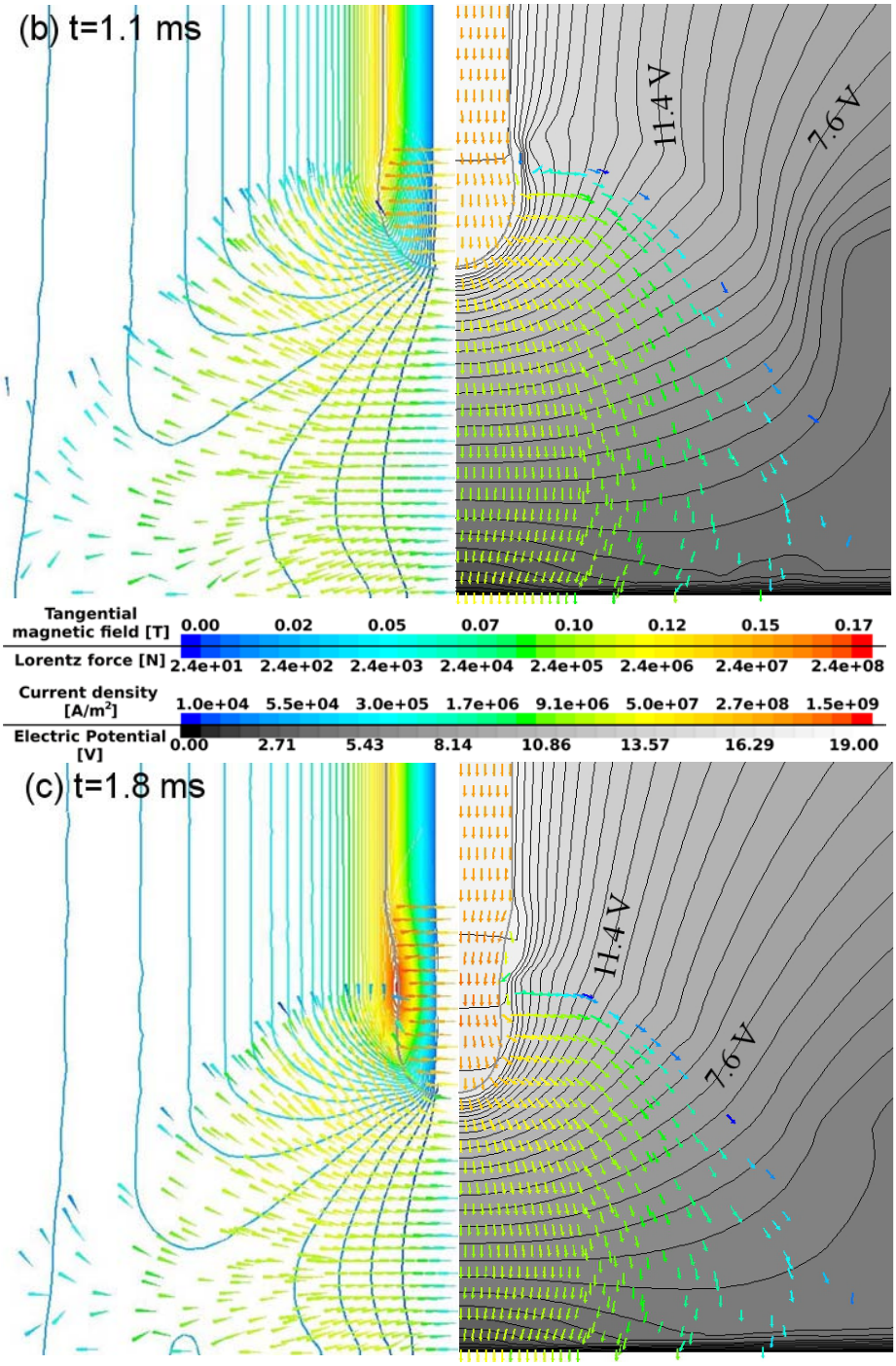

Figure 8 Magnetic field contours [T] (left, interval 4.9 mT) and electric potential contours [V] (right, interval 0.54 V) with superimposed Lorentz forces [N] (cones on the left) and current density [A/m^2] (arrows on the right) versors at different time steps during peak current phase. [29]

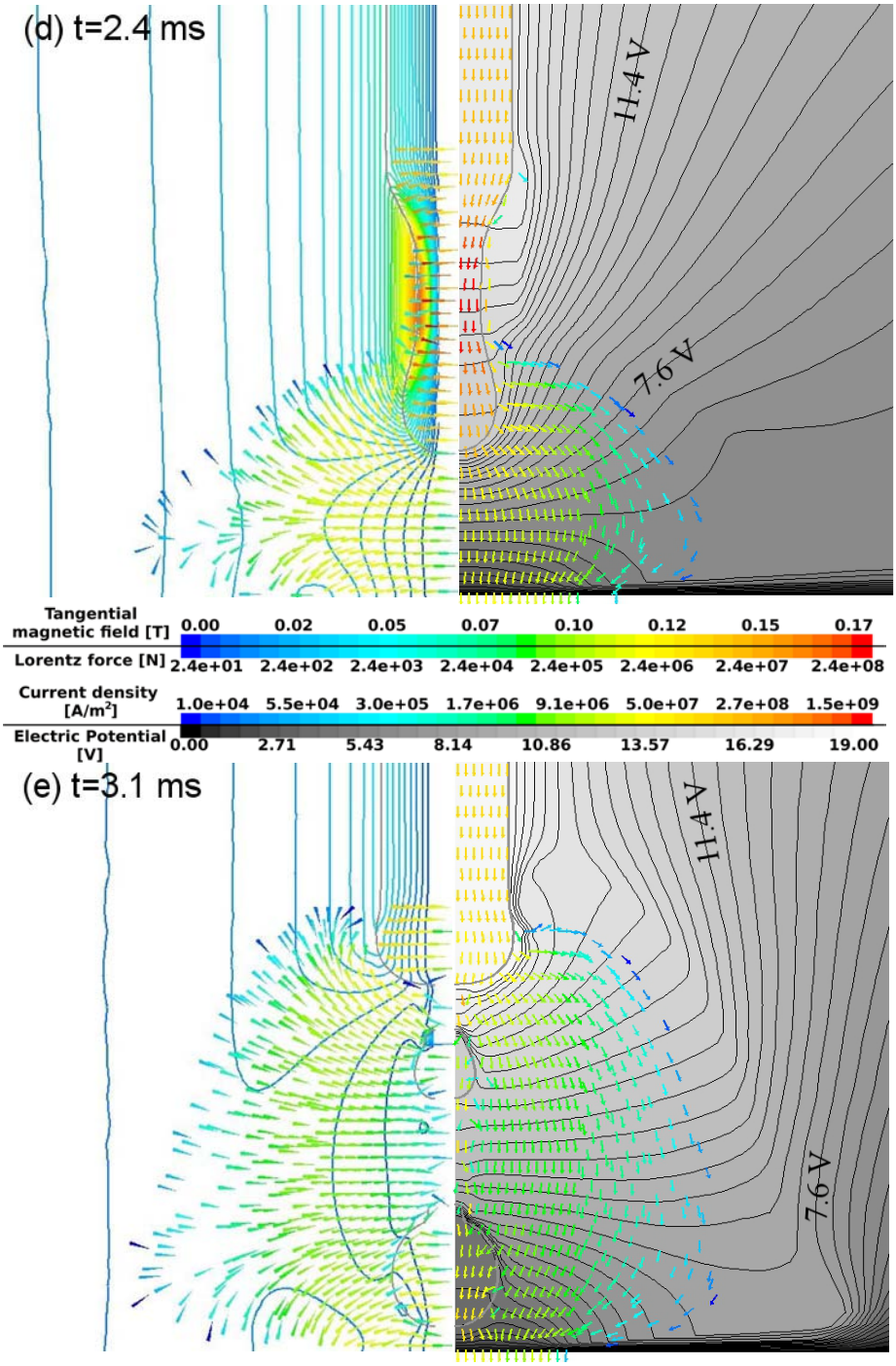

Figure 9 Magnetic field contours [T] (left, interval 4.9 mT) and electric potential contours [V] (right, interval 0.54 V) with superimposed Lorentz forces [N] (cones on the left) and current density [A/m^2] (arrows on the right) versors at different time steps during current slope down phase. [29]

1.5 Conclusions

A pulsed welding process has been investigated using 2D time-dependent modelling and high-speed camera imaging. It has been shown that metal vapour from the overheated wire tip induces an off-axis temperature peak during the high current phase of the cycle, whereas during the base phase the temperature peak is on the axis. A comprehensive analysis of the electromagnetic characteristics involved in the process has been performed in different phases of the droplet detachment. It has been shown that combined effects of droplet shape and high current pulses induce a pinch effect that allow for a droplet detachment during the base current phase.

2. Moments method: fume formation and distribution

2.1 Introduction

Gas-metal arc welding (GMAW) is a process in which a non-constricted plasma arc is ignited between a workpiece and a metal wire that is melted by the heat from the arc, resulting in metal transfer occurs from the wire to the workpiece [2, 6]. Depending on the combination of process operating parameters (arc current time-profile, the wire-feeding rate, wire material and diameter, etc.), the metal transfer to the workpiece can be obtained in globular, spray, pulsed or short-circuit mode [5, 6].
Following recent studies on health effects for welding workers exposed to fume inhalation [37, 38], a huge effort is currently being devoted to the investigation of fume formation during the welding process and to the development of processes with lower fume production rate.
In the welding process, fumes are generated by nucleation and growth of nanoparticles from the metal vapour coming from evaporating weld pool, droplets and metal wire. While a fraction of the produced metal vapour will be condensed on the workpiece [39], most of it will be transported by convection to the cooler edge regions of the arc where nanoparticles can nucleate and successively grow by heterogeneous condensation and coagulation.
Even if experimental try and fail approaches have been adopted to develop operating conditions that induce a lower formation of fumes [2], modelling is a valuable tool that provides insight on those physical processes occurring during the formation phase that cannot be easily monitored by diagnostics.
Modelling of fume formation during gas metal arc welding has been reported by Tashiro et al. [40], taking into account a simplified metal transfer approach and vapour transport in a 2-D framework while the fume formation has been modelled along different flow pathlines in a 1-D approach without considering time-dependent variations of the current waveform.
In this work, the simulation of fume formation in pulsed GMAW process is reported taking into account the metal transport and metal vapour formation in a self-consistent approach using the Volume-of-Fluid (VoF) method and modelling fume nanoparticles production using the method of moments (MoM) for the solution of the aerosol general dynamic equation [41]. While this method has been widely used for the modelling of nanoparticle synthesis in thermal plasma reactors [42], this is the first attempt to implement the MoM approach in modelling fume formation in pulsed GMAW. This approach allows to investigate the fume formation mechanisms in different phases of the current pulse and to track the mass transport of fumes. The results presented in the following pages have been published in [43].

2.2 Process Modelling

Modelling of a pulsed GMAW process has been accomplished with reference to a Cebora Sound MIG 5040/TD Double Pulse source operated with a wire feed rate of 5 m/min and a pure iron wire of 1 mm diameter. The distance between the surface of the workpiece and the contact tip of the torch is set at 15 mm, with an average arc length of 4 mm and a stick out length of 11 mm. Ar was used as shielding gas, with a constant flow rate of 10 l/min. The pulsed current waveform used as a reference in this work is characterized by a period of 9 ms, a peak of current of nearly 350 A and a background current of 30 A (see figure 10). If the electric pulse is well tuned, after a transient start-up of some tens of pulses, the droplet detachment and metal transfer assumes a periodic behaviour. Results for a single droplet transfer in the periodic behaviour obtained after more than one hundred pulses are reported.

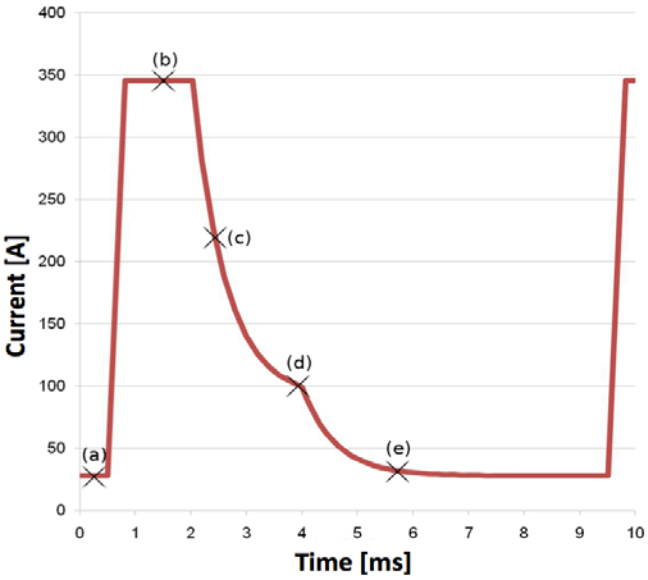

Figure 30 Electric current waveform adopted in pulsed GMAW process modelling. [43]

2.2.1 Modelling of plasma behaviour, metal transfer and vapour production

Mass continuity, momentum, and energy conservation (1.1, 1.2, 1.3) are solved in the whole computational domain assuming Local Thermodynamic Equilibrium (LTE) as reported in [28, 29]. Metal vapour conservation (1.4) is modified as it follows:

$$\frac{\partial \rho y_{vap}}{\partial t} + \nabla \cdot \left(\rho y_{vap} \vec{u}\right) = \nabla \cdot \left(\rho D_{vap} \nabla y_{vap}\right) + S_{vap} + S_{evap} - S_{fume} \qquad (1.13)$$

where S_{evap} is the production of metal vapour due to evaporation of nanoparticles and S_{fume} is the vapour consumption on behalf of nanoparticles formation.
The tracking of molten metal and the prediction of the metal droplet shape have been done using the VoF method by solving equation 1.5.

Diffusion of metal vapour from the molten metal has been taken in account using a simplified diffusion model, neglecting demixing effects. The production of metal vapour on the wire, droplet and workpiece surfaces has been self-consistently

calculated through the vapour mass flux J_{vap} using Hertz-Knudsen-Langmuir approximation reported in equation 1.6.
It is known that Hertz-Knudsen-Langmuir formula results in a overestimation of the *net evaporation rate* in near-cathode plasma since it does not include the effect of the electric field that pulls metal vapour ions back to the evaporating surface [44]; however, in the present model the main source of vapour is the anodic wire surface, in which the electric field acts to push the ions away from the evaporating surface thus resulting in no reduction of the net evaporation rate. Turbulent effects on flow have been neglected.
The electromagnetic field equations (1.8, 1.9, 1.10 and 1.11) have been solved in their vector potential form *A* using the extended field approach as in [45].

2.2.2 Moment method for the modelling of fume nanoparticle formation

Fume formation can be described by the aerosol general dynamic equation (GDE), proposed by Friedlander [41]:

$$\frac{\partial}{\partial t}n(v_p)+\nabla\cdot[\vec{u}n(v_p)]=\nabla\cdot[D(v_p)\nabla n(v_p)]+I\delta_D(v_p-v_p^*)-\frac{\partial}{\partial v_p}[Gn(v_p)]$$
$$+\frac{1}{2}\int_0^{v_p}\beta(v_p',v_p-v_p')n(v_p')n(v_p-v_p')dv_p'-\int_0^{\infty}\beta(v_p,v_p')n(v_p)n(v_p')dv_p' \qquad (1.14)$$

where n is the PSD function (PSDF), v_p is the particle volume, $\boldsymbol{u}$ is the gas velocity, D is the particle diffusion coefficient as proposed by Phanse and Pratsinis [46], I is the nucleation rate, δ_D is the Dirac delta function, G is the heterogeneous condensation growth rate, β is the interpolative collision frequency function and the suffix * denotes the critical state.
According to Friedlander, stable nuclei formed from the precursor vapour at a defined nucleation rate, are moved by convection and diffusion through the surrounding fluid, growing due to vapour condensing on their surface; particles can also collide among themselves, sticking together to form a larger one while reducing their total number density [41].
The aerosol GDE is mathematically reformulated in order to obtain a system of equations that is easier to solve using the method of moments (MoM) that relies on the following assumptions:

- spherical nanoparticles;
- negligible nanoparticles inertia;
- nanoparticles temperature and velocity identical to those of the plasma flow;
- nanoparticle size following a uni-modal log-normal distribution.

In the MoM approach, the equations for the first three moments of the PSDF are solved. The k^{th} moment is defined as:

$$M_k=\int_0^{\infty}v_p^k n(v_p)dv_p \quad k=(0,1,2) \qquad (1.15)$$

The zero-th moment represents the total concentration of the generated nanoparticles, while the first moment corresponds to their total volume. Meanwhile, the second moment is proportional to the light scattered by the nanoparticles in case their size is much smaller than the wavelength of the incident light.
The moment steady state transport equations then take the form:

$$\nabla\cdot[\boldsymbol{u}M_k]=[\dot{M}_k]_{nucl}+[\dot{M}_k]_{cond.}+[\dot{M}_k]_{coag}+[\dot{M}_k]_{diff}-[\dot{M}_k]_{evap} \quad k=(0,1,2) \qquad (1.16)$$

where the terms $[\dot{M}_k]$ represent the net production rates due to nucleation, condensation, coagulation, diffusion and evaporation. These sources terms have been implemented according to [42,47].
The additional evaporation term has been implemented as follows:

$$[\dot{M}_1]_{evap} = \frac{J_{vap}}{\rho_p}(36\pi M_0)^{1/3} M_1^{2/3} \tag{1.17}$$

$$[\dot{M}_2]_{evap} = 2\frac{J_{vap}}{\rho_p}\frac{(36\pi M_1^{\,5})^{1/3}}{M_0^{2/3}} \tag{1.18}$$

where ρ_p is the particle density.
The system is then mathematically closed by the definitions of geometric standard deviation σ_g and of geometric mean volume v_g and by the relation between moments:

$$ln^2\sigma_g = \frac{1}{9} ln\left(\frac{M_0 M_2}{M_1}\right) \tag{1.19}$$

$$v_g = \frac{M_1^2}{M_0^{3/2} M_2^{1/2}} \tag{1.20}$$

$$M_k = M_0 v_g^k exp\left(\frac{9}{2} k^2 ln\sigma_g\right) \tag{1.21}$$

Finally, a source term has been added to the metal vapour conservation equation accounting for the metal vapour consumption on behalf of nucleation and condensation and for metal vapour production rate due to evaporation of nanoparticles, through the term

$$S_{evap} = J_{vap}(36\pi M_0)^{1/3} M_1^{2/3} \tag{1.22}$$

A null value as been used as boundary conditions for moment transport equations at inlets, solid interfaces; at the outlet, null flux has been used for cells with outgoing flow, whereas a null value has been set for cells with reverse flow.

2.3 Results

Modelling results for a selection of instants, as shown in figure 10 with crosses on the current profile, are reported. Results are reported for the GMAW process under conditions of periodic behaviour of the metal transfer and of the iron vapour concentration field. In modelling these conditions can be obtained by running the model for several cycles after setting the initial conditions.

Results for plasma temperature, gas velocity, iron vapour concentration, vapour consumption and nanoparticle mass concentration are reported in figure 11 for time frame (a), where the current is set at the base level; consequently the temperature is generally at lower than for the rest of the pulse. Maximum temperature is around 7000 K and the arc is diffuse. The wire is partially melted and the droplet has an almost spherical shape, mainly determined by surface tension forces. The iron vapours are mostly concentrated in the region close to the evaporating wire tip and in the vicinity of the workpiece surface, without inducing a significant cooling of the arc. Plasma

maximum velocity in the arc is around 25 m/s and a recirculating pattern has been found close to the arc attachment at the workpiece.
At this time frame, some vapours produced during the previous pulse have been transported to the fringes of the arc by convection and diffusion and they are converted to nanoparticles; the vapour consumption field has a narrow distribution around the 2000 K temperature iso-contour, with two peaks with a value of about 0.16 and 1.6 mg/mm^3 s close to the workpiece and to the wire tip, respectively. Total nanoparticle production in this time frame is about 1 mg/s.
Nanoparticles are formed mainly in the region with vapour consumption peaks: nanoparticles generated close to the workpiece are transported radially outward by the convective effect of the plasma gas, whereas those generated near the wire tip are dragged by the plasma flow to the high temperature region in the arc center where they are completely converted again to iron vapour. Nanoparticles formed during the previous pulse are transported away from the arc center by recirculating flow. A maximum mass concentration around 5e-3 µg/mm^3 is reached in the vicinity of the arc fringes before nanoparticles are dispersed in the surrounding atmosphere.

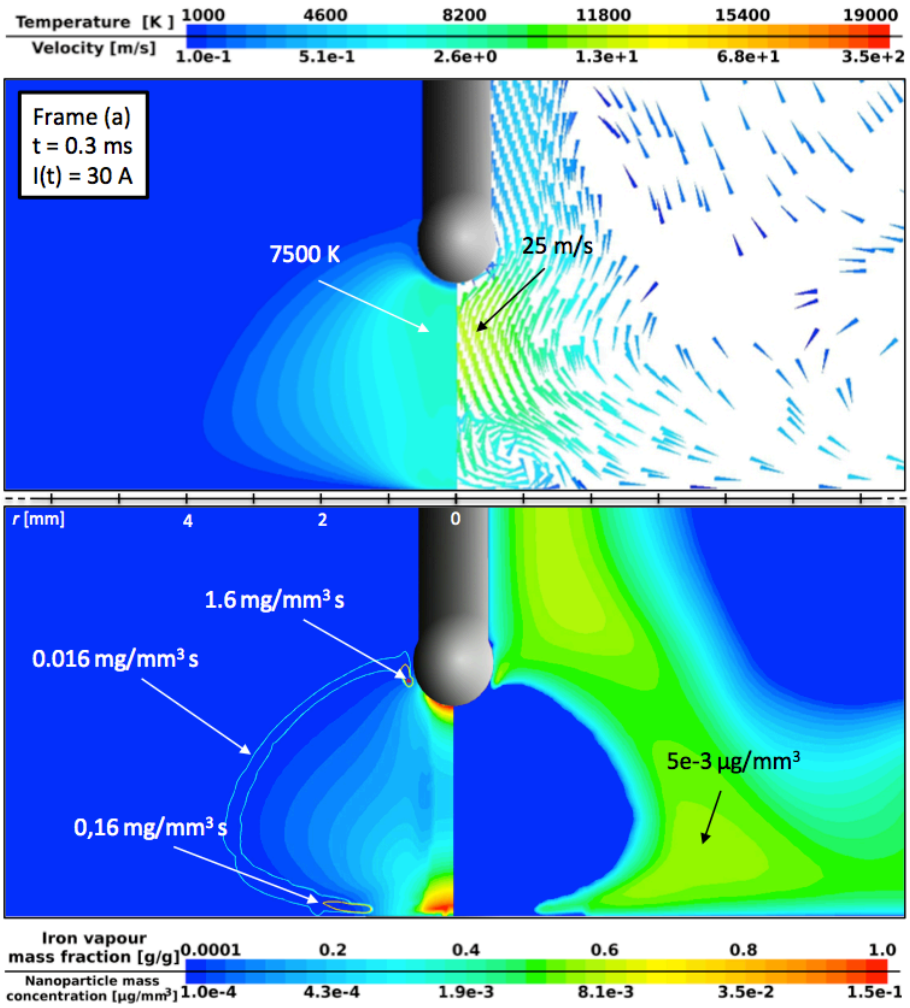

Figure 11 Results for time frame (a): plasma temperature contours (top-left), gas velocity vectors (top-right), iron vapour concentration filled contours with superimposed line contours of vapour consumption source (bottom-left), and nanoparticle mass concentration (bottom-right). [43]

The relevant results obtained for frame (b) are reported in figure 12. From frame (a) to frame (b) the current rises more than ten times (from 30 A to 350 A) while the shape of the wire tip remains almost unchanged, even though the metal droplet hanging from the solid wire tip is slightly elongated as a consequence of magnetic forces acting on it. The higher current induces a strong increase of the arc temperature, reaching a maximum value of about 16500 K and a higher production of iron vapours that are transported along the arc axis by a strong convective flow with a velocity up to 350 m/s. High iron vapour concentration on the arc axis leads to the formation of a cool channel with a temperature of about 6000 K. Experimental evidences for the temperature drop and for the high iron vapour concentration (mole fraction higher than 80%) in the central part of the arc have been reported in literature for a pulsed GMAW in similar operating conditions [18].
As a consequence of higher current, the arc is also broadened and temperature iso-contour where nanoparticle are formed (2000 K) is shifted to a higher radial position. The plasma flow pattern is that typical of a jet impinging on a substrate and a strong flow in the outward radial direction is generated near the workpiece, inducing the transport of iron vapour to the fringes of the arc. Nanoparticle nucleation (see vapour consumption source term) is mainly concentrated near the workpiece and around the temperature iso-contour at 2500 K with a peak of about 0.9 mg/mm^3 s. Nanoparticle production rate in this time frame is about 7.2 mg/s. Nanoparticles that are formed are transported to the outer region and to the surrounding atmosphere by convection reaching a maximum mass concentration of 2e-2 $\mu g/mm^3$.

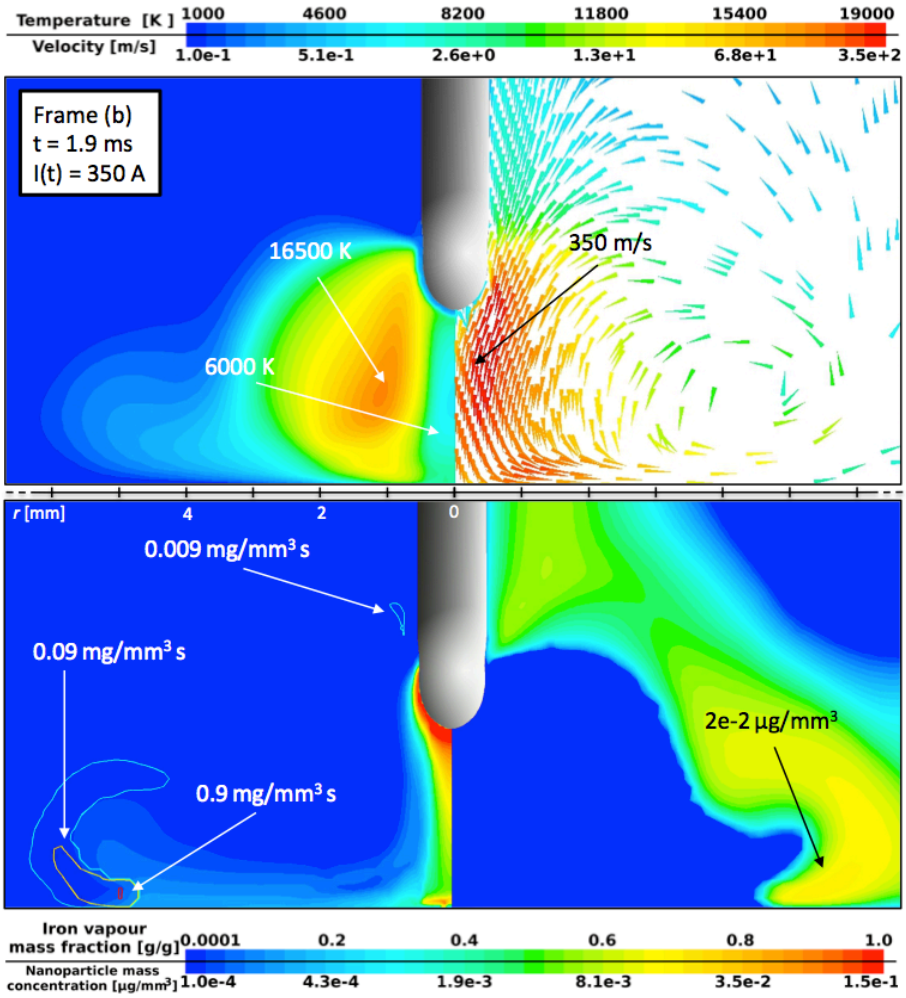

Figure 12 Results for time frame (b): plasma temperature contours (top-left), gas velocity vectors (top-right), iron vapour concentration filled contours with superimposed line contours of vapour consumption source (bottom-left), and nanoparticle mass concentration (bottom-right). [43]

During the ramp-down current, the droplet detachment occurs with the melted part of the wire being constricted and dragged towards the workpiece. Relevant results for this time frame are reported in figure 13. Since the current is at 220 A at this time frame, evaporation of the wire is still high and it is extended on a larger surface of liquid metal. The emitted iron vapour is transported downstream–along the torch axis. Vapour is strongly emitted also from a portion of surface of the melted wire where there is no plasma arc. Close to this part of the wire, a highly concentrated production of nanoparticles (up to 13 mg/mm^3 s) occurs which is mainly due to the high vapour mass fraction (close to 1 g/g) and low gas temperature (about 2000 K). Total nanoparticle production rate in this time frame is around 11 mg/s. Nanoparticle concentration on the side of the melted part of the wire consequently reaches a value of 0.1 µg/mm^3. However, these nanoparticles are mainly transported downstream by the plasma flow with still high velocity (about 90 m/s) towards the center of the arc and they are converted back to the vapour state. On the contrary, nanoparticles generated near the workpiece in the fringes of the arc, are transported outward radially, inducing nanoparticle dispersion in the surrounding atmosphere.

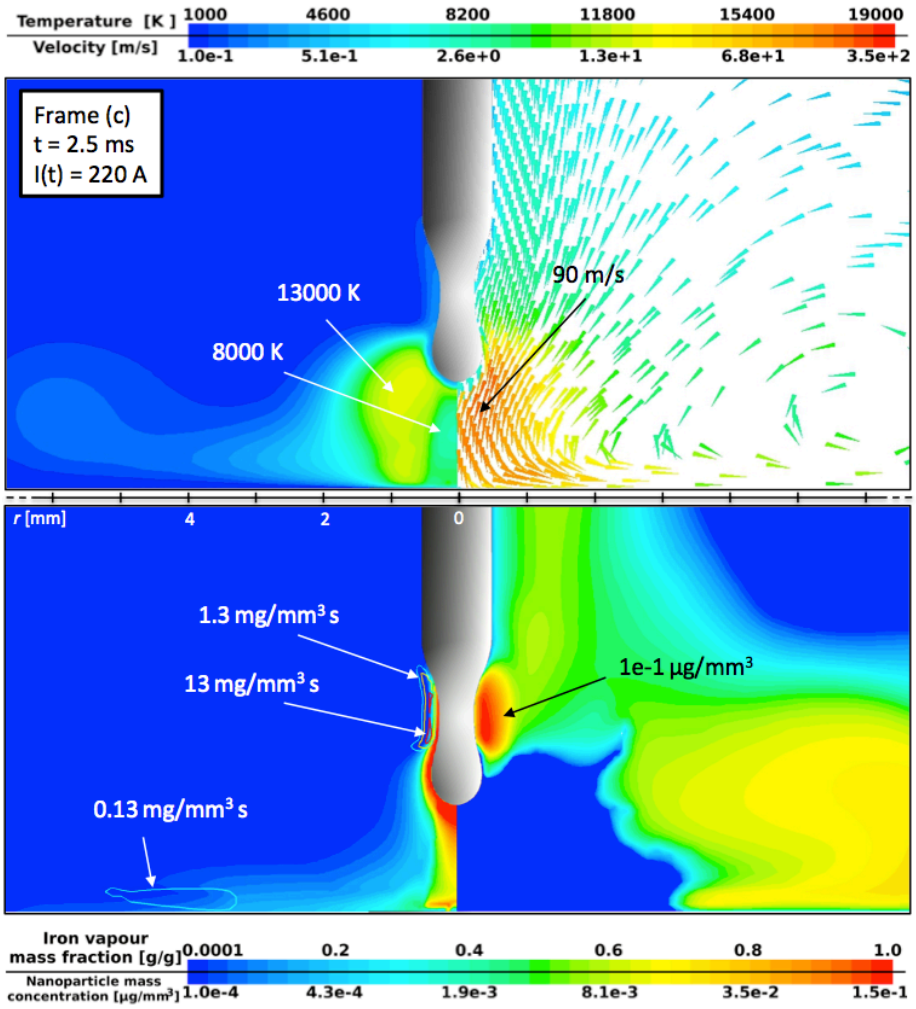

Figure 13 Results for time frame (c): plasma temperature contours (top-left), gas velocity vectors (top-right), iron vapour concentration filled contours with superimposed line contours of vapour consumption source (bottom-left), and nanoparticle mass concentration (bottom-right). [43]

When the current has been reduced at 100 A, about 2 ms after the pulse peak phase, the droplet is already detached and it has been dragged by the plasma flow towards the workpiece. Results for plasma temperature, gas velocity, iron vapour concentration, vapour consumption and nanoparticle mass concentration are reported in figure 14 for this time frame. Plasma temperature has a peak value of 12500 K and the arc is less expanded in the radial direction, as the current is lower than for previous time frames. Gas velocity is about 40 m/s and thus convective transport is still the main contribution to iron vapour and nanoparticle transport phenomena. Vapour concentration is peaked on the torch axis as a consequence of the strong emission from the detached droplet and its satellite droplet during transition along the inter-electrode gap. Iron vapours are transported to the outer region of the arc where they are converted to nanoparticles, especially in the vicinity of the workpiece. In this region, the vapour consumption source has a maximum with a value of about 0.9 mg/mm^3 s, whereas nanoparticles are nucleated and transported to the outer region and dispersed in the surrounding atmosphere with a mass concentration of about 2e-2 µg/mm^3. Nanoparticle production rate in this time frame is about 5.2 mg/s.

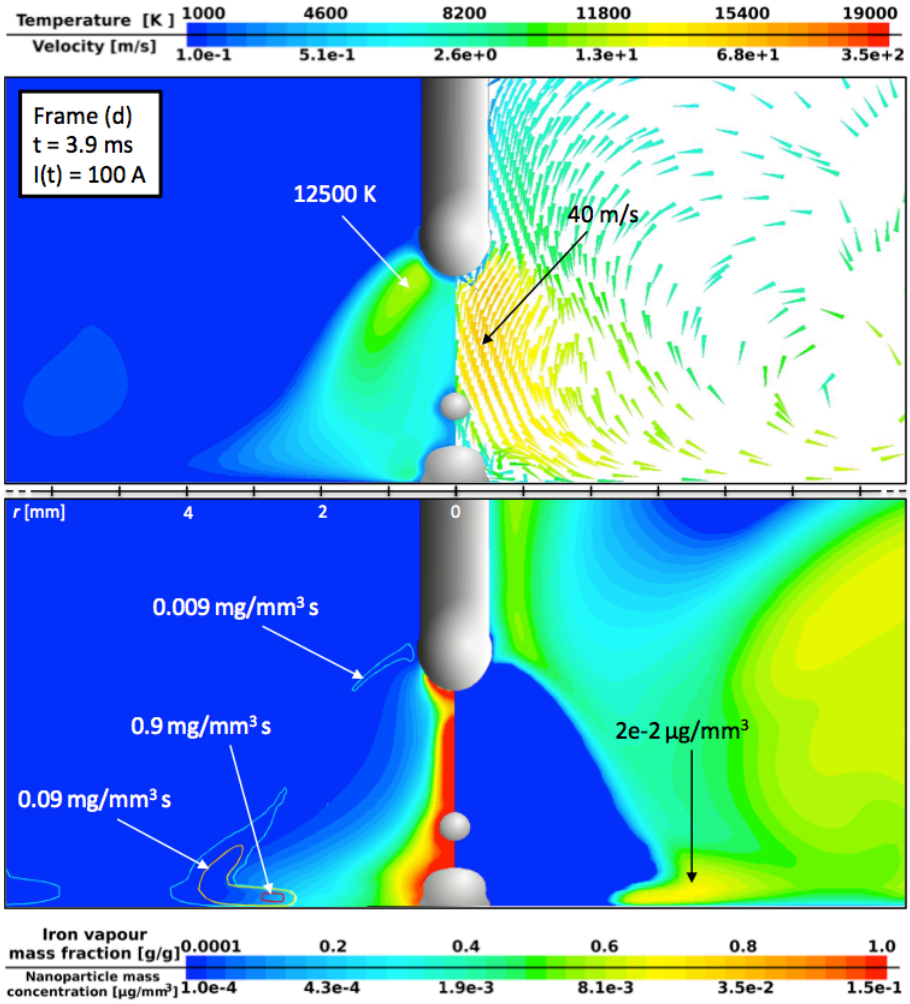

Figure 14 Results for time frame (d): plasma temperature contours (top-left), gas velocity vectors (top-right), iron vapour concentration filled contours with superimposed line contours of vapour consumption source (bottom-left), and nanoparticle mass concentration (bottom-right). [43]

At the end of the current pulse, the current intensity is almost at its lowest value (30 A) and the melting process of a new portion of wire starts. Relevant results for this time frame are reported in figure 15. Physical phenomena occurring in the time region between this time frame and time frame (a) of the following pulse are similar to those previously described for frame (a). Temperature of the arc is lowered as the current is decreased and the arc radius is decreased accordingly. The production of nanoparticles occurs mainly in the region close to the workpiece (the production rate in this time frame is less than 2 mg/s) and the produced nanoparticles are transported towards the surrounding atmosphere by convection and, partially, also by diffusion, as the gas velocity is decreased to about 20 m/s.

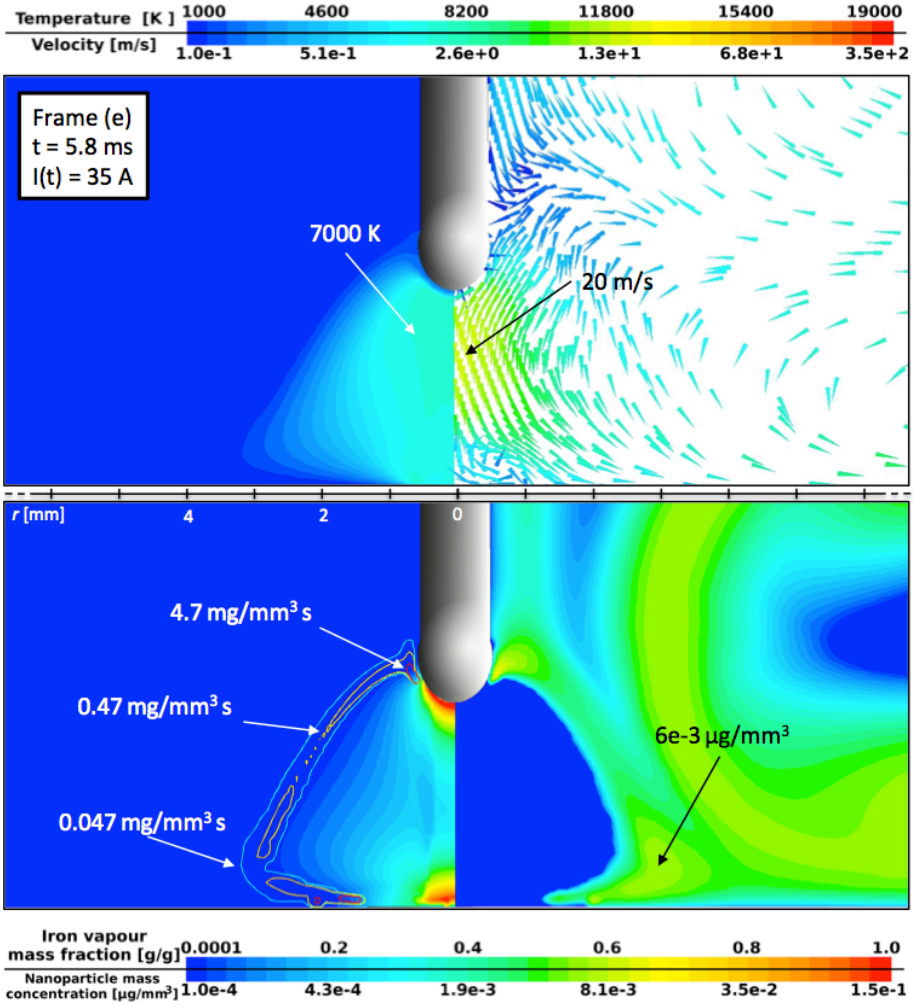

Figure 15 Results for time frame (e): plasma temperature contours (top-left), gas velocity vectors (top-right), iron vapour concentration filled contours with superimposed line contours of vapour consumption source (bottom-left), and nanoparticle mass concentration (bottom-right). [43]

2.4 Discussion

The model implemented in this work takes into account the time-dependent tracking of the fumes generated in a GMAW process using a moment of moments approach for the solution of the aerosol general dynamic equation. Only one model has been reported in literature [40] to describe fume formation in GMAW: the model reported in [40] can take into account the plasma arc behaviour and metal transfer in a time-dependent framework as it has been done in the present work but the computation for fume formation is separately carried out under the steady-state approximation, assuming that the temperature field doesn't change in the time required for nanoparticles to be generated and then transported to the surrounding atmosphere. While this assumption can be acceptable for constant current GMAW processes, it is a rather rough approximation for pulsed processes in which the current intensity changes by more than one order of magnitude in less than one millisecond. In this case, the population of nanoparticles must be computed in a time-dependent framework as it has been proposed in this work.

As an example, in the operating conditions analysed in this work, nanoparticles generated in time frame (a) are rapidly evaporated again as the current is increased

from the background level to the peak level: the arc is broadened and the temperature is increased also in the region where nanoparticles have been generated. Since the current is 30 A in frame (a), nucleated nanoparticles have a low initial velocity (less than 1 m/s) and the time required to escape from the plasma arc (few ms) is higher than the time required for the arc to heat up nanoparticle above boiling point (about 0.2 ms).
Moreover, after the current pulse, nanoparticle nucleation occurs in a spatial region where temperature decreases by more than 1200 K in less than 0.6 ms as a consequence of current intensity reduction, resulting in a cooling rate of about 2 000 000 K/s, which is in the same order of magnitude of the cooling rates due to nanoparticle transport from their nucleation point to a cooler region by convection, which is in the range 10^5-10^7 K/s.
These phenomena cannot be predicted by any model that doesn't take into account time-dependent transport of the generated fumes.
Another feature of the model reported in the present work is that nanoparticle concentration can be determined on the whole spatial domain, whereas the model reported in [40] allows to track fume formation only for few selected positions. The tracking of fume concentration in the whole domain is a prerequisite in order to quantify the total production of fumes and their dispersion in the surrounding atmosphere under different GMAW operating conditions, which in turn is mandatory in order to seek optimal conditions that reduce fume emission.
Results reported in this work suggest that the coupled solution of plasma arc fluid-dynamics, liquid transfer, vapour transport and time-dependent aerosol general dynamic equation through the method of moments allows a time-dependent tracking of fumes also in plasma processes where temperature time-variations occur faster than nanoparticle transport from the nucleation region to the surrounding atmosphere, as it is the case for most pulsed GMAW processes.
Nanoparticle production rate predicted by this model at different time frames ranges between 1 and 11 mg/s; the time-averaged mean value at 5.5 mg/s is in agreement with fume formation rate reported in many experimental works [2, 48,49].

2.5 Conclusions

A pulsed gas metal arc welding (GMAW) process has been investigated using a novel modelling approach, which allows a time-dependent tracking of fumes also in plasma processes where temperature time-variations occurs faster than nanoparticle transport from the nucleation region to the surrounding atmosphere. This model offers insight on the pulsed GMAW process that could not be obtained with previous modelling approaches: the time distribution of fume sources with a time-varying current and their spatial localization and quantification along the fringes of the arc. Qualitative agreement has been found between results of this model for temperature distribution and iron vapour concentration and experimental data reported in literature for similar GMAW processes; a strong fluctuation of fume formation rate has been predicted by the model during current pulse cycle (from 1 to 11 mg/s), with time-averaged mean values in agreement with experimental data reported in literature (about 5 mg/s). The results reported in this work can be used as a basis for the optimization of pulsed GMAW process in order to reduce the production of harmful nanosized fumes.

References

[1] Gas metal arc welding, Welding Handbook vol. 2, 9th Edition, American Welding Society (2004)
[2] Murphy A B, J. Phys. D: Appl. Phys. **43**, 434001 (2010)
[3] Collard J F, Weld. J. **67**(11), 35-38 (1988)
[4] Ueguri S, Hara H and Komura H, Weld. J. **64**(8), 242-250 (1985)
[5] Jacobsen N, J. Phys. D: Appl. Phys. **25**, 783-797 (1992)
[6] Lancaster J F, The Physics of Welding, Oxford, Pergamon (1984)
[7] Kim Y S and Eagar T W, Weld. Res. Suppl., 269-278 (1993)
[8] Thorn K, Feenstra M, Young J C, Lawson W H S and Kerr H W, Metal Construction **14**(3), 128-133 (1982)
[9] Haidar J and Lowke J J, J. Phys. D: Appl. Phys **29**, 2591 (1996)
[10] Haidar J and Lowke J J, IEEE Trans. Plasma Sci. **25**, 931 (1997)
[11] Lucas W and Amin M, Metal Construction **2**, 77-83 (1975)
[12] Agusa K, Nishiama N and Tsuboi J, Metal Construction **9**, 570-574 (1981)
[13] Quintino L and Allum C J, Weld. & Met. Fabr. Vol. **3**, 85-89 (1984)
[14] Quintino L and Allum C J, Weld. & Met. Fabr. Vol. **4**, 126-129 (1984)
[15] Wu C S, Chen M A and Lu Y F, Meas. Sci. Technol. **16**, 2459-2465 (2005)
[16] Zielinska S, Musiol K, Dzierzega K, Pellerin S, Valensi F, de Izarra Ch and Briand F, Plasma Sources Sci. Technol. **16**, 832-838 (2007)
[17] Wilhelm G, Gott G, Schopp H and Uhrlandt D, J. Phys. D: Appl. Phys. **43**, 434004 (2010)
[18] Rouffet M E, Wendt M, Goett G, Kozakov R, Schoepp H, Weltmann K D and Uhrlandt D, J. Phys. D: Appl. Phys. **43**, 434003 (2010)
[19] Valensi F, Pellerin S, Boutaghane A, Dzierzega K, Zielinska S, Pellerin N and Briand F, J. Phys. D: Appl. Phys. **43**, 434002 (2010)
[20] Xu G, Hu J and Tsai H L, J. Appl. Phys. **104**, 103301 (2008)
[21] Murphy A B, Tanaka M, Yamamoto K, Tashiro S, Sato T and Lowke J J, J. Phys. D: Appl. Phys. **42**, 194006 (2009)
[22] Tanaka M, Yamamoto K, Tashiro S, Nakata K, Yamamoto E, Yamazaki K, Suzuki K, Murphy A B and J J Lowke, J. Phys. D: Appl. Phys. **43**, 434009 (2010)
[23] Tsujimura Y, Tashiro S and Tanaka M, Transactions of JWRI **40**(1), 25-29 (2011)
[24] Hu J and Tsai H L, Int. J. Heat Mass Transfer **50**, 833–46 (2007)
[25] Hu J and Tsai H L, Int. J. Heat Mass Transfer **50**, 808–20 (2007)
[26] Schnick M, Fuessel U, Hertel M, Haessler M, Spille-Kohoff A and Murphy A B, J. Phys. D: Appl. Phys. **43**, 434008 (2010)
[27] Fan H G and Kovacevic R, J. Phys. D: Appl. Phys. **37**, 2531–2544 (2004)
[28] Boselli M, Colombo V, Ghedini E and Sanibondi P, IEEE Trans. Plasma Sci. **39**(11), 2896-2897 (2011)
[29] Boselli M, Colombo V, Ghedini E, Gherardi M and Sanibondi P, Plasma Sources Sci. Technol. **21** 055015 (2012) © 2012 IOP Publishing
[30] Wu C S, Chen M A and Lu Y F, Meas. Sci. Technol. **16(**12), 2459–2465 (2005)
[31] Nemchinsky V A, J. Phys. D: Appl. Phys., **30,** 1120–1124 (1997)
[32] Guo H, Hu J and Tsai H L, J. Manuf. Sci. Eng. **132**, 021011 (2010)
[33] Haidar J, J. Phys. D: Appl. Phys. **31**, 1233–44 (1998)
[34] Bernardi D, Colombo V, Ghedini E and Mentrelli A, Eur. Phys. J.D **22**, 119-125 (2003)
[35] Boulos M I, Fauchais P and Pfender E, Thermal Plasmas: Fundamentals and Applications vol I, New York: Plenum (1994)

[36] Gleizes A, Cressault Y and Teulet Ph, Plasma Sources Sci. Technol. **19**, 055013 (2010)
[37] Antonini J M, Critical Reviews in Toxicology **33** 61-103 (2003)
[38] Hewitt P J, Indoor and Built Environment **5** 253-62 (1996)
[39] Deam R T, Simpson S W and Haidar J, J. Phys. D: Appl. Phys. **33** 1393 (2000)
[40] Tashiro S, Tasuku Z, Kentaro Y, Manabu T, Kazuhiro N, Murphy A B, Eri Y, Kei Y and Keiichi S, J. Phys. D: Appl. Phys. **43** 434012 (2010)
[41] Friedlander S K, Smoke, Dust and Haze, Fundamentals of Aerosol Dynamics, New York: Oxford University Press (2000)
[42] Colombo V, Ghedini E, Gherardi M and Sanibondi P, Plasma Sources Science and Technology **21** 055007 (2012)
[43] Boselli M, Colombo V, Ghedini E, Gherardi M and Sanibondi P, J. Phys. D: Appl. Phys. **46** 224006 (2013) © 2013 IOP Publishing
[44] Nemchinsky V A and Showalter M S, J. Phys. D: Appl. Phys. **36** 704 (2003)
[45] Colombo V, Ghedini E, Boselli M, Sanibondi P and Concetti A, J. Phys. D: Appl. Phys. **44** (2011)
[46] Phanse G M and Pratsinis S E, Aerosol science and technology **11** 100-19 (1989)
[47] Colombo V, Ghedini E, Gherardi M, Sanibondi P and Shigeta M, Plasma Sources Science and Technology **21** 025001 (2012)
[48] Zimmer A T, Baron P A and Biswas P, Journal of Aerosol Science **33** 519-31 (2002)
[49] Ioffe I, MacLean D, Perelman N, Stares I and Thornton M, J. Phys. D: Appl. Phys. **28** 2473 (1995)

CHAPTER 2
Plasma arc welding: non equilibrium modelling and experimental optical emission spectroscopy

1. Introduction

Plasma arc welding (PAW) is a process where an electric arc is created between a pointed electrode (usually made of thoriated tungsten) and the workpiece, to provide the necessary energy density and heat flux to melt the workpiece [1-5]. The electrode is positioned inside the torch body and plasma gas (such as argon) is fed around it. The arc generated from the electrode tip is constricted by passing through a copper nozzle in order to increase the plasma velocity and temperature. A sheath gas is injected axially (usually with a swirl component) and concentrically around the arc, allowing the protection of the weld pool from contamination of the surrounding oxidant atmosphere. The combination of constriction and convection stabilization provides a high speed focused plasma jet with deeper weld penetration and higher energy concentration and resistance to perturbations than the gas tungsten arc welding (GTAW) process.
Two modes of operation are available for PAW depending on how the plasma jet interacts with the workpiece: melt-in (15A-200A) and keyhole (>100A). Although the keyhole mode is the most important operation mode for PAW for industrial purpose since the penetration depth is greater, only the melt-in mode operating conditions have been considered here. This choice is motivated by the fact that the focus of this paper is to characterize the plasma arc taking into account also non-equilibrium phenomena, which are more relevant for low current arcs. Also, to the knowledge of the Authors, no results on arc excitation temperature measurement and on non-equilibrium 2T modelling have been reported in literature for this specific process [6-8].
For both the design of plasma sources and for the understanding of fundamental physical phenomena in the field of industrial applications of plasmas, the knowledge of physical quantities in the discharge by means of modelling [9, 10] and/or diagnostics [11, 12] plays a major role for the optimization of processes. In thermal plasma modelling, the assumption of Local Thermodynamic Equilibrium (LTE) has been the rule until recent years, when the increase of available computational power and tools, together with a deeper comprehension of the physics of the non-equilibrium discharge and the availability of more accurate non-equilibrium thermodynamic and transport properties [13-19], has allowed the development and application of non-equilibrium models for different types of plasma sources [20]. Still, comparisons with experiments are needed to validate such models.
Optical Emission Spectroscopy (OES) has been widely used for diagnostics of thermal plasmas to determine physical quantities such as electron and heavy particle temperature and density [21-25]. Simple methods for the analysis of the OES spectrum have been developed in the past that relies only on the assumption of Boltzmann law for the distribution of bounded electrons on atoms/ions excited states, e.g. plotting and fitting the emissivity of two or more lines emitted by the same species in the Boltzmann plot. With these methods, the so-called excitation temperature is determined, which for thermal plasmas is very close to the electron translational temperature [23]. The advantage of the Boltzmann plot is that it is relatively easy to setup and the data analysis is almost straightforward; however, the uncertainties on the determination of temperature depend strongly on the difference of the energy levels related to the

selected lines and on the signal-to-noise ratio (s/n) of the lines adopted in the calculation. In practical cases, it is not always possible to obtain a spectrum in the whole spatial region of interest with two or more lines with both high s/n and high difference in related energy levels; this results in quite high uncertainties in the determination of excitation temperature (more than 30-40%). Methods based on the absolute measurement of volumetric emission coefficient and on norm methods [22] can be more accurate, but they rely on the assumption of LTE for the calculation of equilibrium composition.
In this paper the Authors compare the results obtained by means of both LTE and non-LTE two-temperature (2T) numerical modelling [26] with the results of OES diagnostics, proposing a method to extend the Boltzmann plot technique to regions where lines s/n is poor and discussing its validity in case of thermal non-equilibrium conditions; also demonstrating how this approach can be effectively used to characterize a plasma source of industrial interest. For this reason modelling and diagnostics activities have been performed on a commercial plasma source torch.
The investigated plasma arc welding process will be presented in section 2 and the methods used for the characterization of the process will be clarified in sections 3 and 4; results will be reported in section 5, while conclusions will be drawn in section 6.
The results presented in the following pages have been published in [27].

2. Plasma source

The investigated process is a constant current plasma arc welding process working in the melt-in mode (current lower than 100A), obtained using a Cebora plasma source (Plasma Welding Robot connected to a TIG Sound DC 2340T power supply) equipped with a Binzel torch (model Abiplas® Weld 100 W MT). Three different current levels (constant current at 25A, 40A and 70 A) that span the whole current range that induces the melt-in mode with this torch have been analysed. The working gas is pure argon. Operating conditions and dimensions of consumables for different current levels have been reported in table 1. A copper substrate has been used as an anode in order to reduce vapour emission and surface modifications usually characterizing weld pools in stainless-steel plates. A picture of the typical plasma arc welding process at 70 A has been reported in figure 16.

Table 1 Experimental operating conditions and consumables dimensions for the cases analysed

Nominal current (A)	Cathode diameter (mm)	Nozzle internal diameter (mm)	Plasma gas flow rate (slpm Ar)	Sheath gas flow rate (slpm Ar)
25	1.6	1.2	0.5	6
40	1.6	1.2	0.5	6
70	2.4	2.3	1	6

Figure 16 Picture of the operating plasma arc welding process at 70 A. [27]

3. Modelling approach

In the following paragraph the details of the LTE and 2T modelling approaches are reported. A schematic of the computational domain used in the calculations is reported in figure 17.

In the LTE model, the continuity, momentum (Navier-Stokes) and energy equations are solved together with the Maxwell's equations for the electromagnetic field [19]. The continuity and Navier-Stokes equations are

$$\nabla \cdot (\rho \vec{u}) = 0 \tag{2.1}$$

$$\nabla \cdot (\rho \vec{u}\vec{u}) = -\nabla p + \nabla \cdot \bar{\bar{\tau}} + \rho \vec{g} + \vec{J} \times \vec{B} \tag{2.2}$$

where ρ is the mass gas density, $\vec{u}$ the fluid velocity, p the pressure, $\bar{\bar{\tau}}$ the viscous stress tensor, $\vec{g}$ is the gravitational acceleration, and $\vec{J} \times \vec{B}$ the contribution of the Lorentz forces, where $\vec{J}$ is the current density and $\vec{B}$ is the magnetic field.
The energy conservation equation is written as

$$\nabla \cdot (\rho h_t \vec{u}) = \nabla \cdot (k \nabla T) + \frac{5}{2}\frac{k_B}{e}\vec{J} \cdot \nabla T + \vec{J} \cdot \vec{E} - Q_{rad} \tag{2.3}$$

where h_t is the total plasma enthalpy, k is the laminar thermal conductivity, k_B is the Boltzmann constant, e is the electron charge, $\vec{J} \cdot \vec{E}$ is the Joule heating ($\vec{E}$ is the electric field) and Q_{rad} the radiation losses calculated using a net emission coefficient approach [28, 29] with a plasma radius of 1 mm.

In order to take into account the thermal non-equilibrium, a two-temperature approach (2T) is used, in which the translational electron temperature T_e can be different from the translational heavy particle temperature T_h.
Equations for the 2T model have been implemented following the results reported by Freton et al. [26] and are summarized as follows: mass conservation and Navier-Stokes equations are the same as LTE model, whereas separate energy equations for the species are needed. The energy equation for the heavy particles and electrons are

$$\nabla \cdot \left(n_h \frac{5}{2} k_B T_h \vec{u}\right) = \nabla \cdot (k_h \nabla T_h) + Q_{eh} - Q_{rad,line} \tag{2.4}$$

$$\nabla \cdot \left(n_e\left(\frac{5}{2}k_B T_e + E_i\right)\vec{u}\right) = \nabla \cdot (k_e \nabla T_e) + \frac{5}{2}\frac{k_B}{e}\vec{j} \cdot \nabla T + \vec{j} \cdot \vec{E} - Q_{eh} - Q_{rad,cont} \quad (2.5)$$

where k_h and k_e are the thermal conductivities for heavy particles and electrons, respectively, n_e and $n_h$the electron and heavy particles number densities, respectively, E_i is the ionization energy and *e* the electron elementary charge.
Electron density has been calculated using the Saha equation for 2T systems assuming chemical equilibrium [17]; the energy exchange by collisions between electrons and heavy species Q_{eh} is calculated as in [19].
According to the model proposed in [26], the radiation contribution due to continuum emission ($Q_{rad,cont}$) has been set as a negative source for electrons, whereas the contribution due to line emission ($Q_{rad,line}$) has been implemented in the energy equations for heavy particles. The continuum contribution is due to free-free and free-bound interactions of electrons with heavy particles and ions and therefore it is associated with the electron energy equation, whereas line contribution is due to bound-bound electronic transitions and therefore the energy loss is attributed to heavy particles. Separate radiation contributions have been calculated using data from [29].
Non-equilibrium plasma thermodynamic and transport properties have been computed using the Rat approach as in [17].

The electromagnetic field for both the LTE and the 2T models is calculated using Maxwell's equations written explicitly for the vector potential $\vec{\mathbf{A}}$ and scalar potential $\mathbf{V}$. The vector and scalar potential equations are solved in the following form:

$$\nabla^2 \vec{A} - \mu_0 \sigma \vec{E} = 0 \quad (2.6)$$

$$\nabla \cdot (\sigma \nabla V) = 0 \quad (2.7)$$

where σ is the electrical conductivity and μ_0 is the magnetic permeability of free space; the electric field is related to the gradient of the scalar potential ($\vec{E} = -\nabla V$) and the current density has been calculated using the simplified Ohm's law, neglecting the Hall current $\vec{j} = \sigma \vec{E}$.
In the 2T model the Joule heating $\vec{j} \cdot \vec{E}$ is defined as

$$\vec{j} \cdot \vec{E} = \sigma \overrightarrow{E_p} \cdot \left(\overrightarrow{E_p} - \frac{k_B}{e} T_e \cdot \nabla ln\, n_e\right) \quad (2.8)$$

where $\overrightarrow{E_p}$ is the effective electric field, that can be derived from a simplified expression of the generalized Ohm's law as shown in [13].

A parabolic profile of the current density on the cathode surface is given as a boundary condition following

$$j(r) = -j_{max}\left[1 - \left(\frac{r}{R_0}\right)^2\right] \quad (2.9)$$

where j_{max} is the maximum value of the current density on the cathode, r is the distance from the axis of the cathode, R_0 is a reference value calculated imposing a given value of the total current I on the cathode surface. On the anode surface the electrical potential is assumed to be zero, while on all other surfaces the current flux is assumed to be zero.

The boundary condition for the vector potential $\partial\vec{A}/\partial\hat{n} = 0$ has been used on all the wall surfaces, $\hat{n}$ being the unit vector normal to the surface.
For the LTE model and for heavy particles in the 2T model a 1500K temperature is given as a boundary condition on the cathode; to allow a stable anode arc attachment an exponential temperature profile was imposed on the workpiece [30]:

$$T = 2700 \cdot e^{-\left(\frac{r}{r_0}\right)^8} + 300 \tag{2.10}$$

where r_0 is a geometric reference value. On all other surfaces the LTE and the heavy particles temperature is fixed at 300 K.
A 1500 K electron temperature is imposed on the cathode. A zero flux condition for T_e is imposed on all other wall surfaces. Argon flow rates and current are set according to experimental operating conditions reported in table 1.

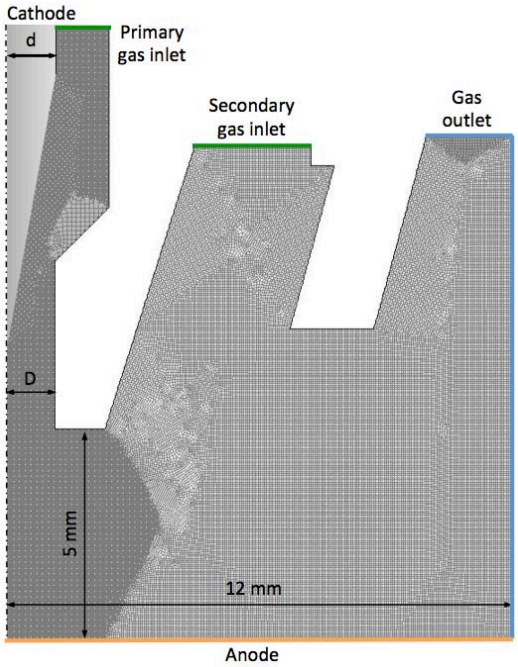

Figure 17 Schematic of the computational domain: cathode diameter (d) and nozzle diameter (D) are modified according to dimensions reported in table 1. [27]

4. Optical emission spectroscopy

4.1. Experimental setup

The experimental setup for the acquisition of the optical emission spectra (shown in figure 18) is composed of a 500 mm focal length monochromator (Princeton Instruments SP500i) connected with a iCCD camera (Princeton Instruments PIMAX3, 1024x1024 resolution) and of an optical system that focuses the arc image rotated by an angle of 90 degrees on the monochromator slit, in order to allow the acquisition of line-of-sight emission (along y axis) from different points along the lateral coordinate at the same time (x direction in figure 18). The optical system is composed of two focusing lenses that magnify three times the arc image, and of two movable mirrors that allow focusing on different axial positions of the arc. Neutral filters and pin holes have been adopted to reduce the emission intensity of the plasma arc. The monochromator has

been operated with a 1200 grooves/mm grating and the entrance slit has been set to 100 µm. The iCCD acquisition time (10-100 ms) has been regulated in order not to saturate the CCD sensor and to obtain a high signal to noise ratio.

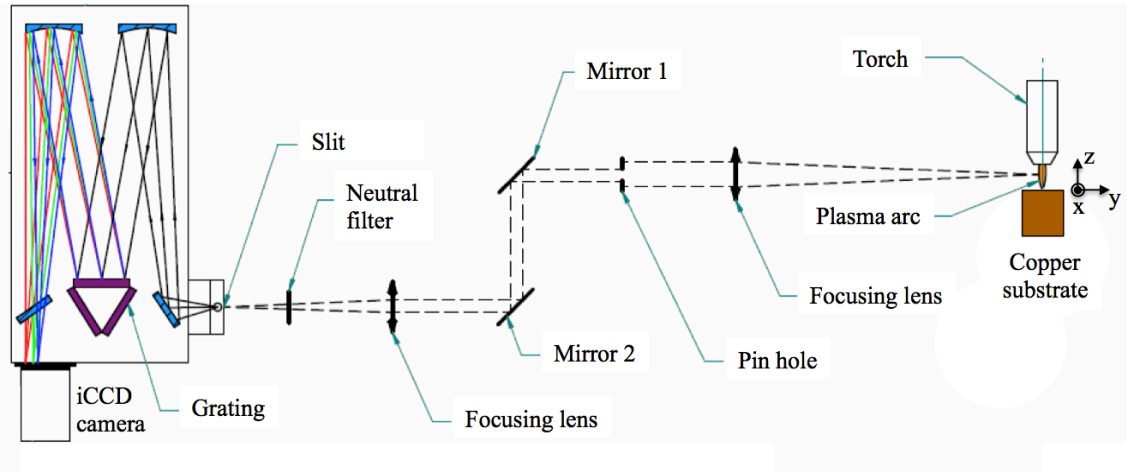

Figure 18 Schematic of the experimental setup for OES. [27]

4.2. Spectroscopic methods

It is known that under local thermodynamic equilibrium (LTE) conditions the number density $n_{j,u}$ of particles of the species j with optical electrons at energy level E_u is given by the Boltzmann distribution [21]:

$$n_{j,u} = n_j(T_{exc}) \frac{g_{j,u}}{Z_j(T_{exc})} \exp\left(-\frac{E_u}{k_B T_{exc}}\right) \tag{2.11}$$

where $n_j(T_{exc})$ is the total number density of species j calculated using Saha equation, perfect gas law and quasi-neutrality condition; $g_{j,u}$ is the statistical weight; $Z_j(T_{exc})$ is the internal partition function of the species j; k_B is the Boltzmann constant and T_{exc} is the excitation temperature linked to Boltzmann distribution of excited states.
The volumetric coefficient ε_λ of emission generated by electron transitions from the upper energy level E_u to the lower energy level E_l is characterized by an individual line in the emission spectrum with wavelength $\lambda_{j,ul} = hc/(E_u - E_l)$ and it is given by

$$\varepsilon_\lambda = \frac{1}{4\pi} \frac{hc}{\lambda_{j,ul}} A_{j,ul} n_{j,u} \tag{2.12}$$

where $A_{j,ul}$ is the transition probability, h and c are the Planck constant and the speed of light in vacuum, respectively.
A common approach to estimate the excitation temperature is to measure the volumetric emission coefficient of two lines ($\lambda_{1,ul}$ and $\lambda_{1,u'l'}$) of the same species and to use a *relative line intensity method* [23], which can be considered a special case of the Boltzmann plot method:

$$T_{exc} = \frac{E_{1,u'} - E_{1,u}}{k_B \ln\left(\frac{\varepsilon_\lambda \lambda_{1,ul} A_{1,u'l'} g_{1,u'}}{\varepsilon_{\lambda'} \lambda_{1,u'l'} A_{1,ul} g_{1,u}}\right)} \tag{2.13}$$

where u' and l' are the energy levels of the second emission line. With this method, the uncertainty $u(T_{exc})$ on excitation temperature is

$$\frac{u(T_{exc})}{T_{exc}} = \frac{k_B T_{exc}}{E_{1,u'} - E_{1,u}} \sqrt{\left(\frac{u(\varepsilon_\lambda)}{\varepsilon_\lambda}\right)^2 + \left(\frac{u(\varepsilon_{\lambda'})}{\varepsilon_{\lambda'}}\right)^2 + \left(\frac{u(A_{1,ul})}{A_{1,ul}}\right)^2 + \left(\frac{u(A_{1,u'l'})}{A_{1,u'l'}}\right)^2} \quad (2.14)$$

where $u(\varepsilon_\lambda)/\varepsilon_\lambda$ and $u(A_{1,ul})/A_{1,ul}$ are the uncertainties due to the experimental assessment of the volumetric emission coefficient and the ones related to the transition probability, respectively.
This method has been applied using two lines of the Ar atom (Ar I), with characteristic wavelength at 696.5 nm and 687.1 nm, respectively, which are widely used for diagnostics of argon thermal plasmas [23]. The spectroscopic constant for these two lines are reported in table 2.

Table 2 Spectroscopic constants for neutral argon lines used in this study.

Element	Wavelength (nm)	Upper energy level (eV)	Statistical weight	Transition probability (1/s)	Accuracy
Ar I	687.13	14.7108	3	4.0×10^6	±13% [23]
Ar I	696.54	13.3278	3	7.1×10^6	±11% [23]

In this frequency range, a strong noise may be found, which is mainly due to continuum radiation. When the signal to noise ratio (line to continuum radiation ratio) for the lateral emission is maximum on the axis of the plasma arc (s/n 80 and 5 for line at 696.5 nm and 687.1 nm, respectively), the uncertainty for volumetric emission coefficient is estimated around 10% and 15% for line at 696.5 nm and 687.1 nm, respectively. However, in the fringes of the arc, the emission at 687.1 nm is weaker and the s/n ratio is lower, leading to a too high uncertainty on temperature calculation using the relative line intensity method.
For the calculation of T_{exc} in the fringes of the arc, an *absolute intensity method* [23] based on the use of only the line at 696.5 nm (characterized by a higher s/n ratio also in the fringes of the arc) could be used; once the absolute calibration of the acquisition setup has been carried out using a calibrated light source. Also, if the temperature in the center of the arc is sufficiently high so that the radial volumetric emission profile is characterized by an off-axis peak, the temperature can be calculated using a *norm temperature method* [22], without requiring absolute calibration of the measurement system. However, this method can be used only when the maximum temperature is higher than the norm temperature, which is around 15000 K for the Ar I lines.
In order to take advantage of the absolute intensity method without complicating the optical setup with the use of a calibrated lamp, the central region of the arc was used as a calibrated light source: the excitation temperature on the axis $T_{exc}(0)$ is calculated with the relative line intensity method using the lines at 696.5 nm and 687.1 nm and the resulting temperature is used to calculate the volumetric emission coefficient of the line at 696.5 nm in the same position, $\varepsilon_\lambda(0)$, using formulas 11 and 12 (see figure 19, profile for non-equilibrium parameter θ = 1); for temperatures lower than the norm temperature, the absolute intensity has a bi-univocal relationship with the excitation

temperature ($T_{exc} \Leftrightarrow \varepsilon_\lambda$) and the radial profile of the latter can be calculated from the radial profile of the absolute volumetric emission coefficient, which is calibrated using the following expression

$$\varepsilon_\lambda(r)\left[\frac{W}{m^3\,ster}\right] = \frac{\varepsilon_\lambda(r)[a.u.]}{\varepsilon_\lambda(0)[a.u.]}\,\varepsilon_\lambda(0)\left[\frac{W}{m^3\,ster}\right] \tag{2.15}$$

This method will be called in the remaining part of the paper *"hybrid method"*. The uncertainty related to this method is estimated from the uncertainty of the measurement of $T_{exc}(0)$.

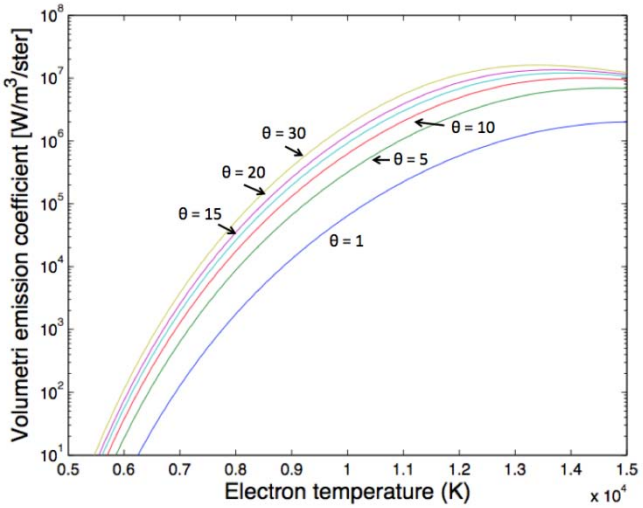

Figure 19 Volumetric emission coefficient of the Ar I line at 696.5 nm as a function of electron temperature T_e, for different values of the non-equilibrium parameter $\theta = T_e/T_h$.[27]

The absolute intensity method and the hybrid method are strictly valid only for LTE. In case thermal non-equilibrium exists, the volumetric emission coefficient is a function of electron translational temperature T_e, excitation temperature T_{exc} and heavy particle translational temperature T_h as follows

$$\varepsilon_\lambda = \frac{1}{4\pi}\frac{hc}{\lambda_{j,ul}}A_{j,ul}\,n_j(T_e,T_{exc},T_h)\frac{g_{j,u}}{Z_j(T_{exc})}\exp\left(-\frac{E_u}{k_B T_{exc}}\right) \tag{2.16}$$

However, for the calculation of the emission coefficient, $T_{exc} \approx T_e$ can be assumed [23], leading to

$$\varepsilon_\lambda = \frac{1}{4\pi}\frac{hc}{\lambda_{j,ul}}A_{j,ul}\,n_j(T_e,T_h)\frac{g_{j,u}}{Z_j(T_e)}\exp\left(-\frac{E_u}{k_B T_e}\right) \tag{2.17}$$

Results for the volumetric emission coefficient of the Ar I line at 696.5 nm are reported in figure 19 for different values of the non-equilibrium parameter, $\theta = T_e/T_h$.
If the non-equilibrium parameter can be estimated (e.g. from modelling), it is possible to calculate the error in neglecting thermal non-equilibrium in the computation of volumetric emission coefficient in the hybrid method: for fixed non-equilibrium parameter, there exist a bi-univocal relation between ε_λ and T_e (see figure 19), and electron temperature can be estimated from the measured absolute intensity of the volumetric emission coefficient of the hybrid method. With this method the error on

temperature neglecting non-equilibrium in the calculation of composition was estimated to be less than 10% for $\theta = 10$, which is an overestimation of the non-equilibrium parameter encountered in the spatial region investigated with OES in this paper.

4.3. Elaboration of spectroscopic raw data

The raw spectrum in the wavelength range 680-700 nm is composed of emissions from 687.1 nm and 696.5 nm lines and of the continuum emission. In order to distinguish between continuum and line contributions, the broadened line intensity profiles $I(y,\lambda)$ are fitted with a Lorentz function for each lateral position *y*. The intensity of the fitted Lorentz function is used to calculate the lateral emission intensity profile $I_\lambda(y)$ for each line. The latter is fitted with a Gaussian function and it is converted to radial volumetric emission coefficient $\varepsilon_\lambda(r)$ using the analytical expression of the Abel inversion for the Gaussian function. Self-absorption of the adopted lines is not taken into account in the elaboration of data since absorption in the visible and near infrared spectral region is negligible [31].

5. Results

The plasma arc welding process has been analyzed using LTE and 2T models and optical emission spectroscopy in order to characterize the process at three different current levels (25, 40 and 70 A) and test the proposed OES method.

5.1. LTE modelling of the arc in the plasma arc welding process

Results for temperature and velocity fields obtained using the LTE model have been reported in figure 20. The temperature field outside the nozzle has a shape that is typical for a free-burning arc working in the diffuse mode [32]: when the arc is not constricted, the plasma flow expands radially due to diffusion and, in the region close to the workpiece, the enthalpy of the arc is transported radially by thermal conduction to the outer region resulting in a typical bell shape. Inside the nozzle, the arc is constricted and stabilized by the cold gas flowing near the wall surface and by the nozzle wall itself. The constriction of the arc is most pronounced for the case at 40 A: in this case and at 25 A, the maximum temperature is obtained at the nozzle outlet, where the constriction/stabilization effects are maximum. The increase in temperature in the constricted part of the arc is mainly due to higher electric field and therefore higher joule dissipation. For the case at 70 A, the constriction effect is lower due to the larger nozzle orifice and the temperature maximum is localized near the cathode tip, as it is usual for free-burning arcs. It should be noted that the maximum temperature is higher for the 40 A case than for 70 A; even if the current is higher, typical operating conditions at 70 A involve the use of a nozzle with larger orifice, that results in a lower mean current density (the ratio of total current and nozzle orifice area): for the case at 40 A, the mean current density is about 20 A/mm^2, whereas for the 70 A case it is about 15 A/mm^2. These values are way lower than typical mean current densities typical for plasma arc cutting applications (from 50-60 A/mm^2 to more than 90 A/mm^2 for high definition cutting torches) [33, 34].
Plasma velocity reaches its maximum (around 1200 m/s for the 40 A case) at the point with highest temperature, where the density of the gas reaches its minimum. The constriction of the arc induces higher velocities than those obtained in typical free-burning gas metal arc welding processes. However, the maximum velocity is below the speed of sound for local temperature conditions, resulting in an uncompressible fluid

behaviour. The maximum velocity for the case at 40 A is comparably higher than that of the 70 A case, as the increase in current and flow rate has a lower effect than the increase in the orifice cross section. For the case at 25 A, the lower current intensity induces a lower mean plasma temperature and consequently a lower gas velocity than for the 40 A case.

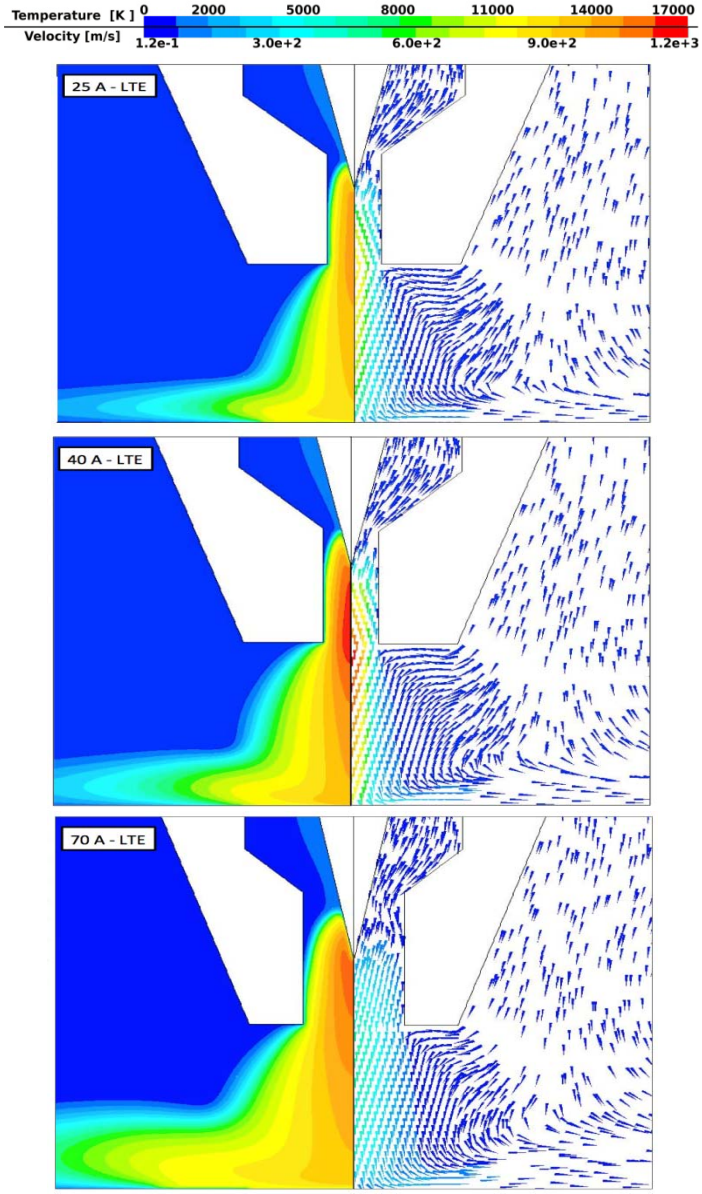

Figure 20 Temperature field (left) and velocity vectors (right) at different current levels, when using the LTE model. [27]

5.2. 2T modelling of the arc in the plasma arc welding process

While for plasma arc at high current levels (>100A) thermal non-equilibrium is mainly found in the fringes of the arc [26], low current arcs (lower than 50 A) can be characterized by a strong thermal non-equilibrium also in the central part of the arc, as shown for a free-burning gas metal arc welding process by Tashiro et al. [35] using two-temperature modelling. In this paragraph results are reported (see figures 21 and 22) for the plasma arc welding process at low currents using a 2T modelling approach.

As can be seen in figure 21, the heavy particle temperature is characterized by a spatial distribution similar to the one obtained using the LTE model. However, the electron temperature (figure 22) is characterized by a larger spread in the radial direction outside the nozzle and upstream the plasma flow in the primary gas channel. This behaviour is similar to those reported in literature for other plasma processes [14, 26, 35]. In figure 22, it can be seen that the non-equilibrium parameter reaches values up to 23 in the fringes of the arc. The velocity field obtained using the 2T model is similar to that obtained using the LTE model, even if the absolute value of the velocity is lower for the 2T model as a consequence of the slightly lower temperature obtained (see figure 21).
It is worth noting that for the plasma arc welding process the electron temperature is higher than that of heavy particles also inside the plasma arc, both in the nozzle region and outside the nozzle. In the region inside the nozzle, the non-equilibrium parameter is higher than 1 as a consequence of the interaction of the supplied cold gas with the arc column, which induces mainly the cooling of heavy particles while electrons remains at high temperature. This is most evident for the case at 40 A, whereas for the case at 70 A, thermal equilibrium is almost reached inside the arc. The maximum electron temperature for the case at 40 A is 16400 K and it is located at the nozzle outlet, whereas the heavy particle temperature maximum is 16000 K. This is mainly due to the unbalance of electron heating by Joule effect and collisional term of energy transfer from electrons to heavy particles: as a consequence of the high velocity of the gas flow reached in the wall constricted arc, the transport of electron energy outside the nozzle by convection is predominant with respect to the energy transfer to heavy particles. Also, the smaller nozzle radius in the case at 40 A induces a higher cooling of the heavy particles in the nozzle region with respect to the case at 70 A.

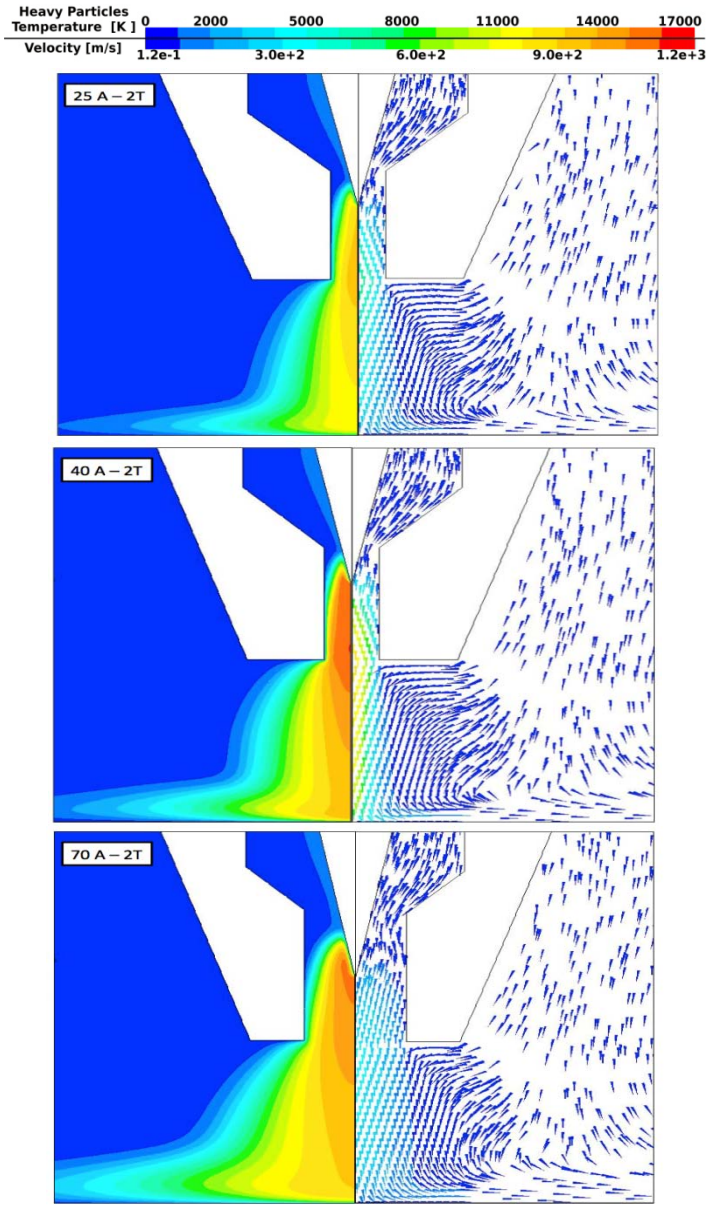

Figure 21 Heavy particle temperature field (left) and velocity vectors (right) of the plasma arc welding process at different current levels, when using the 2T model. [27]

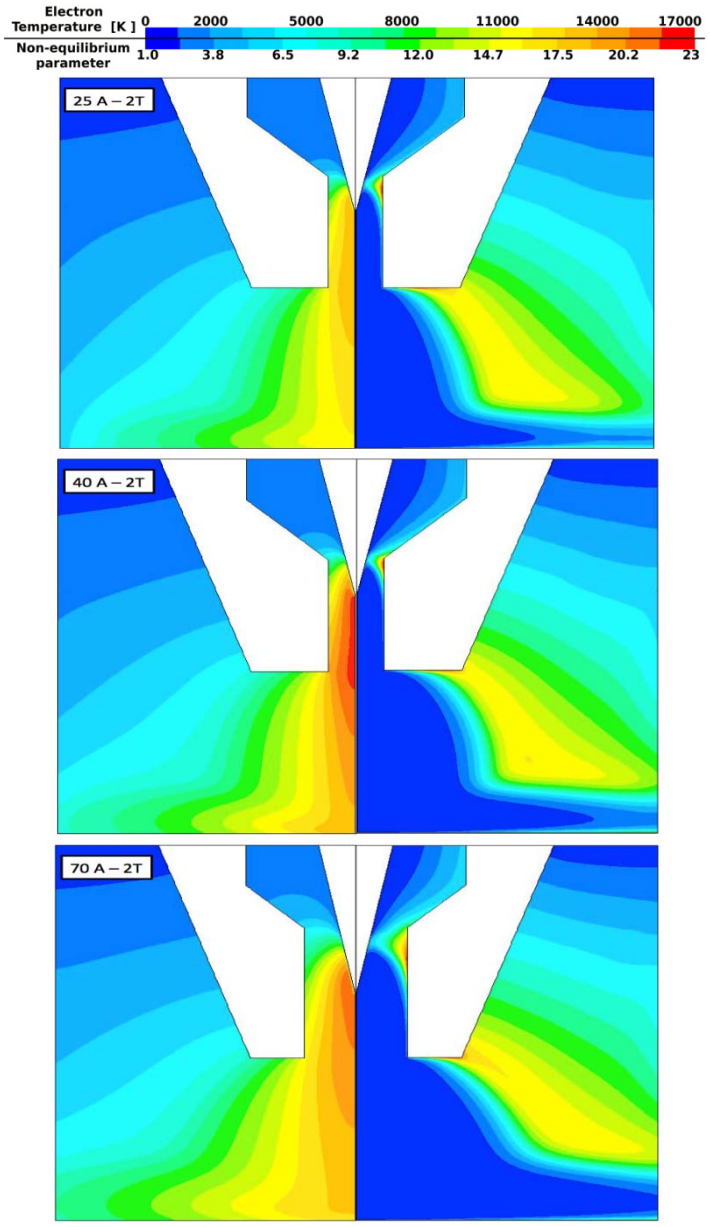

Figure 22 Electron temperature field (left) and non-equilibrium parameter (right) of the plasma arc welding process at different current levels, when using the 2T model. [27]

5.3. Optical emission measurement of excitation temperature and comparison with modelling

The excitation temperature field has been determined from OES measurements using the hybrid method proposed in paragraph 4. Different axial positions have been scanned from 0.5 mm to 4.5 mm from the workpiece, with an axial spatial resolution of 0.5 mm. Two-dimensional contours have been obtained by linear fitting of the data at different radial and axial positions and they are reported in figure 23, together with electron temperature fields obtained from 2T modelling. A good agreement has been found between the OES measurement of the excitation temperature and the electron temperature obtained from 2T modelling. These results are in line with the common assumption that the bounded electron population follows a Boltzmann distribution on

excited states of atoms with an excitation temperature close to the electron translation temperature [23].
However, some discrepancies have been found in the vicinity of the workpiece, where possible emission of copper vapours from the substrate, not taken into account in the model, may have cooled the plasma arc during the OES acquisitions. The influence of vapours is mostly seen for the case at 70 A, whereas for the lowest current level the agreement is quite satisfactory, also in the vicinity of the workpiece.

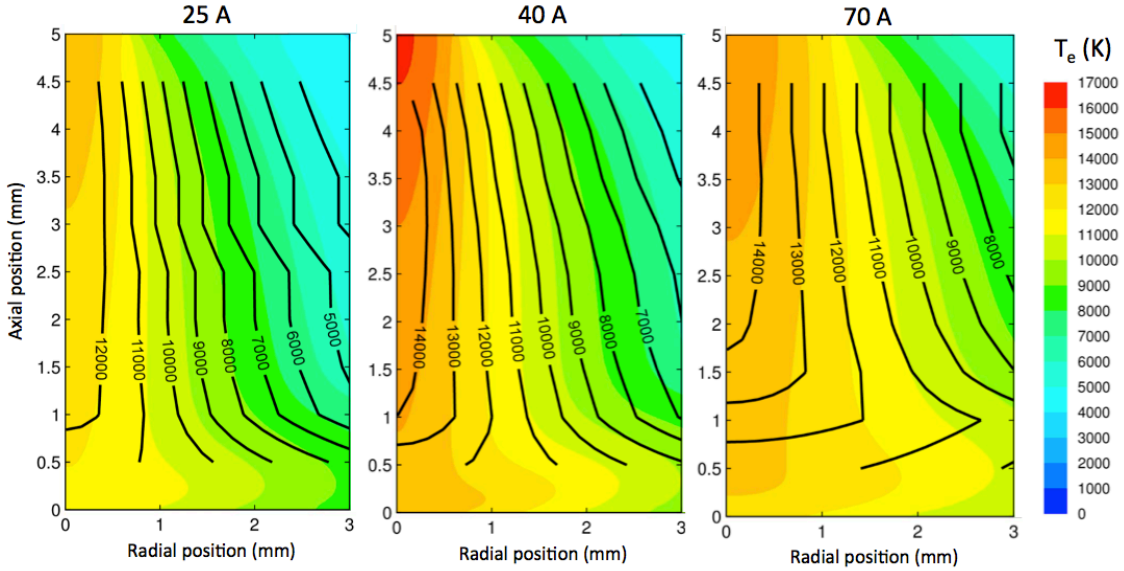

Figure 23 Comparison of the excitation temperature field obtained using optical emission spectroscopy (black lines contours) and the electron temperature field obtained using simulations with 2T models (colour filled contours) for the plasma arc welding process at different current levels. [27]

In figures 24, 25 and 26, a detailed comparison of the radial profile at different axial positions of the temperatures obtained with the three methods used in this work (LTE model, 2T model and OES) have been plotted for the case at 25 A, 40 A and 70 A, respectively.
It is evident from these figures that the excitation temperature obtained using OES is close to the electron temperature obtained with the 2T model (the electron temperature is inside the uncertainty range of OES measurements for the whole analysed region), while the equilibrium temperature obtained in the LTE model is similar to the heavy particle temperature resulting from the 2T model.
At z = 4.5 mm from the workpiece, the arc is mostly constricted with a Gaussian temperature profile, and it expands radially as it approached the workpiece (z = 2.5 and 0.5 mm). The electron temperature has generally a larger profile with respect to heavy particle temperature, whereas at z = 0.5 mm the profiles of LTE electron and heavy particle temperatures are almost the same.
It is worth noting that 2T modelling and OES hybrid method resulted independently in a similar profile for electron temperature and excitation temperature for all the cases investigated in this work, suggesting that the hybrid method can be used for characterization of thermal plasma arcs with temperatures lower than the *norm* temperature.

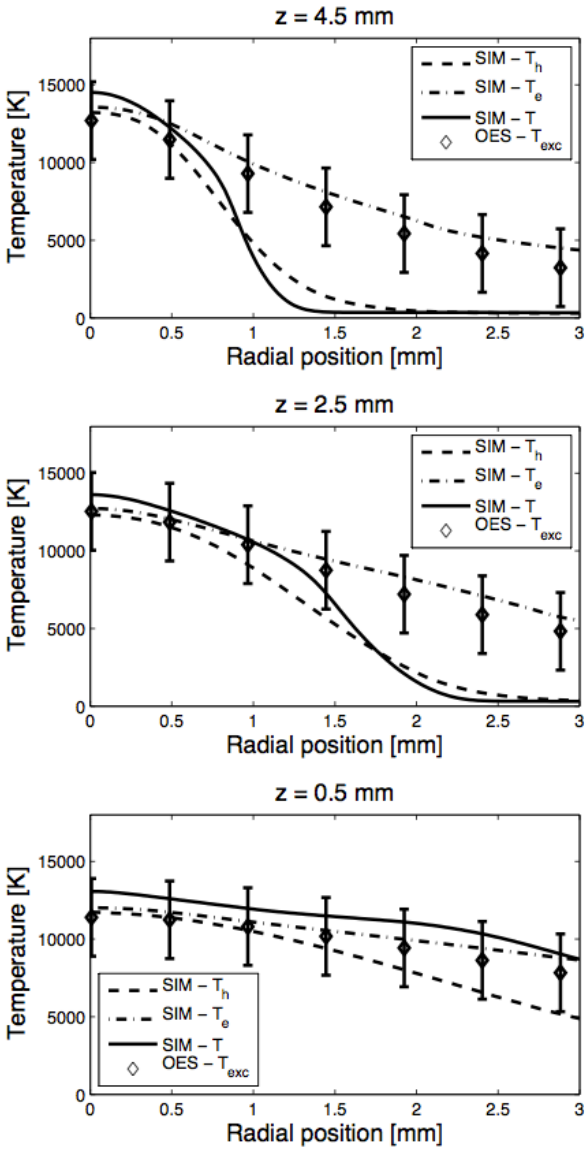

Figure 24 Comparison of the radial temperature profile at different axial positions obtained using optical emission spectroscopy (T_{exc}) and simulations with LTE (T) and 2T (T_h and T_e) models for the plasma arc welding process at 25 A. [27]

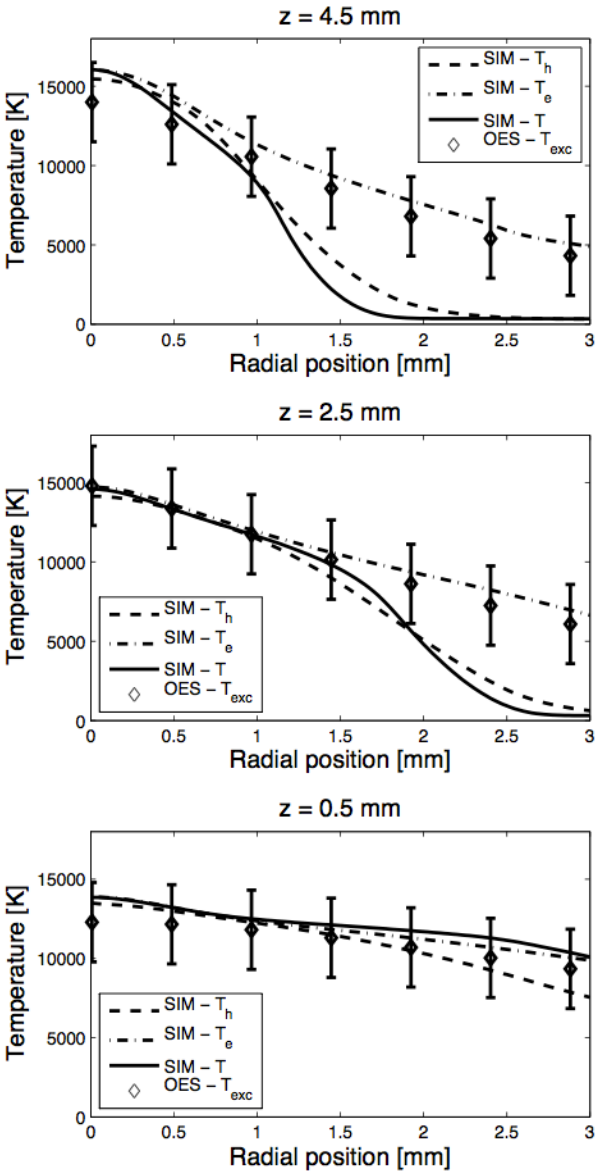

Figure 25 Comparison of the radial temperature profile at different axial positions obtained using optical emission spectroscopy (T_{exc}) and simulations with LTE (T) and 2T (T_h and T_e) models for the plasma arc welding process at 40 A. [27]

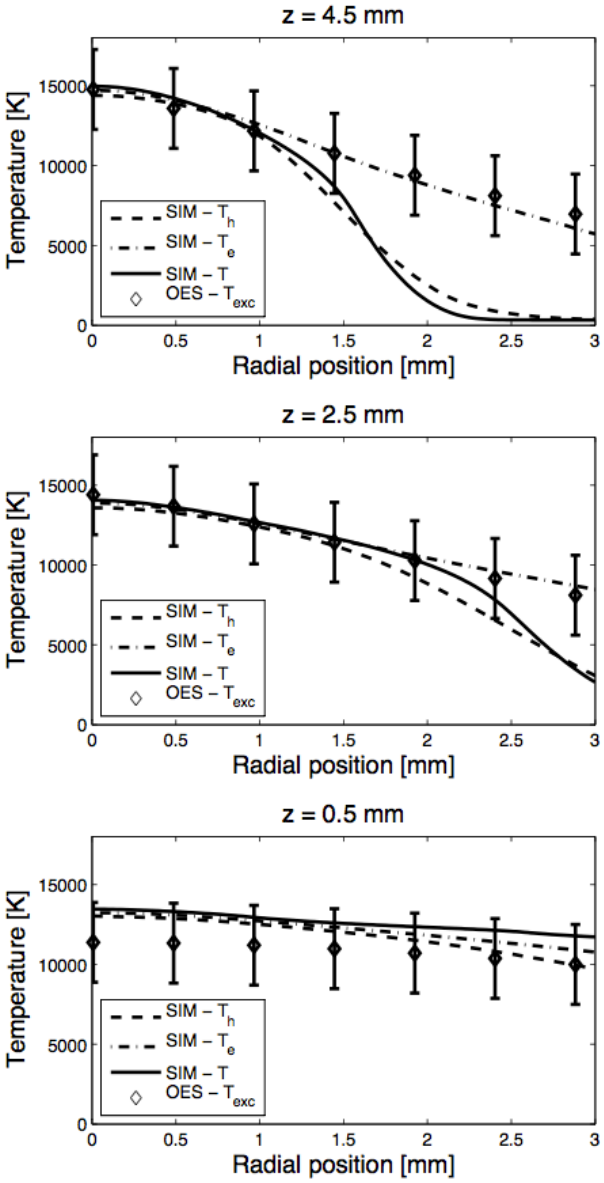

Figure 26 Comparison of the temperature profile at different axial positions obtained using optical emission spectroscopy (T_{exc}) and simulations with LTE (T) and 2T (T_h and T_e) models for the plasma arc welding process at 70 A. [27]

6. Conclusions

The thermal plasma arc in a constant current plasma arc welding process obtained using a commercial industrial torch has been characterized using LTE and 2T modelling together with optical emission spectroscopy. LTE, heavy particle and electron temperature have been obtained from modelling, whereas the excitation temperature of Ar atoms has been obtained from OES measurements using a new method, called *hybrid method*, that has been proposed to extend the usability of the Boltzmann plot method to spatial regions where the uncertainty of the latter is too large due to poor signal to noise ratio of the involved spectral lines. A good agreement has been obtained between the excitation temperature and the electron temperature radial profiles at different axial positions and for different current levels and a complete characterization

of the plasma torch operating in standard operating conditions has been carried out. Further investigations for the improvement of the design of plasma arc welding processes at constant current and for the characterization of different plasma arc welding processes, like AC-PAW, will take advantage of the methods proposed and exploited in this work.

References

[1] Lancaster J F, The physics of welding, Oxford: Pergamon Press (1986)
[2] Dowden J and Kapadia P, Journal of Physics D: Applied Physics, **27** 902 (1994)
[3] Fuerschbach P and Knorovsky G, Welding Journal(USA) **70** 287 (1991)
[4] DuPont J and Marder A, Welding Journal-Including Welding Research Supplement **74** 406 (1995)
[5] Bashenko V V and Sosnin N A, Weld J **67** S233-S7 (1988)
[6] Dowden J and Kapadia P, J Phys D Appl Phys **27** 902-10 (1994)
[7] Schnick M, Fussel U and Spille-Kohoff A, Weld World **54** R87-R96 (2010)
[8] Zhang T, Wu C S and Chen M A, Acta Metall Sin **48** 1025-32 (2012)
[9] Gleizes A, Gonzalez J J and Freton P, Journal of Physics D: Applied Physics **38** R153-R83 (2005)
[10] Murphy A B, Boulos M I, Colombo V, Fauchais P, Ghedini E, Gleizes A, Mostaghimi J, Proulx P and Schram D C, High Temperature Material Processing **12** 255-336 (2008)
[11] Peters J, Bartlett B, Lindsay J and Heberlein J, Plasma Chemistry and Plasma Processing **28** 331-52 (2008)
[12] Colombo V, Concetti A, Ghedini E, Rotundo F, Sanibondi P, Boselli M, Dallavalle S, Gherardi M, Nemchinsky V and Vancini M, Plasma Chemistry and Plasma Processing **32** 411-26 (2012)
[13] Trelles J P, Heberlein J V R and Pfender E, Journal of Physics D: Applied Physics **40** 5937-52 (2007)
[14] Ghorui S, Heberlein J V R and Pfender E, Journal of Physics D: Applied Physics **40** 1966-76 (2007)
[15] Trelles J P, Chazelas C, Vardelle A and Heberlein J V R, J Therm Spray Tech **18** 728-52 (2009)
[16] Rat V, André P, Aubreton J, Elchinger M F, Fauchais P and Lefort A, Physical Review E - Statistical, Nonlinear, and Soft Matter Physics **64** 264091-2640920 (2001)
[17] Colombo V, Ghedini E and Sanibondi P, Journal of Physics D: Applied Physics **42** 055213 (2009)
[18] Colombo V, Ghedini E and Sanibondi P, Plasma Source Sci. Technol **20** 035003.(2011)
[19] Colombo V, Ghedini E, Boselli M, Sanibondi P and Concetti A, Journal of Physics D: Applied Physics **44 (**2011**)**
[20] Rat V, Murphy A B, Aubreton J, Elchinger M F and Fauchais P, Journal of Physics D: Applied Physics **41** 183001 (2008)
[21] Griem H R, Plasma Spectroscopy, New York: McGraw-Hill (1964)
[22] Peters J, Heberlein J V R and Lindsay J, Journal of Physics D: Applied Physics **40** 3960 (2007)
[23] Bussière W, Vacher D, Menecier S and André P, Plasma Sources Science and Technology **20** 045004 (2011)
[24] Hartmann R M and Heberlein J V, J Phys D Appl Phys **34** 2972-8 (2001)

[25] Valensi F, Pellerin S, Boutaghane A, Dzierzega K, Pellerin N and Briand F, Contrib Plasm Phys **51** 293-6 (2011)
[26] Freton P, Gonzalez J J, Ranarijaona Z and Mougenot J, Journal of Physics D: Applied Physics **45** 465206 (2012)
[27] Boselli M, Colombo V, Ghedini E, Gherardi M and Sanibondi P, J. Phys. D: Appl. Phys. **46** 224009 (2013) © 2013 IOP Publishing
[28] Lowke J J, Journal of Quantitative Spectroscopy and Radiative Transfer **14** 111-22 (1974)
[29] Cressault Y, Rouffet M E, Gleizes A and Meillot E, J Phys D Appl Phys **43** (2010)
[30] Murphy A B, Tanaka M, Yamamoto K, Tashiro S, Sato T and Lowke J J, J. Phys. D: Appl. Phys. **42** 194006 (2009)
[31] Boulos M I, Fauchais P and Pfender E, Thermal Plasmas: Fundamentals and Applications, New York: Plenum Press (1994)
[32] Yang G and Heberlein J, Plasma Sources Science and Technology **16** 529 (2007)
[33] Colombo V, Dallavalle S, Ghedini E, Masini G, Russo D and Vancini M, J. High Temp. Mater. Proc. **10** 379 (2006)
[34] Cantoro G, Colombo V, Concetti A, Ghedini E, Sanibondi P, Zinzani F, Rotundo F, Dallavalle S and Vancini M, Journal of Physics: Conference Series **275**(2011)
[35] Tashiro S, Iwao T, Inaba T, Murphy A B and Tanaka M, Plasma Science, IEEE Transactions on **36** 1070-1 (2008)

CHAPTER 3
Plasma arc cutting: high-speed imaging of process instabilities

1. Introduction

Plasma arc cutting (PAC) is a process for cutting metallic sheets with typical thickness in the range 1-50 mm in which a thermal plasma arc is ignited between a thermionic cathode that is enclosed in the plasma torch and the workpiece which works as the anode [1].
Research efforts in the last decades have been mainly focused on the improvement of the quality of the cut, on the increase of the maximum cutting speed and the reduction of the wear rate for torch consumables. Significant results have been achieved in cut quality and speed, leading to the possibility of cutting mild steel with thickness up to 50 mm at a speed of 0.8 m/min for a 400A torch and to high-definition cutting for lower thicknesses (<30 mm). However, cathode erosion and torch consumable wear still represents a challenge that limits the up-scaling of plasma cutting device to higher current levels [1-3].
The design of plasma arc cutting devices requires a deep understanding of the influence of the operating conditions, torch geometries and materials on the physical phenomena occurring during torch operations. The optimization of these devices is often pursued using an integrated approach that includes the analysis of results coming from experimental evidences, optical and electrical diagnostics and computational modelling [4].
Many works have been reported in literature on the investigation of cathodic processes and involved erosion mechanisms [4-12] using ex-post pictures of a series of transitory conditions occurred during one (or more) cutting cycle(s), while experimental erosion tests and microstructural analysis are required for quantitative analysis of electrodes wear rate. Besides, high-speed imaging techniques have allowed a deeper comprehension of transient phenomena occurring during different cutting phases that mainly impact cathode erosion, like electrode behaviour during current ramp-up and shut-down and stabilization on the pilot arc attachment on cathode insert on used electrodes [13-15].
In this chapter, high-speed imaging investigations of selected transient phenomena that induce wear of torch consumables, for different torch configurations are reported. In particular, high-speed imaging sequences for the pilot arc start-up and shut-down phase are presented for cathodes of different material and shape of the initial recess that are known to have a strong influence on the cyclic erosion mechanisms [1, 4, 6]. In particular, two phenomena for which no results have been reported in literature were investigated: the influence of the depth of the initial recess on the transition time from ignition to a stable arc attachment on the center of the emitter surface and the influence of the thermionic emitter material (e.g the use of Ag-Hf mixture as insert material) on shut-down erosion. Also, it was investigated the start-up and shut-down transients by high-speed imaging during torch operation in transferred arc mode on a graphite anode, by removing the shield cup and by using a modified nozzle, as shown in [6], characterized by the presence of a viewing port at one side of the nozzle.
Moreover, results are presented concerning the effects of swirl flow during the pilot arc start-up phase and during the cutting phase: the former must be investigated for the optimization of the torch operating conditions in terms of reduction of the wear rate of

the nozzle internal surface, whereas the study of the latter can provide a deeper insight for the improvement of cut quality and the reduction of cathode erosion during the cutting phase. The results presented in the following pages have been published in [16].

2. Experimental setup

2.1 Plasma sources

For experimental tests reported in section 3.1, 3.2, 3.3 and 3.4 a Cebora S.p.A. plasma cutting system was used, comprising a power supply Plasma Prof 264 HQC, equipped with a remote high-frequency unit HV18 and a Gas Console PGC1-2 for manual gas settings, together with a multi-gas plasma torch CP251G. The system can operate in the current range 25–250 A in controlled current mode. These experiments were carried out under operative conditions typically used in the cutting of mild steel (MS) plates thicker than 20 mm, with air as both plasma and shield gas. In the considered pilot arc phase the arc current is fixed at 25 A; the signal of the voltage drop between the electrode and the nozzle has an average value of 150 V with fluctuations of about ±30 V. The tested electrodes use a press fit Hf based insert with a diameter of 2 mm working in association with a nozzle with a 1.9 mm diameter orifice.
In section 3.4, the electrodes combining powders of a high thermal conductibility (Cu, Ag) and high thermionic emissivity (Hf, Zr) materials were used. In particular, one electrode with a 50%-50% by weight Cu-Zr alloy insert composition and one with a 50%-50% by weight Ag-Hf alloy insert composition were tested.
For the experiments reported in section 3.5, a mono-gas plasma torch (CP101) with a power supply Cebora Plasma 100 has been used under typical operative conditions for 20 mm MS plates cutting with air plasma gas. During the arc initiation phase, the arc current varies linearly between 25 and 160 A. The tested electrodes use a press fit Hf based insert with a diameter of 2 mm working in association with a nozzle with a 1.8 mm diameter orifice.

2.2 High-speed imaging setup

A High speed camera Memrecam GX-3 (NAC Image Technology) with a maximum acquisition speed of 200,000 fps has been used equipped with a 180 mm focal-length lens protected by a protective neutral filter, at a distance of about 0.5 m from the plasma torch, joined with a digital oscilloscope LT374M (Teledyne Lecroy) (figure 27). Visualization of the cathode surface during pilot arc was accomplished by positioning the torch and the camera lens coaxially to the nozzle orifice or to a viewing port on the side of the nozzle, so to have a free axial line-of-sight from the insert surface to the camera (figure 28). The camera set-up has been selected with frame rate and shutter time up to 100,000 fps and 1/333,000 s, respectively, in order to achieve the best compromise between camera acquisition speed and image resolution.
In all experiments auxiliary lighting has been used only in the setting phase, in order to facilitate the focusing procedure, while the images have been captured without any filtering.
For all the cases, the image acquisition was synchronized with operating current waveform acquisition in order to create an evident link between the typical behaviour of the pilot arc and the arc voltage waveform.

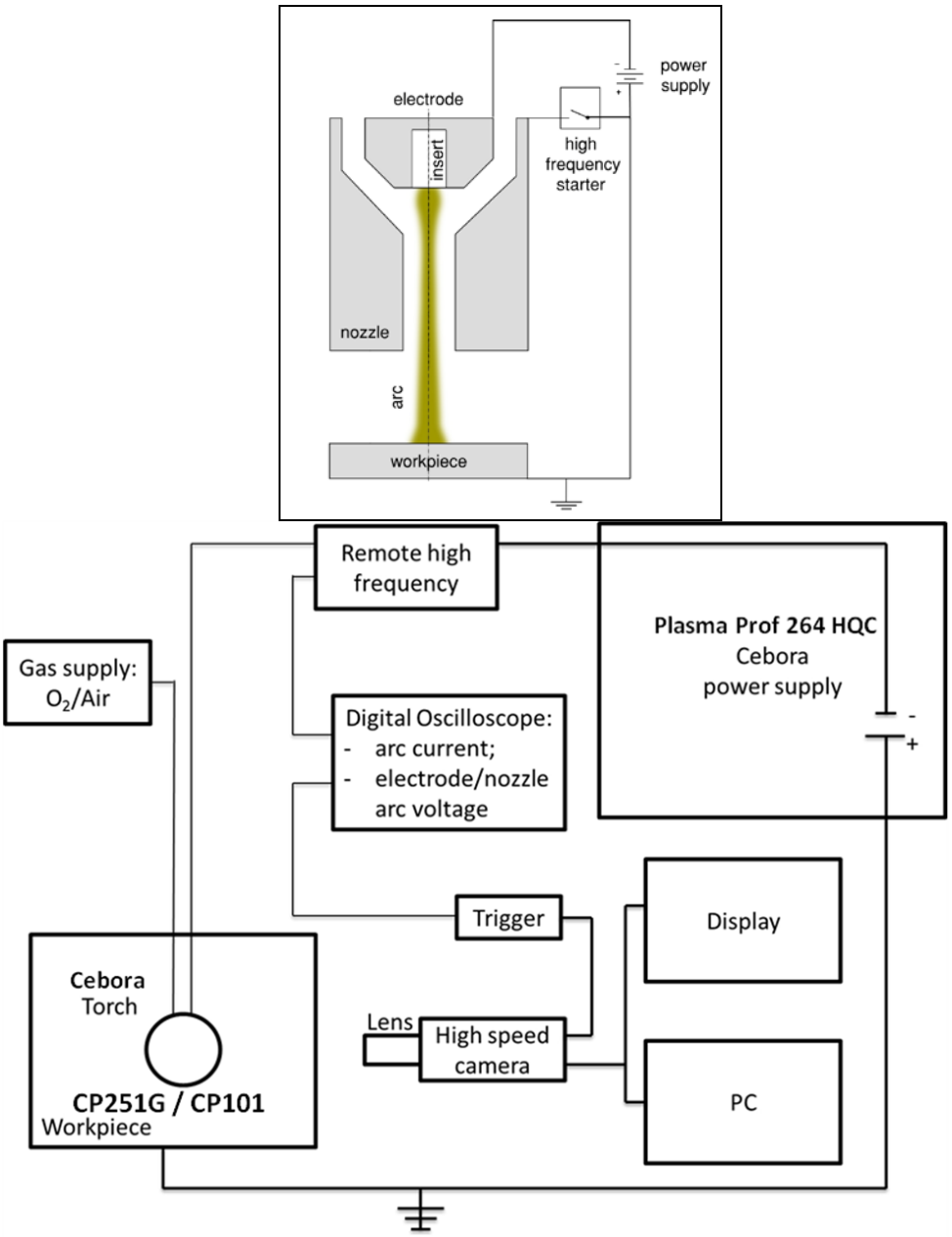

Figure 27 Scheme of the plasma torch (top) and of the visualization set-up for high-speed imaging (bottom). [16]

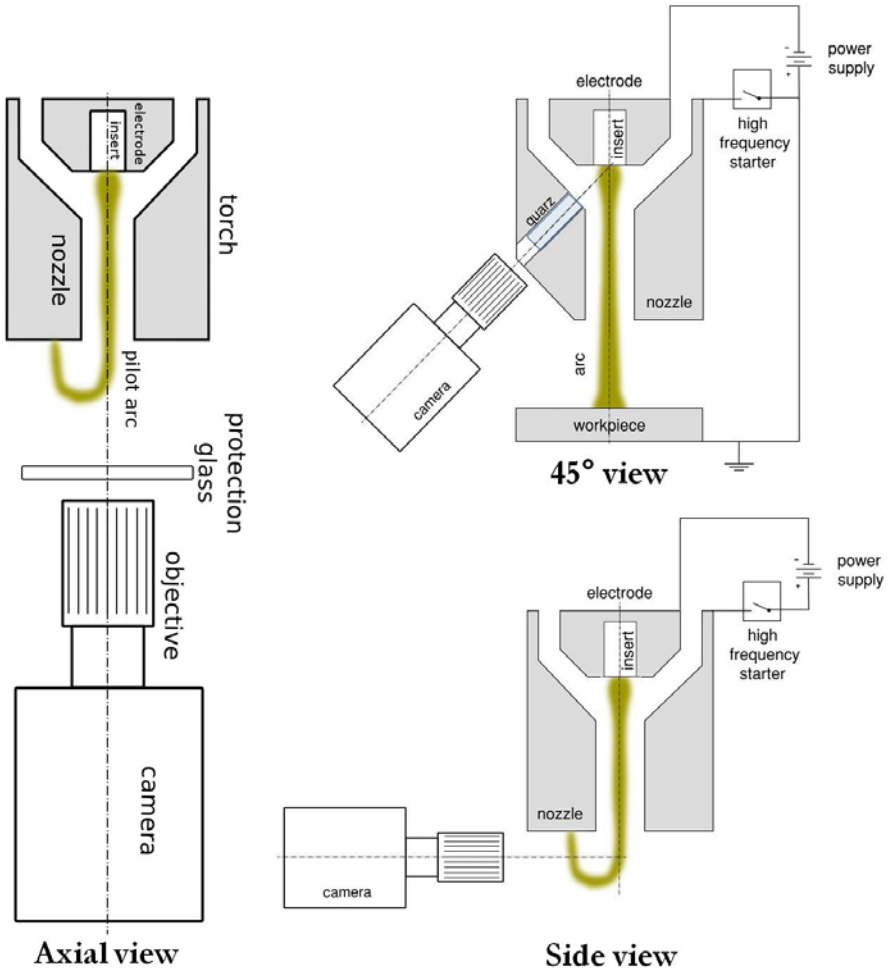

Figure 28 Scheme of the experimental set-up with different view points for high-speed visualization of pilot arcing transient. [16]

3. Results

The frames from high speed imaging recordings that are reported in the next sections have been selected with the aim of describing the observed phenomena. These phenomena are repeatable with the same torch geometry and operating conditions, even if the random behaviour of the plasma arc induces every recording to be slightly different from the others. The reported frames are representative of the investigated phenomena.

3.1 Behaviour of Hf cathodes with different depths of the initial recess during pilot arc start-up transient

In a previous paper [14], it was shown that the pilot arc process is characterized by two subsequent phases: in the first one, the cathode arc root rotates at the periphery of the emitter surface inducing emission of Hf vapours; in the second phase, the cathode attachment is no more rotating at the periphery of the emitter surface and the arc column stabilizes in its centre. The time required for the transition from the first pilot arc phase to the second one was reported to be 12 ms and 175 ms for brand new and used electrodes, respectively. The different behaviour has been attributed to differences

in thermal diffusivity of the emitting surface material, being pure Hf for the brand new electrode and hafnium oxide for the used electrode. However, the used and the brand new electrodes were also characterized by a different depth of the recess and this aspect was not taken into account in the discussion of the results.
In this section, results are reported for experiments carried out with the same operating conditions reported in [14] in order to clarify the effect of the depth of the initial recess (with flat square surface) on the time required for stabilization of the arc root at the center of the Hf cathode. A greater depth of the recess is expected to modify the fluid dynamics on the electrode surface. In order to clarify the importance of the recess depth on the transition time, the pilot arc start-up transition in a dual-gas CP251G torch with electrodes machined on purpose with flat square surface (using a square end mill) but with different depths of the initial recess has been recorded using the high-speed imaging setup reported in figures 27 and 28. In this case, the surface of the emissive insert is pure Hf. Tests have been performed for electrodes with flat surface with 0.4, 0.8 and 1.2 mm of recess depth; for each electrode three different recordings have been done in order to verify the reproducibility of the results. Results for the transition time as a function of the recess depth of the cathode are reported in figure 29, whereas selected frames of the high-speed recording are reported in figure 30.
As can be seen in results reported in figure 29, the transition time for different recess depth is almost constant with a mean value of 4 ms, confirming the discussion reported in [14] in which the reason for a longer transition time in used electrodes was attributed not to the greater depth of the recess but to the different thermal properties of the emitter surface material. These results demonstrate that the fluid dynamics changes caused by the recess depths are negligible compared to the thermal diffusion phenomena.
Selected high-speed imaging frames for the case with 1.2 mm depth of the initial recess are reported in figure 30. In this figure, the circular region that can be seen is the insert surface delimited by the nozzle orifice; the remaining part of the figure, which is mostly dark, is the nozzle external surface. The high-frequency signal occurs at t = 0 ms and the arc is struck between the nozzle inner surface and the copper part of the electrode. The frame at t = 1.75 ms shows the arc column deflected by the swirl component of the gas while it is blown out from the nozzle; in this frame the arc attachment on the electrode is not visible. The arc is blown out from the nozzle at t = 1.8 ms and the green spot caused by copper evaporation near the arc root on the nozzle tip can be seen at t= 1.89 ms; the bright central spot that can be seen starting from the frame at t = 1.89 ms is the arc pilot column. At t = 2.82 ms the cathode arc root starts to rotate at the periphery of the hafnium insert, as can be seen from the grey-blue emission. From t = 3 ms to t = 8 ms the arc appears unstable and a transition occurs from the first pilot arc phase to the second one (described at the beginning of the paragraph), with the emission of grey–blue hafnium vapours. The transition event ends at t = 8.3 ms and the arc root is stabilized at the center of the emitter surface. This sequence is in line with that reported in [14] for a pure Hf emitter with no initial recess.

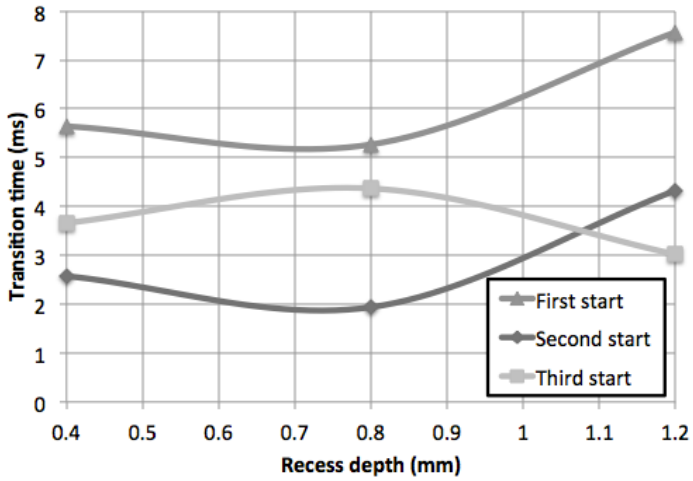

Figure 29 Time required for pilot arc root stabilization at the center of the Hf emitter surface as a function of the recess depth for new electrodes. [16]

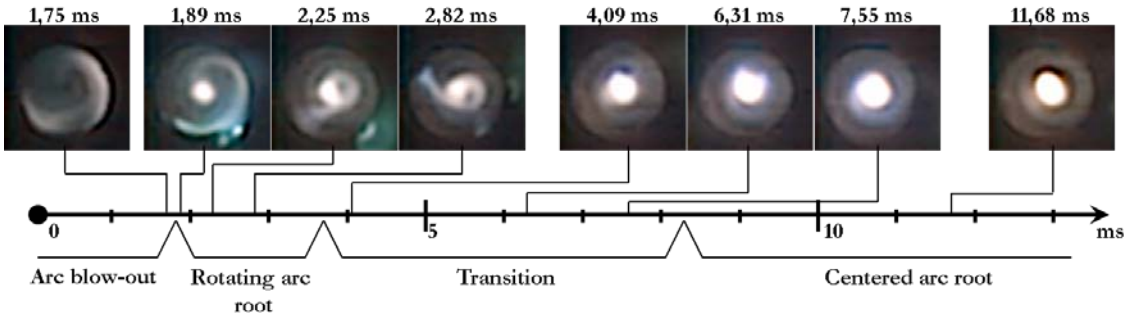

Figure 30 Pilot arc images, at different time intervals, for the case of a new electrode with a flat emission surface with initial recess of 1.2 mm. Images acquired at 100 000 fps and 1/200 000 s shutter time without any filtering. [16]

3.2 Pilot arc attachment on nozzle surface during start-up transient in a realistic time scale

During pilot arc start-up transient, the arc is ignited between the electrode and the nozzle internal surface and it is successively blown out by the plasma gas leading to the root attachment on the external surface of the nozzle. During this transient, the arc root may induce a local oxidation of the nozzle surface with a characteristic spiral pattern due to swirl component of gas velocity in the plasma chamber. The residence time of the pilot arc root on the internal surface influences directly the wear amount of the surface. While high-speed imaging for pilot arc has been reported for long transients (hundreds of milliseconds) that are not encountered in standard torch operation procedures [13], here high-speed imaging of the pilot arc during start-up transient is reported in a realistic time scale (few milliseconds) in order to evaluate the time required for the pilot arc anodic root to reach the external surface of the nozzle. Tests have been performed for two different geometries of the plasma gas diffuser: diffuser with 6 holes with diameter 0.8 mm (diffuser 1), and diffuser with 3 holes with diameter 0.4 mm (diffuser 2). In the high-speed imaging frames reported, the t = 0 ms is fixed for pilot arc ignition. In the case with diffuser 1 (see figure 31), the pilot arc is rapidly blow out of the nozzle in about 0.35 ms and the arc root stabilizes on the external surface of the nozzle; in the case with diffuser 2 (see figure 32), the residence time of the arc root inside the plasma chamber is more than 3 ms. Diffuser 1 has a lower swirl component and higher flow rate with respect to diffuser 2 as a consequence of the higher flow cross

section area. The higher swirl component of the plasma gas obtained with diffuser 2 can be beneficial for arc stabilization during steady state cutting conditions and thus improvement of the cut quality, but during pilot arc phase a higher residence time of the pilot arc root inside the plasma chamber may results in a higher erosion rate of the nozzle.

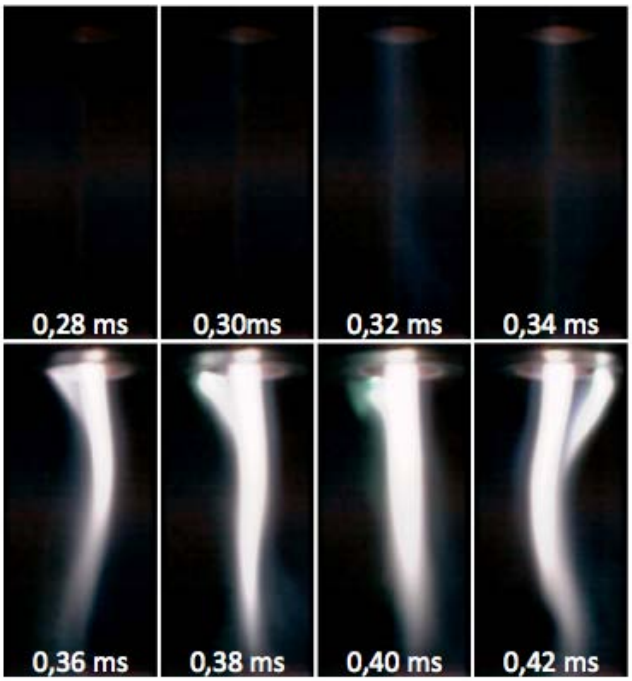

Figure 31. Selected high-speed imaging frames of the pilot arc start-up transient for the case with low swirl component of the gas velocity (diffuser with 6 holes, diameter 0.8 mm). Images acquired at 50 000 fps and 1/200 000 s shutter time without any filtering. [16]

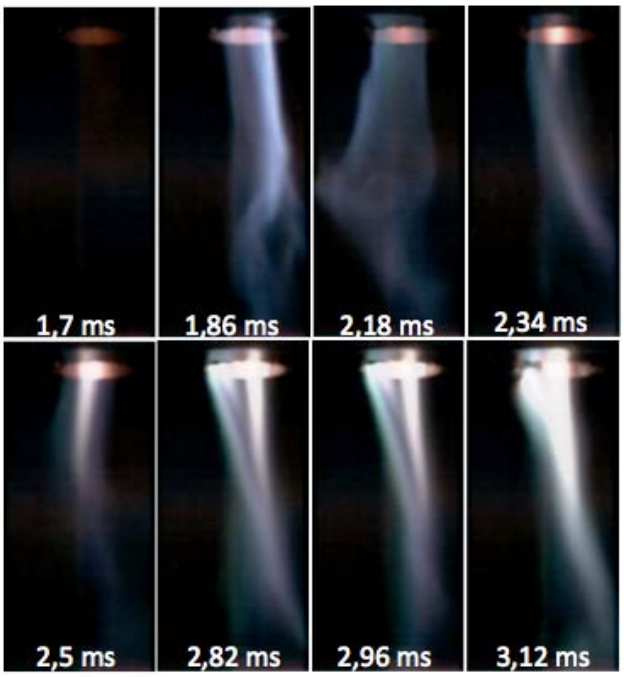

Figure 32. Selected high-speed imaging frames of the pilot arc start-up transient for the case with high swirl component of the gas velocity (diffuser with 3 holes, diameter 0.4 mm). Images acquired at 50 000 fps and 1/200 000 s shutter time without any filtering. [16]

3.3 Behaviour of the arc inside the plasma chamber during torch operation in transferred mode

High-speed imaging of the arc inside the plasma chamber during torch operation in transferred mode has been accomplished by removing the shield cup and by using a modified nozzle, as shown in [13], characterized by the presence of a viewing port at one side of the nozzle, positioned at an angle of 45° from the torch/arc axis.
The transferred mode was obtained using a water-cooled rotating carbon cylinder simulating the anode and replacing the workpiece; a quartz window has been suitably positioned into the port and locked through a specific sealing resin. The viewing angle of 45° implies the presence of the round view port in images and an elliptical shape of the hafnium insert.
Operating conditions during the recordings in the transferred mode were those typical of cutting 20 mm thick MS plates at 250 A, whose current profile is reported in figure 33: the pilot arc with a current of 25 A is ignited at t = 0 ms and the arc is transferred to the workpiece in few milliseconds; the current level is successively increased up to the nominal current of 250 A in about 150 ms; during this transient the plasma gas pressure is increased and the plasma gas composition is changed from dry air to pure oxygen. The nominal current is maintained for 1 second and, finally the arc is extinguished after a current ramp-down transient of about 100 ms.
During current ramp-up (selected frames reported in figure 34), Hf vapour ejected from the emissive element can be seen with the characteristic blue-gray colour together with solid particles dragged by the plasma gas.
At the end of the operation, during current ramp-down molten particles dragged by the plasma flow can be seen as for the cases reported for the pilot arc shut-down. In the selected frames reported in figure 35, t = 0 ms corresponds to the instant in which the arc is extinguished; the emission of molten particles from the cathode surface is mainly concentrated after the arc is extinguished, when the arc pressure is no more contrasting the dragging of the cathode molten pool by the plasma gas that leads to Hf droplet ejection.
During torch operation and in particular during arc start-up transient, the arc may exhibit an unstable behaviour. In figure 36, the waveform of the cathode-nozzle voltage drop during the start-up transient is reported together with the frequency spectrum analysis of selected time regions using the Fast-Fourier-Transform algorithm. During current ramp-up, the cathode-nozzle voltage is smooth and no remarkable spikes can be seen in the whole transient. However, high-speed imaging revealed a pulsing behaviour of the arc after 80 ms in which the arc luminous diameter has an oscillation between about 1 mm and 1.5 mm with a frequency of about 8 kHz (selected frames reported in figure 37), whereas the arc is stable before that point. Frequency analysis of the cathode-nozzle voltage in these two time regions showed a different spectrum: the time region with pulsing arc behaviour is characterized by peak at a frequency of 7.7 kHz, which is very close to the observed oscillation with high-speed imaging, whereas the time region with stable arc has no peak frequencies. The pulsing behaviour of the arc could be originated by fluid-dynamic instabilities such as Kelvin-Helmholtz ones, which are due to the hot plasma flow interacting with the cold plasma gas, or by Helmholtz pressure resonance, as was suggested in [18] for DC non-transferred arc plasma torches. Data acquired in our tests are not sufficient to conclude which physical mechanisms are responsible for the reported pulsing arc behaviour. Future investigations with the help of numerical simulations and gas pressure probing inside the plasma chamber will be helpful to clarify this point.

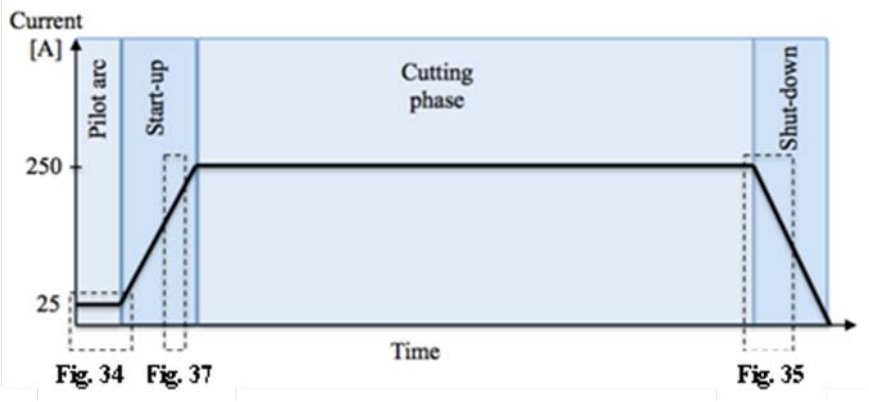

Figure 33. Schematic of current profile during the experiment of section 3.3 with superimposed time interval for high speed imaging acquisitions reported in figures 8, 9 and 11. [16]

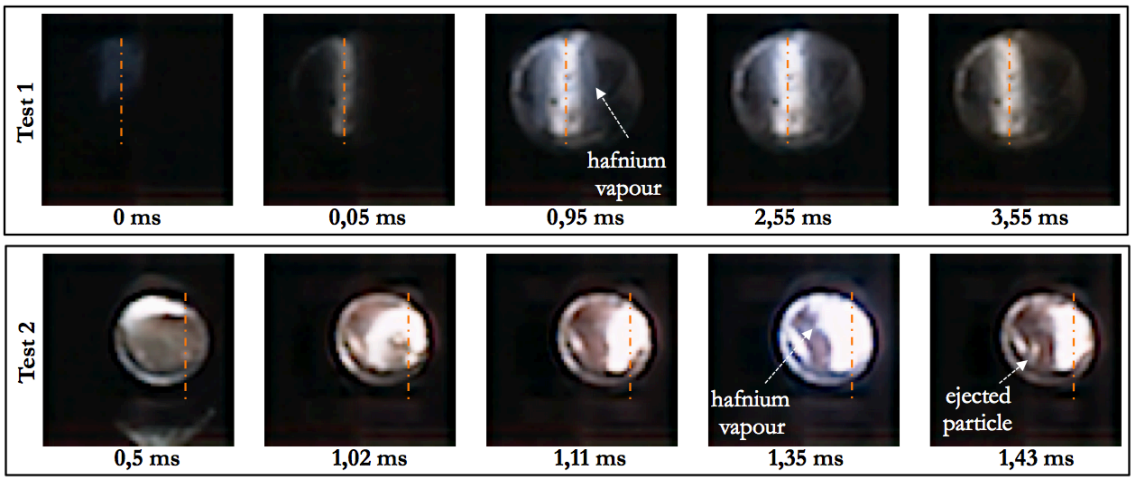

Figure 34. Selected high-speed imaging frames during arc start-up transient from two different tests of torch operation in transferred arc mode. Frame t = 0 ms corresponds to pilot arc ignition. Torch axis depicted using dotted orange line. Images acquired at 80 000 fps and 1/333 000 s shutter time with no filtering. [16]

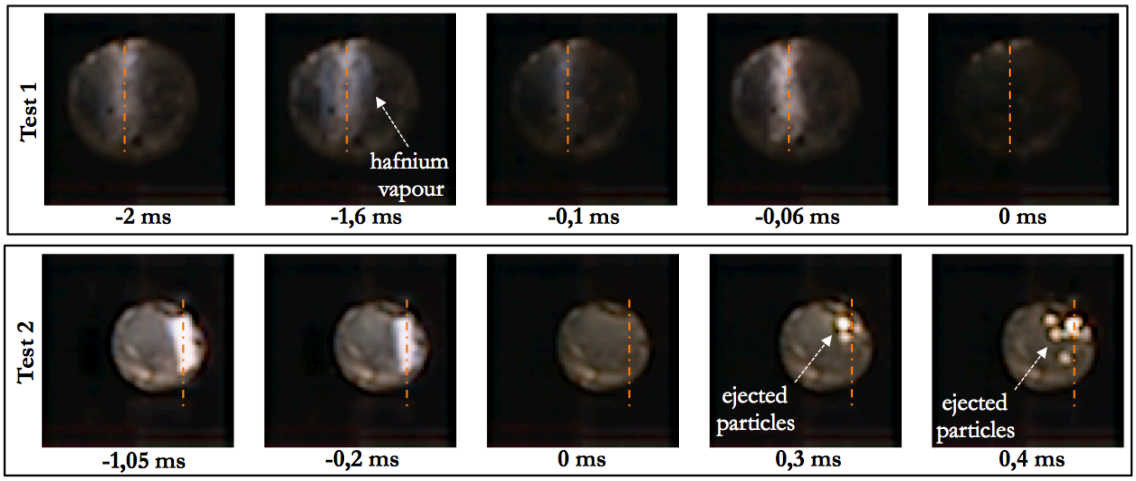

Figure 35. Selected high-speed imaging frames during arc shut-down transient from two different tests of torch operation in transferred arc mode. Frame t = 0 ms corresponds to the instant in which the arc is extinguished after current ramp-down. Torch axis depicted using dotted orange line. Images acquired at 80 000 fps and 1/333 000 s shutter time with no filtering. [16]

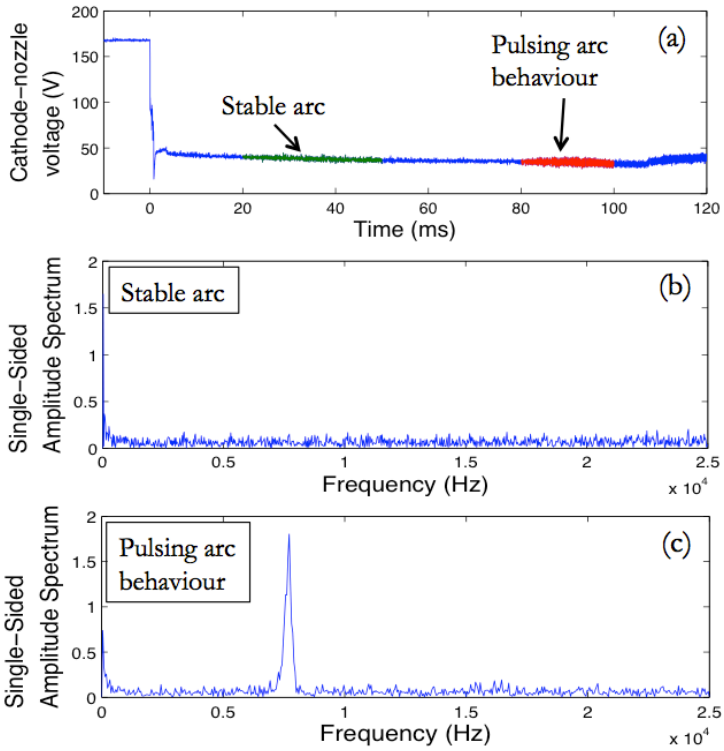

Figure 36. Cathode-nozzle voltage waveform (a) during transferred arc mode and Fast-Fourier-Transform analysis of the time region with stable arc (b) and with pulsing arc behaviour (c). [16]

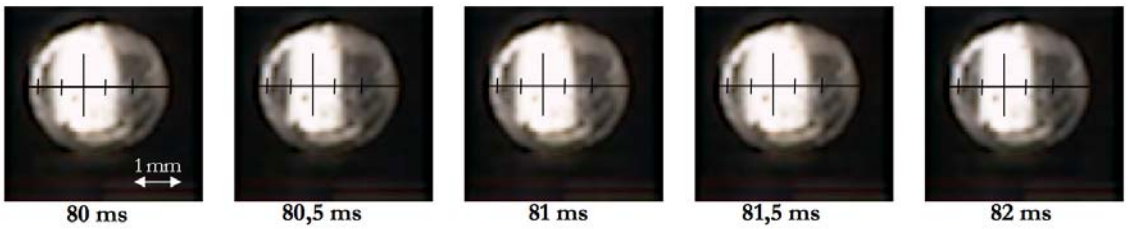

Figure 37. Selected high-speed imaging frames during torch operation in transferred arc mode in the time region with pulsing arc behaviour. Reference axes depicted using black lines. Images acquired at 80 000 fps and 1/333 000 s shutter time with no filtering. [16]

3.4 Erosion during pilot arc shut-down transient in cathodes with modified emissive elements

It has been shown in previous studies [1, 14] that droplets of molten cathode material can be expelled from the emissive surface during pilot-arc shut down and, in general, during arc-off transient contributing to the cyclic erosion of the electrode. One hypothesis on the cause of the shut-down erosion was suggested in [1]: the reduction in gas pressure during arc shut down leads to gas liberation from the molten puddle in the form of bubbles that drag the molten material out of the emissive surface. Another hypothesis related this ejection to the imbalance of different forces (e.g. fluid drag, centrifugal force) acting on the molten pool during this transitory [6].
In this section high-speed imaging results are reported for the pilot arc shut-down phase in a Cebora CP251G torch with electrodes characterized by different types of emissive elements. First of all, a worn electrode, which already underwent several cutting cycles

and thus characterized by a Hf oxide layer on top of the emissive surface, is investigated as a reference case. Since different technological solutions have been proposed in the last decade to reduce cyclic erosion based on the use of artificially shaped emissive elements [14] and on emissive elements made by mixtures of hafnium and a more conducting material like silver or copper [17], the pilot arc shut-down has been recorded also for a new electrode with pure Hf flat insert surface, a new electrode with pure Hf insert showing a spherical concave recess of 0.35 mm of depth, and two new electrodes with emissive elements made by binary alloys of Ag-Hf and Cu-Zr. In the cases reported, the arc shut-down is set at t = 0 ms and the current reaches a null value after few microseconds as a consequence of natural decay.

In figure 38-a selected frames for the case with used Hf electrode have been reported: the shut-down phase is characterized by a strong ejection of molten particles from the emissive surface that are dragged towards the nozzle outlet.

For the cases with new electrodes made with pure Hf (figure 38-b and 38-c), molten particles are ejected during the shut-down phase; although it is known to influence the erosion rate, especially during first cycles [2], the shape of the initial recess (flat or concave) seems to have no influence on the erosion during pilot arc shut-down phase.

In the cases with electrodes with emissive elements made with binary Ag-Hf and Cu-Zr mixtures (figures 39-b and 39-c), the shut-down phase is much shorter than for the pure Hf emissive insert (figure (39-a) and no emission of molten droplets can be observed during the whole transient. The time required for the melted insert to solidify is more than 6 ms for the pure Hf insert, 0.6 ms for the Ag-Hf insert and about 3 ms for the Cu-Zr insert. This behaviour could be related to the solidification kinetics of the standard and composite inserts. In particular, solidification occurs more rapidly when the improved inserts comprising a high conductivity phase are used. As discussed in [6], during the shut-down phase, it is an imbalance of forces acting on the molten pool transitory which causes particles to be ejected. It is therefore clear that if fast solidification is achieved, as for the composite inserts, this massive ejection can be limited. The alloys of Ag-Hf and Cu-Zr are characterized by a lower boiling point compared to pure Hf and with these materials an increase in evaporative losses during the cutting phase can be expected. However, metal vapours emitted by emitter surface are easily ionized by the plasma discharge and ions drift towards the cathode, induced by the electric field, reduces the evaporative losses [1, 19]. Also, the temperature of the insert during cutting can be reduced by the higher cooling of the alloys compared to pure Hf. Further investigations are required to fully understand the effect of these alloys on steady operation.

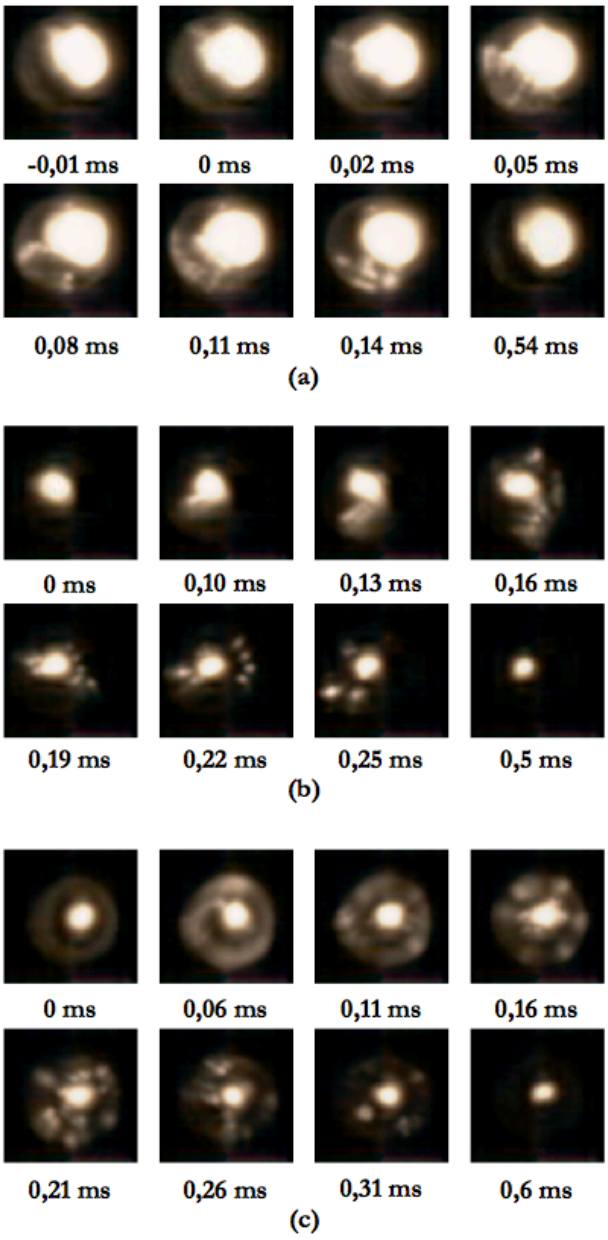

Figure 38 Selected frames of high-speed imaging of the pilot arc for the case of used electrode (a), new electrodes with flat (b) and concave (c) initial recess during the shut-down phase. Images acquired at 100 000 fps and 1/200 000 s shutter time without any filtering. [16]

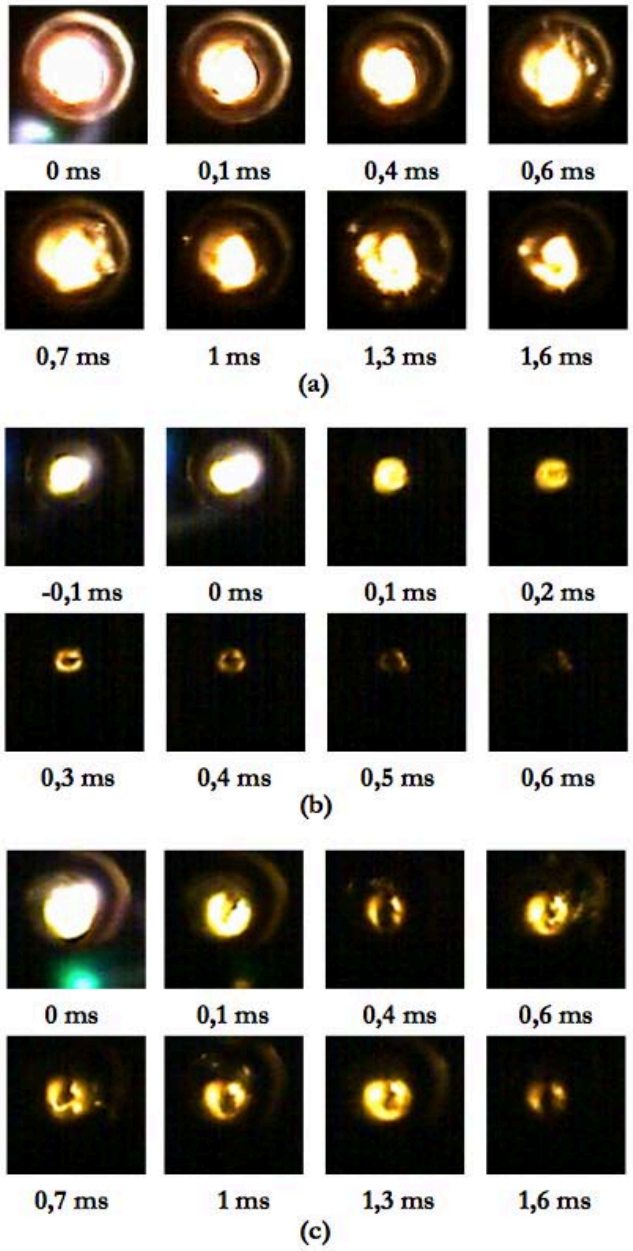

Figure 39 Selected frames of high-speed imaging of the pilot arc for the case of new electrodes with emissive material made with Hf (a), with Ag-Hf binary alloy (b), and with Cu-Zr binary alloy (c) during the shut-down phase. Images acquired at 10 000 fps and 1/200 000 s shutter time without any filtering. [16]

3.5 Process design oriented diagnostics of arc instabilities during the cut initiation phase

During design phase of plasma torch consumables, non-optimized consumable geometry and operating conditions may induce a low cut quality and a rapid wear of torch consumables. Diagnostics by high-speed imaging of the arc can provide useful insights on arc behaviour inducing poor cut quality or short consumable life time, thus supporting the design of improved torch geometries and operating conditions. In this section, the design phase of a mono-gas plasma torch (Cebora CP101) operating in air is reported. Standard 20 mm MS cutting at 160 A was initially characterized by a poor cut quality. High speed imaging of arc initiation phase in edge start revealed a strong

fluctuation of the arc near the torch nozzle outlet (figure 40-a) associated with a fluctuation of the total arc voltage with many spikes (figure 40-b). The arc fluctuation results in emission of copper vapours from the torch nozzle probably due to non-destructive transient double arcing phenomena (figure 41). Arc fluctuations were related in this case not to anodic root random movement but rather to cathode attachment instabilities. Since a too high swirl component in the plasma gas velocity at injection point and in the near cathode region could be the reason behind cathode attachment instability, a plasma gas diffuser with a reduced swirl component has been designed and tested (42 holes - 1.4 mm diameter instead of 8 holes - 1.2 mm diameter), keeping constant all the other cut parameters. Plasma gas flow rate is assumed to not change significantly by switching to the new diffuser: in the investigated configurations, plasma gas flow rate is mainly determined by the nozzle orifice because the nozzle flow cross sectional area is much small than that of the diffusers. Consequently, the change in diffuser geometry mainly influences the amount of swirl component in the plasma gas. With the new diffuser, cutting quality has been greatly improved in terms of dross absence and squareness of the *kerf*. High speed imaging of the arc initiation phase during edge cut showed a stable plasma plume associated with a smoother arc voltage waveform (figure 42). Qualitative insights from high speed imaging analysis led to identification of the possible source of poor cut quality and to the optimization of the torch geometry. Results reported in this section highlight the importance of high-speed imaging diagnostics for supporting the design phase of plasma arc cutting torches and for process optimization.

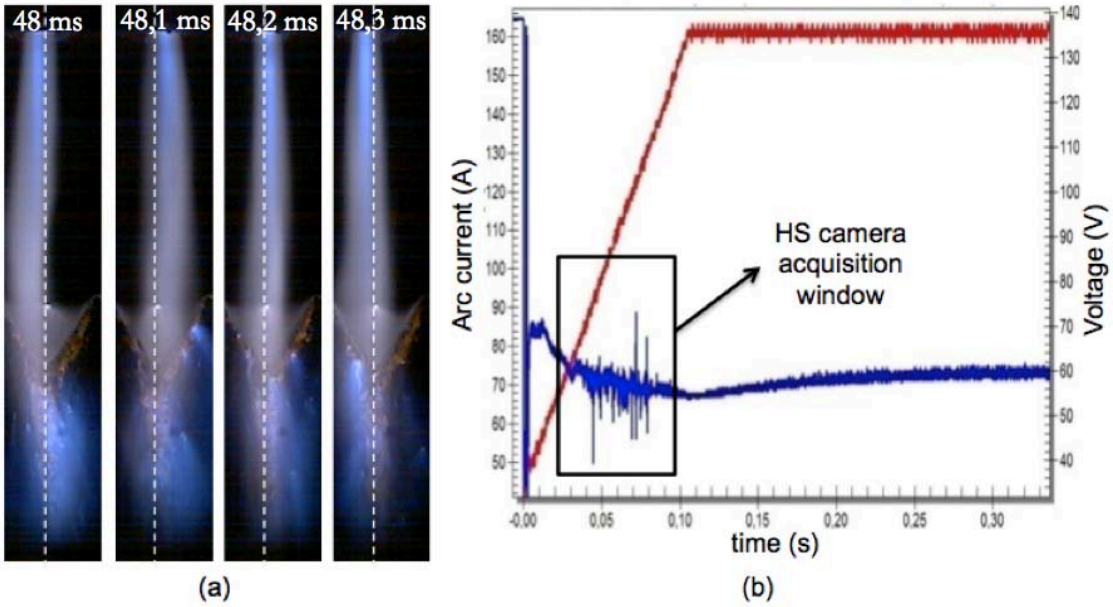

Figure 40. Selected frames of high speed imaging (a) and associated current and total arc voltage waveforms (b) during arc initiation phase in edge cut of a 20 mm thick MS plate. Case with strong swirl component (diffuser with 4 holes, 1.2 mm diameter). Torch axis depicted using dotted white line. Images acquired at 10 000 fps and 1/200 000 s shutter time with no filtering. [16]

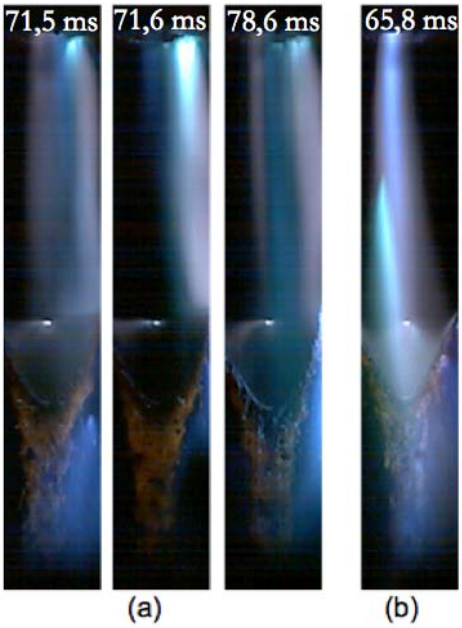

Figure 41. Selected frames of high speed imaging during arc initiation phase in edge cut of a 20 mm thick MS plate. Case with strong swirl component (diffuser with 4 holes, 1.2 mm diameter). Frames with transient double arcing phenomena (a) and copper emissions from torch nozzle outlet (b). Images acquired at 10 000 fps and 1/200 000 s shutter time with no filtering. [16]

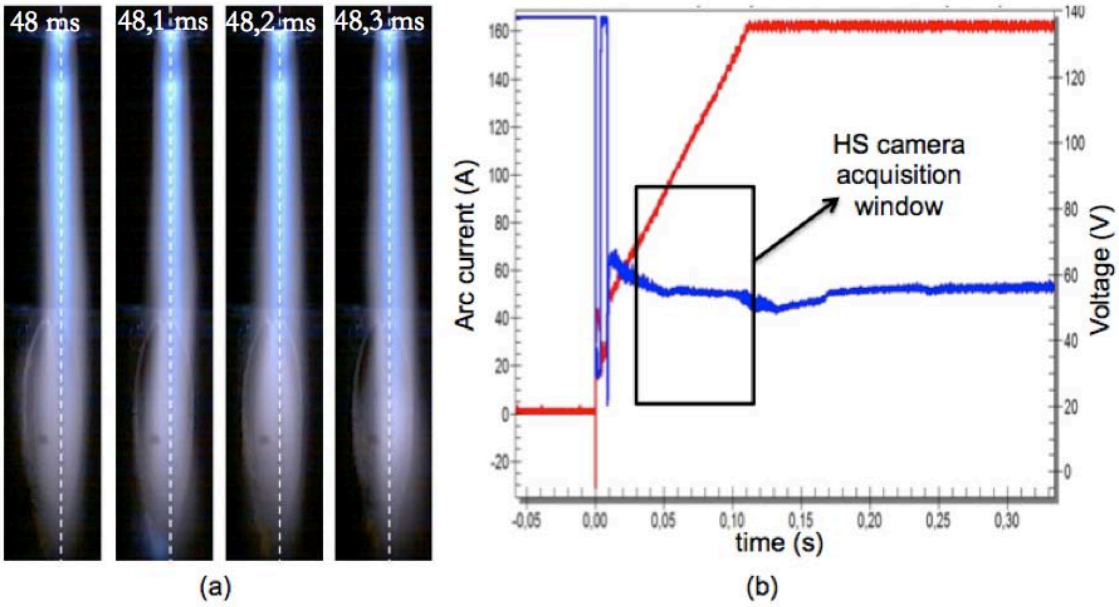

Figure 42. Selected frames of high speed imaging (a) and associated current and total arc voltage waveforms (b) during arc initiation phase in edge cut of a 20 mm thick MS plate. Case with low swirl component (diffuser with 42 holes, 1.4 mm diameter). Torch axis depicted using dotted white line. Images acquired at 10 000 fps and 1/200 000 s shutter time with no filtering. [16]

4. Conclusions

Selected results from high-speed imaging investigation of transient phenomena that impact torch consumable erosion rate and cut quality have been reported. In particular, it is shown that the depth of the initial recess of the emissive element in Hf electrodes does not have influence on the time required for the stabilization of the arc attachment on the center of the emitting surface during pilot arc start-up transient. These results confirm the idea reported in [14] that the transition time is mainly influenced by thermal properties of the emitting material. Moreover, results are reported for electrodes with emissive insert composed of binary alloy of emitting materials (Hf or Zr) and a conductive material (Ag or Cu): it is shown that binary alloy electrodes have a pilot arc shut-down transient characterized by a faster solidification of the molten insert without massive emission of droplets from the liquid insert surface. Also, high speed imaging of torch operation in transferred arc torch revealed pulsing arc behaviour inside the plasma chamber that is correlated with cathode-nozzle voltage oscillations at a frequency of 7.7 kHz. Moreover, results are reported for residence time of pilot arc root attachment on the internal nozzle surface during start-up transient with different plasma gas diffusers. Finally, results are reported for the influence of the swirl component of the plasma gas on the cut quality, which is influenced by cathode instabilities induced by a too high swirl flow.

References

[1] Nemchinsky V A and Severance W S, Journal of Physics D: Applied Physics **39** R423-R38 (2006)

[2] Colombo V, Concetti A, Ghedini E, Rotundo F and Dallavalle S, Plasma Sources Science and Technology **19** 012008 (2010)

[3] Rotundo F, Martini C, Chiavari C, Ceschini L, Concetti A, Ghedini E, Colombo V and Dallavalle S, Materials Chemistry and Physics **134** 858-66 (2012)

[4] Colombo V, Concetti A, Ghedini E, Rotundo F, Sanibondi P, Boselli M, Dallavalle S, Gherardi M, Nemchinsky V and Vancini M, Plasma Chemistry and Plasma Processing **32** 411-26 (2012)

[5] Cantoro G, Colombo V, Concetti A, Ghedini E, Sanibondi P, Zinzani F, Rotundo F, Dallavalle S and Vancini M, Journal of Physics: Conference Series **275** 065023 (2011)

[6] Peters J, Yin F, Borges C F M, Heberlein J and Hackett C, J. Phys. D: Appl. Phys. **38** 1781 (2005)

[7] Nemchinsky V, IEEE Transactions on Plasma Science **30** 2113-6 (2002)

[8] Nemchinsky V, Journal of Physics D: Applied Physics **36** 1573-6 (2003)

[9] Nemchinsky V A and Showalter M S 2003 Cathode erosion in high-current high-pressure arc Journal of Physics D: Applied Physics **36** 704-12

[10] Yamaguchi Y, Yoshida K, Uesugi Y, Tanaka Y, Morimoto S, Minonishi M and Saio K 2010 Experimental study of erosion of hafnium electrodes for oxygen plasma arc cutting Yosetsu Gakkai Ronbunshu/Quarterly Journal of the Japan Welding Society **28** 311-8

[11] Long N P, Tanaka Y and Uesugi Y, IEEE Transactions on Plasma Science **40** 497-504 (2012)

[12] Nguyen Phi L, Yusuke K, Yasunori T, Yoshihiko U and Yoshihiro Y, Journal of Physics D: Applied Physics **45** 435203 (2012)

[13] Colombo V, Concetti A, Ghedini E, Dallavalle S and Vancini M Plasma Sources Science and Technology **18** 023001 (2009)

[14] Colombo V, Concetti A, Ghedini E and Nemchinsky V, Plasma Sources Science and Technology **19** 065025 (2010)
[15] Kavka T, Hrabovsky H, Chumak O, Kopecky V, Maslani A, Konrad M, Pauser H, Heinrich M and Nimmervoll R, Proceedings of 19th Int. Symp. on Plasma Chemistry - ISPC19 Bochum (Germany) (2009)
[16] Boselli M, Colombo V, Ghedini E, Gherardi M, Rotundo F, Sanibondi P, J. Phys. D: Appl. Phys. **46** 224010 (2013) © 2013 IOP Publishing
[17] Coudert J F, Rat V and Rigot D, Journal of Physics D: Applied Physics **40** 7357 (2007)
[18] Luo Z and Couch Jr R W, Electrode for a plasma torch having an improved insert configuration, Hypertherm Inc. Patent US 6,130,399. (2000)
[19] Nemchinsky V, Journal of Physics D: Applied Physics **45** 135201 (2012)

CHAPTER 4
Inductively coupled plasma torch: Schlieren high-speed imaging and quenching device characterization

1. Introduction

In the field of thermal plasmas, inductively coupled plasma (ICP) torches have been widely used both at laboratory and industrial scale as high-temperature sources in a wide range of applications and in different disciplines, thanks to their unique characteristics: high energy density, high volume, high purity and high scalability. Since the first introduction of these thermal plasma sources in science and technology in 1961 [1], the range of possible applications has been steadily growing, to include analytical chemistry for elemental analysis, the chemical synthesis and deposition of high purity materials, spheroidization and purification of metallic and ceramic powders, the synthesis of nano-powders, the destruction of waste materials, as well as in aerospace research and re-entry problem simulation [2-4]. For what concerns its scalability, we can find industrial products and processes based on ICP technology spanning from a power of a few mW in the field of surface modifications of materials for the electronic industry [5] to the MW range for aerospace research [6] and waste treatment [7], passing through the well-established products for ICP-OES and ICP-MS detection of trace elements, that have a low power ICP torch as the heart of the process [8-9].

Recently, a low power ICP torch operated with argon/air mixtures, has been integrated with a quenching device to obtain an effective production of biologically active agents, while keeping effluent temperature and UV radiation at values compatible with biomedical [10]. To support the design of the device, ignition transients, discharge behaviour and flow fields downstream the ICP torch have been investigated using an high-speed imaging setup (HSI) and a Z-type optical setup for Schlieren imaging (SI). Additionally, in order to assert the potential of the device in biomedical treatments, reactive species and UV radiation production have been evaluated by using different diagnostic methods, such as optical emission spectroscopy (OES) and Fourier Transform InfraRed (FT-IR) spectroscopy, at several distances from the plasma device outlet. This research has been performed in close collaboration with Romolo Laurita and some of the results presented in the following pages have been published in [11] and submitted to [12].

2. Experimental setup

2.1. ICP torch and quenching device

The low power ICP torch presented in this work was integrated with a quenching device, shown in figure 43, for cooling down the gas stream and efficiently producing biological active agents relevant for biomedical applications [10]. The ICP torch consists of a three-turn air-cooled coil (for an axial length of 1,6 cm, starting 4,6 cm downstream the gases inlet and ending 0,6 cm upstream the torch exit section) surrounding the quartz confinement and the separator tubes, having inner diameters of

18 mm and 14 mm, respectively. The coil is connected through a matching network to a 1 kW, 13.56 MHz RF solid state power generator (Stolberg HF.Technick, Germany).

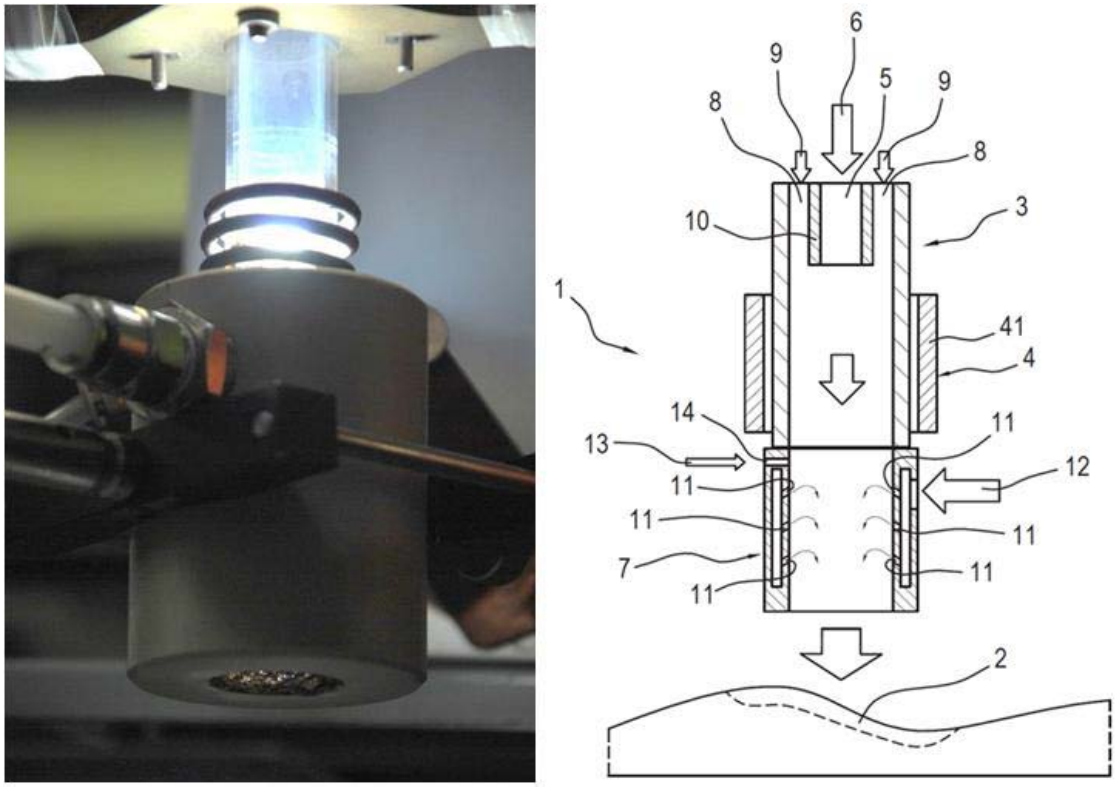

Figure 43. Low power ICP with a quenching device (left) and schematic of the source (right) [10]

The plasma source can be operated with Ar as central gas and a mixture of Ar and air as sheath gas, injected with a swirl component inside the torch, at the limit of sustainability for such a frequency at atmospheric pressure [13]. The quenching device placed at the torch outlet consists of a 7.5 cm long dielectric tube, with suitably designed air injection ports and an exit orifice of 25 mm of diameter for the gaseous effluent.

2.2. High-speed and Schlieren imaging setup

Plasma ignition was induced with the insertion of a tungsten rod in the induction region and by using a Tesla coil, leading in a time span of the order of a few hundreds of milliseconds to a stable discharge exiting the torch confinement tube with a high temperature luminous plume.
An high-speed camera (Memrecam GX-3- NAC Image Technology), operating at 5000 fps and with an open shutter, has been used to study the ignition transient from two different viewpoints, one from the side, pointing perpendicularly to the torch axis, and one from the bottom with the aid of a mirror (figure 44).

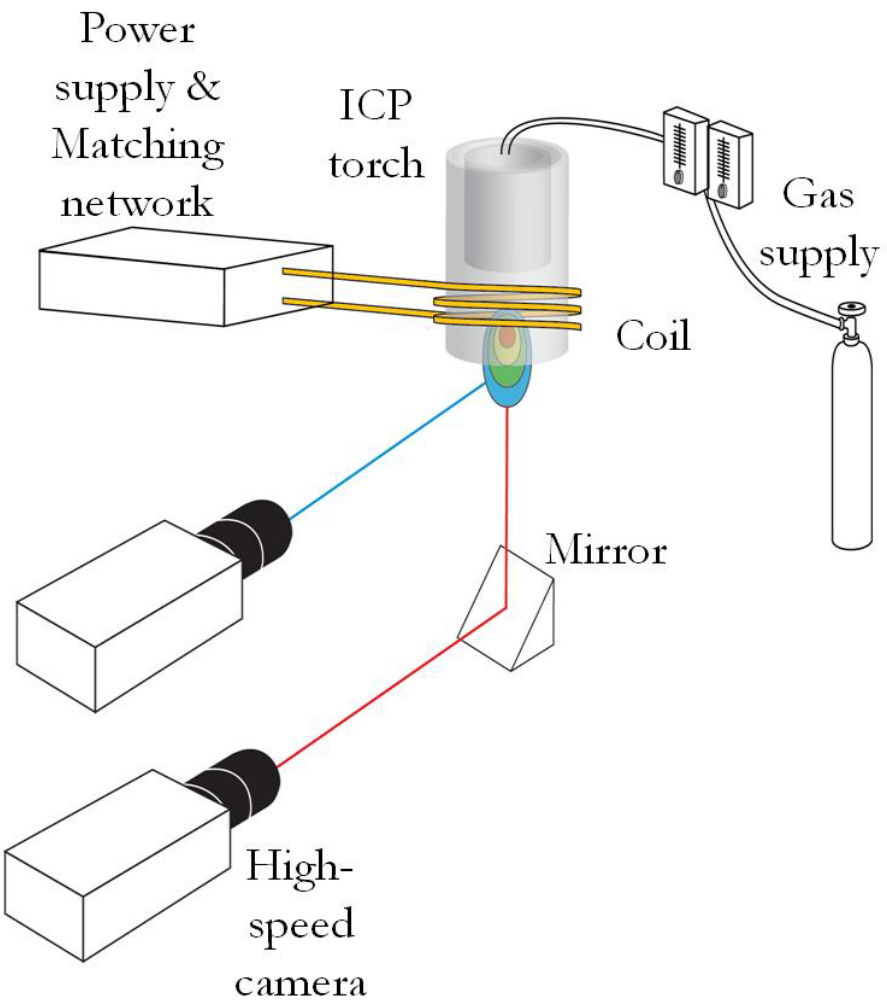

Figure 44. Experimental setup for side and bottom view high-speed imaging of the ICP torch without quenching device

Shape and behaviour of the plasma plume have also been investigated for different power and flow gas operating conditions with the high speed camera in the side view configuration, operating at 500 fps with an open shutter.

The transient and steady conditions of the plasma plume was also investigated through a Schlieren imaging setup in a Z configuration [14] (figure 45) composed of a 450 W Ozone Free Xenon Lamp (Newport-Oriel 66355 Simplicity Arc Source), a slit and an iris diaphragm, two parabolic mirrors with a focal length of 1 m, a knife edge positioned vertically or horizontally and a high-speed camera that records the Schlieren image.

The torch has been positioned in the middle of the optical path between the two parabolic mirrors. For this setup, the high-speed camera was operated at 2000 fps and 1/100000 s shutter time. A similar setup has been used with the addition of the quenching device positioned at the torch outlet to see the device effluent jet shape and behaviour.

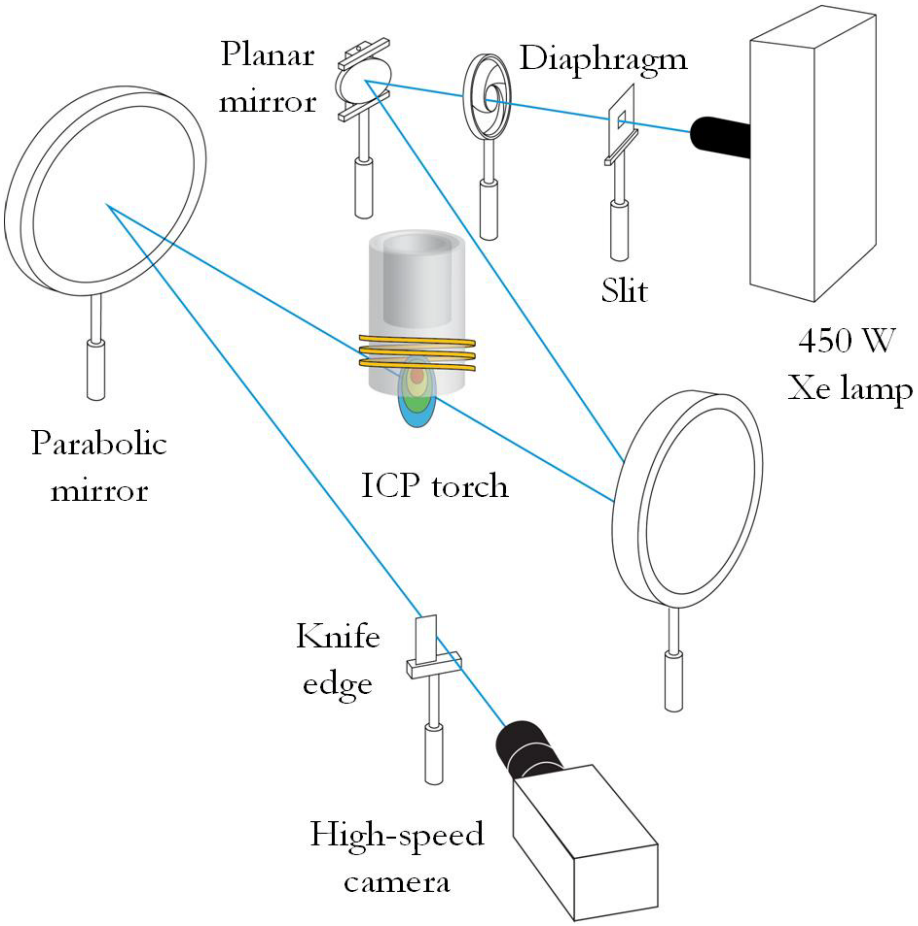

Figure 45. Experimental setup for high-speed Schlieren imaging of the ICP torch without quenching device

2.3. *Optical Emission Spectroscopy and UV irradiance measurement*

In order to identify the reactive species produced by the source, an iCCD camera (PIMAX3, Princeton Instruments) mounted on a 500 mm spectrometer (Acton SP2500i, Princeton Instruments) has been adopted to collect spatially resolved optical emission spectra in the ultraviolet (UV) region. A scheme of the experimental setup is reported in figure 46. Measurements have been performed with an optical fiber guide with a solid angle aperture of 20° pointing perpendicularly to the plasma source axis, with a 20 µm slit width and a spectral resolution of 0.17 nm. Exposure time has been set to 10 ms.
UV irradiance on a substrate placed below the ICP torch has been measured using the UV power meter Hamamatsu C9536/H9535-222 (measurement range of 0.001 mW/cm^2 – 200 mW/cm^2, high spectral response in the range 150-350 nm) with and without the quenching device. The sensitive part of the UV power meter was centered on the torch axis. Measurements have been carried out at different axial distances from the source outlet and each measurement was performed three times.

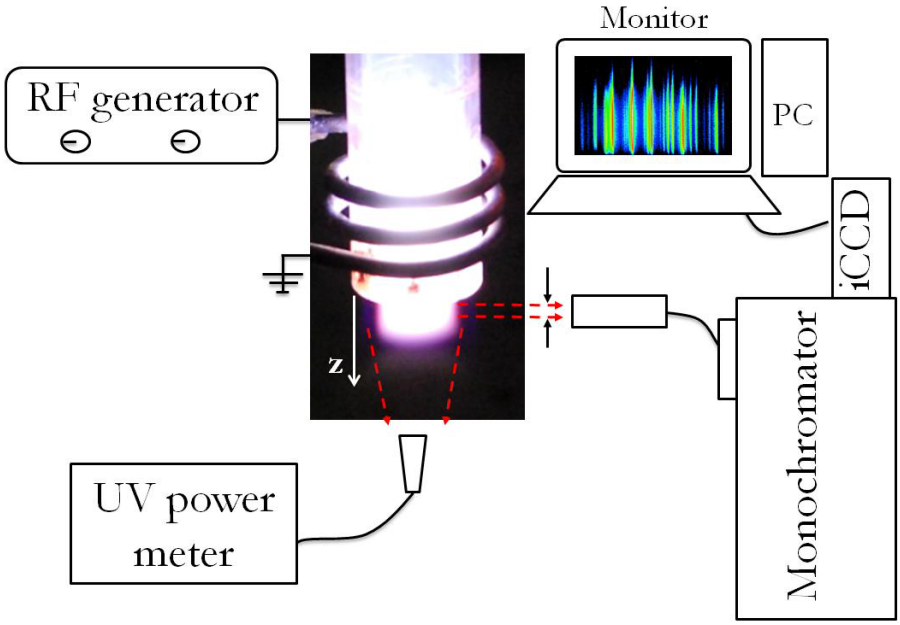

Figure 46. Experimental setup for OES and UV irradiance measurements

2.4. Nitric oxide emission measurement

In order to evaluate the NO and NO_2 concentration in the quenching device effluent in the treatment zone, an analysis through Fourier Transform InfraRed (FT-IR) spectroscopy of the gas composition was performed. Several measurements of the FTIR spectra were recorded in the spectral range of 4000 to 500 cm^{-1}, with resolution 2 cm^{-1} and 32 scans, by using a DLa TGS/KBr detector and a multiple-pass absorption cell with 16 meters of optical path folded in a volume of 2.3 liters. The cell was connected to the measurement zone through an aspiration tube, with a 1 m long heated zone at the inlet to allow a constant temperature of 40 °C inside the cell, followed by a 6 m long PTFE tube and terminating with a 10 cm long brass tube, both with an inner diameter of 4 mm. A membrane pump was used for flushing and sample-collecting operations.
The tip of the aspiration tube was placed directly below and pointed perpendicularly to the plasma source axis (figure 47). Each measurement was carried out by flushing the cell with the effluent of the plasma device for 120 s at a certain distance from the plasma device outlet for given plasma source conditions. After the acquisition of the FTIR spectrum, the plasma was shut down and a second acquisition was performed by flushing the cell for another 120 s with the same gas flow parameters of the previous acquisition. The latter spectrum was then subtracted to the former one in order to reduce the impact of ambient CO_2 and water vapor on the measurement and to better evaluate the contribution of the plasma source to NO and NO_2 concentration. In order to have a quantitative analysis for each spectrum, a calibration acquisition was performed at the beginning of each set of measurements with a gas tank with a known and certified concentration of 117.5 ppm of NO and 18.3 ppm of NO_2 in almost pure N_2. The calibration was performed with the same absorption cell pressure and the temperature conditions of the other measurements. Concentrations were calculated by comparing the relative intensity of each spectrum to the calibration source spectrum for two specific wavelengths, respectively 1903.4 cm^{-1} for NO and 1628.4 cm^{-1} for NO_2 [15]. The standard deviation was evaluated by performing each measurement at least thrice.

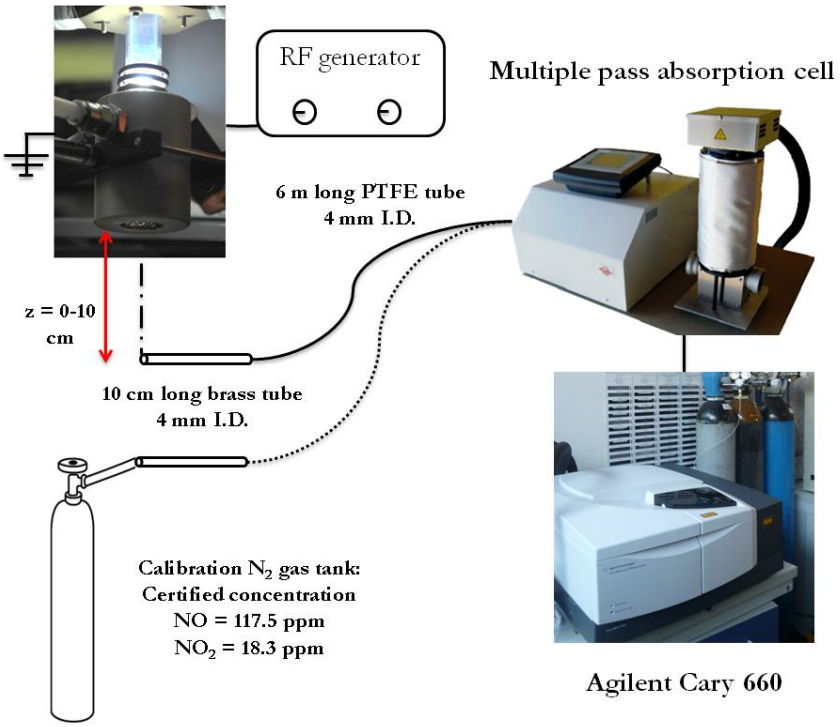

Figure 47. Experimental setup for NO and NO_2 concentration measurements

3. Results

3.1. HSI and SI of the ignition phase

Figure 48 shows selected side view HSI frames of a typical torch ignition transient driven by electron emission from a grounded tungsten rod immersed in the induction magnetic field. The capacitive mode (top frames) is ruled by a single streamer, possibly with multiple attachments on the rod (detailed in the leftmost frame), while in the coil region streamers in random pattern are located near the inner surface of the tube. During the inductive discharge (bottom frames), a diffuse plasma bubble is setting on, together with quartz vapour emission due to tube erosion.

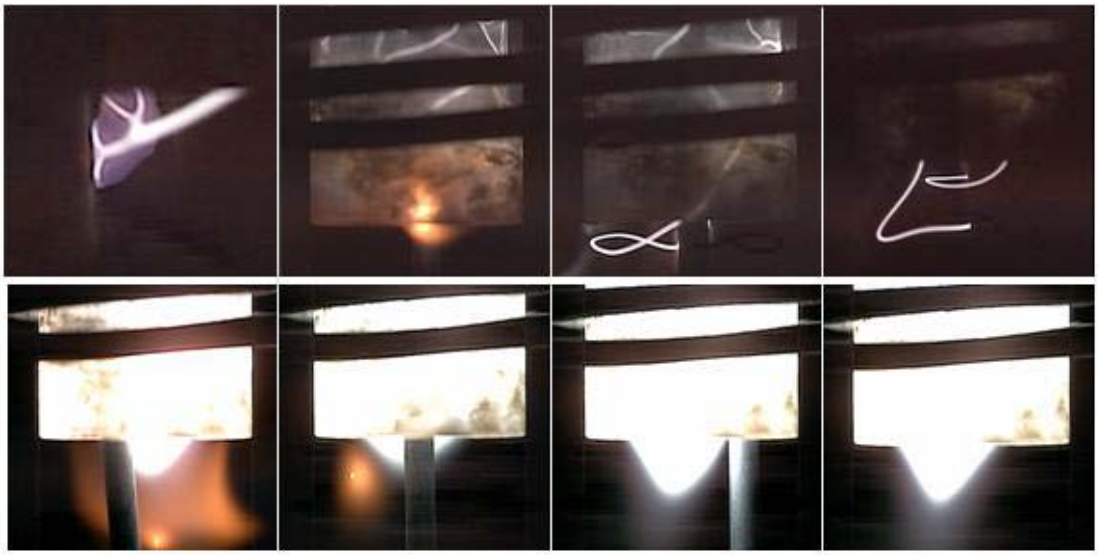

Figure 48. Side view HSI of the transition from capacitive mode (top frames) to inductive mode (bottom frames) [11] © 2014 IEEE

Axial view HSI of the ignition transient (figure 49) shows a rotating streamer connected to the rod and dragged by the swirling flow. On each frame is reported the relative time from the transition from capacitive to inductive mode. After transition to the inductive mode, the discharge expands from the peripheral skin depth region towards the axis. As shown in SI frames of figure 50, when the transition to inductive mode occurs, there is an increase in velocity and temperature of the gas blown out from the torch, even if the mass flow rate of Ar is kept constant (close to 4 slpm).

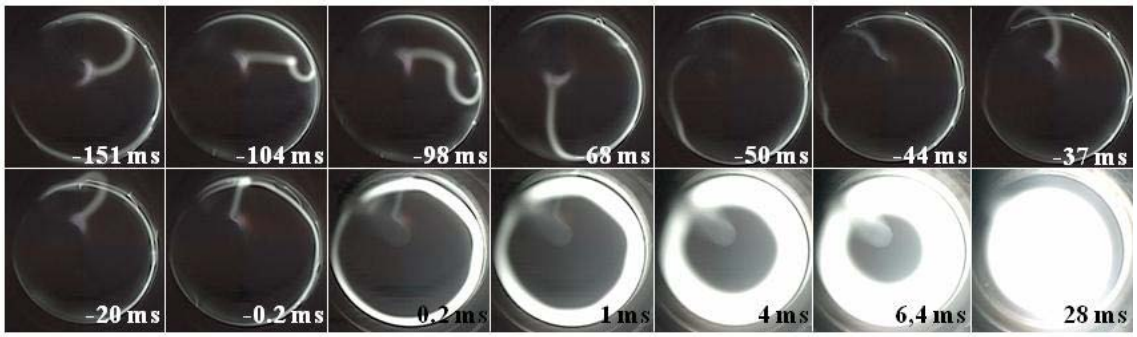

Figure 49. Axial view HSI of the discharge section over a time span of 180 ms. Frame t = 0.2 ms corresponds to plasma ignition. [11] © 2014 IEEE

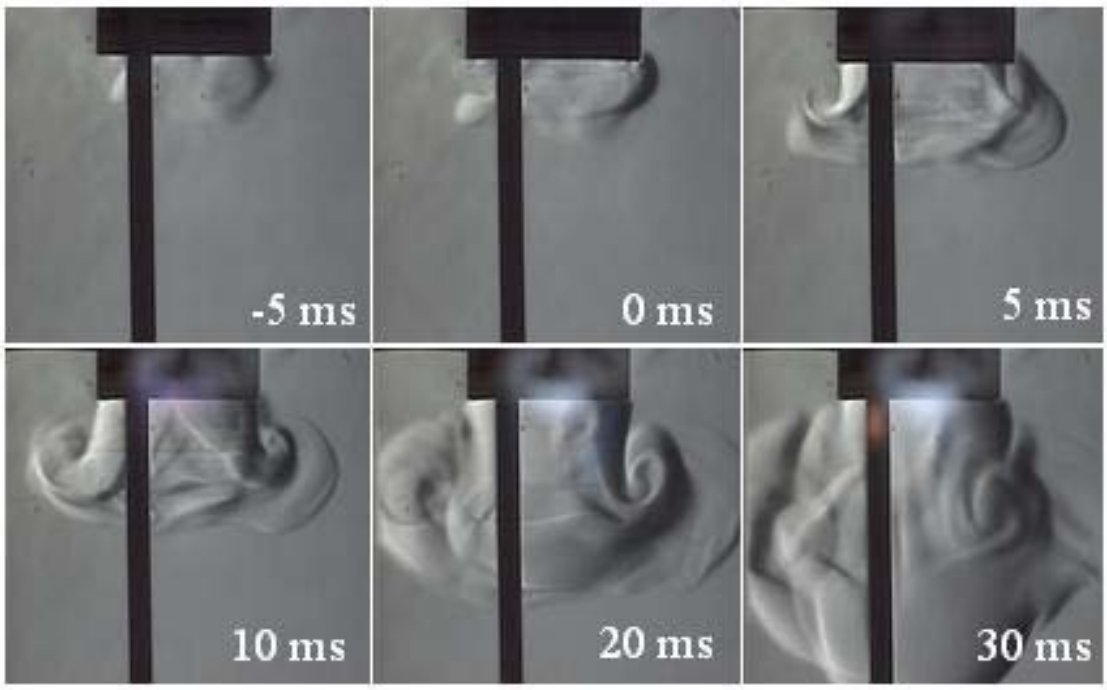

Figure 50. Side view SI of the downstream region of the discharge over the time span of 50 ms. Frame t = 0 ms corresponds to plasma ignition. [11] © 2014 IEEE

3.2. HSI and SI of the steady phase

In figure 51 and in figure 52, side view HSI (top) and SI (bottom) of the downstream region of the torch are shown for steady conditions and different gas flow rate. A laminar plasma plume is found when sheath gas flow rate is lower than 10 slpm, whereas for higher values a bow-like plume is observed, due to ambient air suction directed towards the torch, as shown by SI frames. Increasing the plasma power from

350 to 500 W, there is an increase in the visible light and the bow like plume occurs for higher gas flow rates. By mixing a small amount of air in the sheath gas (0.2 slpm), there is a further increase in the light emission intensity but the visible plasma plume at the torch outlet gets shorter, as the plasma generation zone seems to retreat in a more upstream position, compared to a similar Ar flow condition, as shown on the right most frame of figure 52.

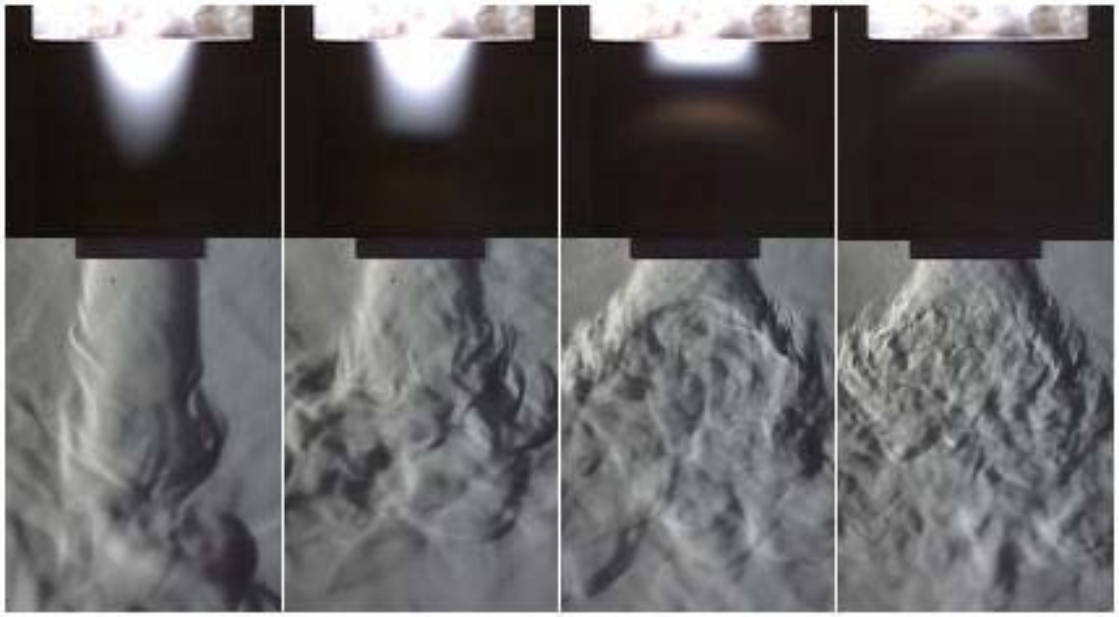

Figure 51. HSI (above) and SI (below) of ICP downstream region in steady conditions with Ar central gas flow rate 0.9 slpm and 350 W: from left to right: sheath gas: Ar, 8-10-12-14 slpm [11] © 2014 IEEE

Figure 52. HSI (above) and SI (below) of ICP downstream region in steady conditions with Ar central gas flow rate 0.9 slpm and 500 W: from left to right:sheath gas: Ar 10-16-18 slpm; Ar 14 slpm + air 0.2 slpm; [11] © 2014 IEEE

When operating the torch with the quenching device, the plasma jet in free-flow conditions shows a fully turbulent behavior with a slightly conical expansion (figure 53, left); when impinging on a Petri dish (figure 53, right; Petri dish is at 5 cm from the quenching device orifice) or more generally on a biological substrate, the flow is spread over its whole surface, promoting the dispersion of reactive species.

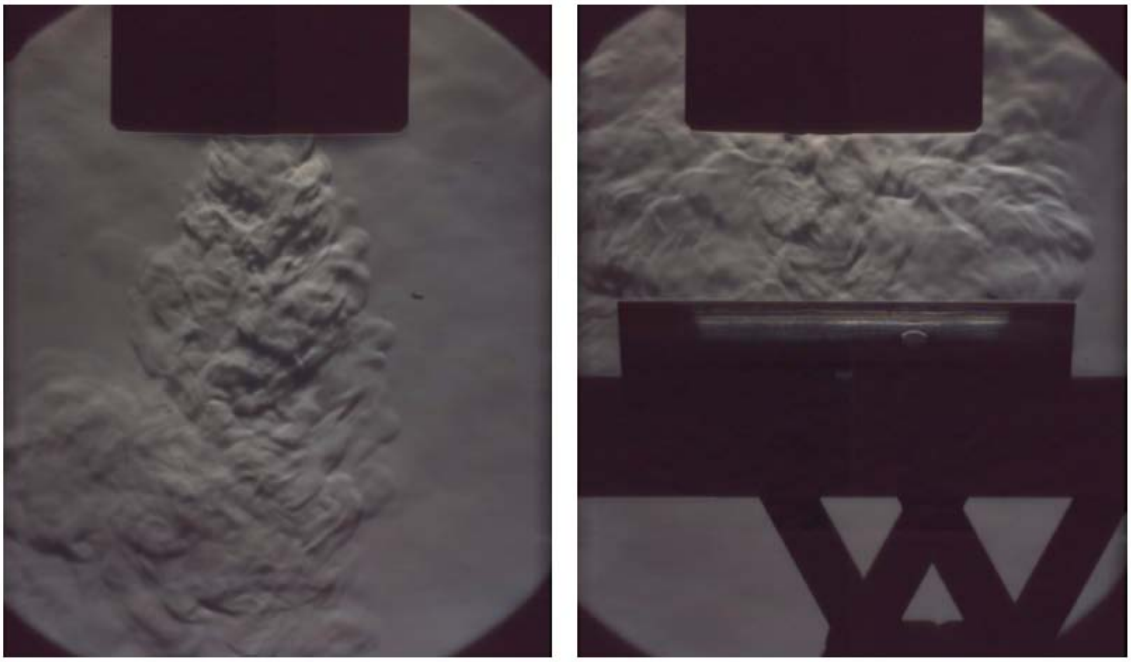

Figure 53. SI of the ICP torch with quenching device operating in free-flow conditions (left) and impinging on a Petri dish (right) [11] © 2014 IEEE

3.3. Optical Emission Spectroscopy and UV irradiance measurement

On figure 54 are reported optical emission spectra in the UV range without quenching device, collected from the side at different distances from the ICP outlet, with 600 W and 14 slpm Ar + 0.1 air of sheath gas flow rate. The dominant bands for excited NO, OH and N_2 species are also reported. The spectra show the presence of each species at least over 15 mm form the torch outlet. On the torch outlet the presence of OH is considerably low, probably due to the use of de-humidified air and Grade 5 argon. OH peaks get more intense by getting farther from the torch, probably due to the mixing and diffusion of water vapor from ambient air, with consequent OH formation. The increase in NO peaks could be due to the air suction to the plasma zone that can induce thermal formation of NO. N_2 peaks decrease in intensity at 15 mm from the torch outlet, probably due to a decrease in temperature in the plasma plume.

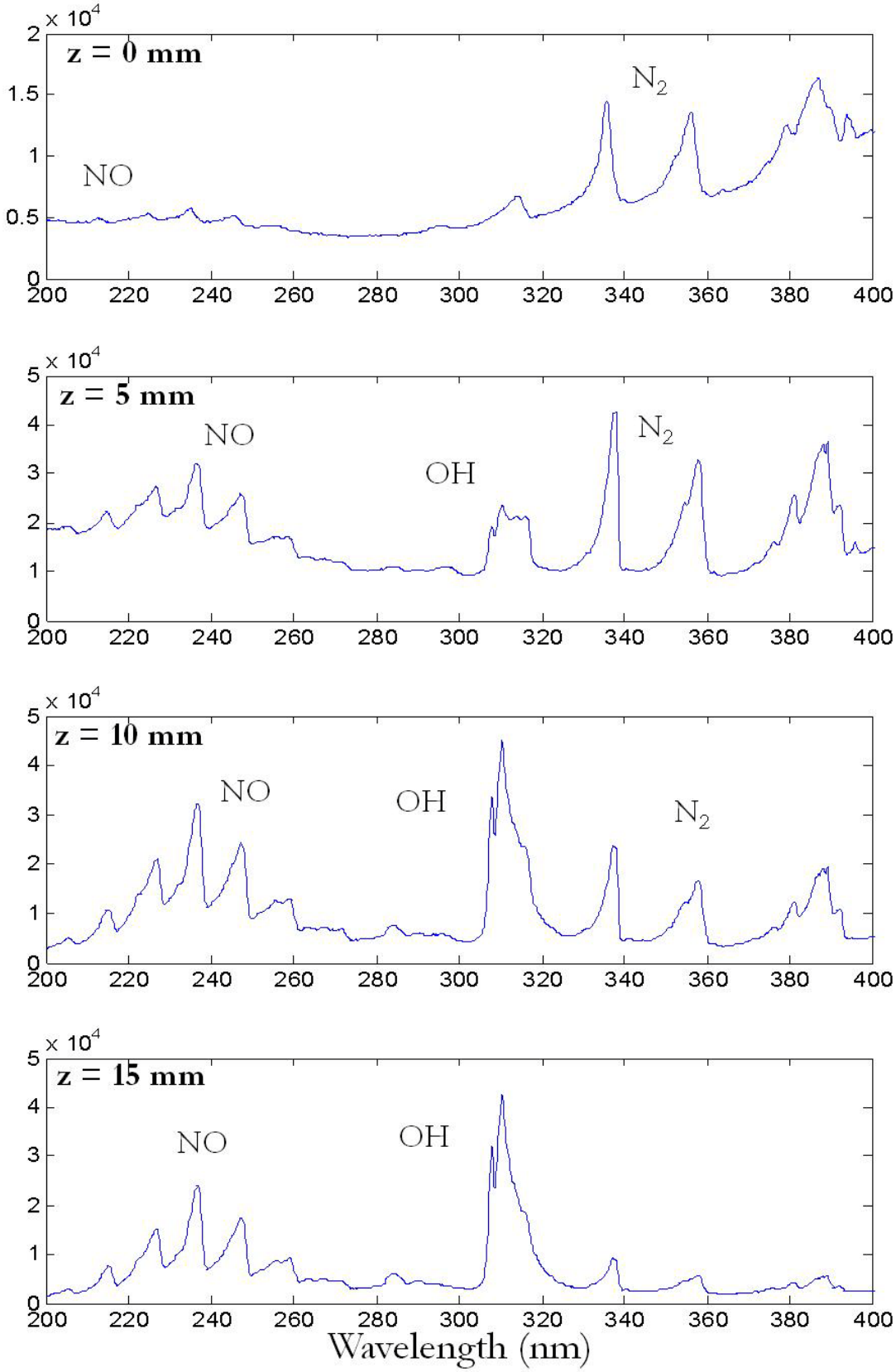

Figure.54 Side view optical emission spectra in the UV range without quenching device at different distances from the ICP outlet. Operating conditions are 600 W and 14 slpm Ar + 0.1 air of sheath gas flow rate

Axial profiles of the total UV irradiance produced by the low power ICP with and without quenching device in several operating conditions are reported in figures 55 and 56; in order to get deeper knowledge on the working map of the presented plasma source, measurements of the total UV irradiance were carried out also for some operating conditions different from those selected for biological experiments.
Results highlight that the UV irradiance monotonically decreases when the distance from the torch outlet is increased. As evaluable from the graph, the UV irradiance is strongly influenced by the air flow introduced in the sheath gas: the greater is the air content in the sheath gas, the higher is the measured UV irradiance. This effect can be related to the increase in UV emissions from NO, N_2 and OH excited species, more abundant in the plasma region when air is introduced in the plasma torch. Furthermore, the implementation of the quenching device induces a slight increase in UV irradiance, for all the considered cases, if compared with the corresponding cases without quenching device. This is probably due to the additional air flow introduced by the quenching device that leads to more N_2 and O_2 species interacting with the hot downstream plasma region.

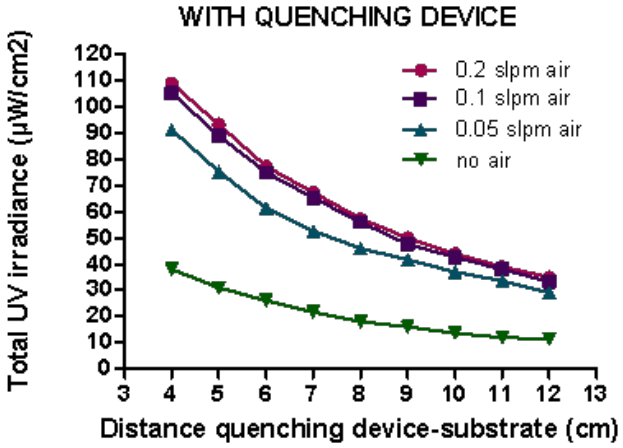

Figure.55 UV irradiance (150-350 nm) as a function of the axial distance between the orifice of the quenching device and the UV sensor for different operating. The flow rate of air in the sheath gas is reported for each condition.[12]

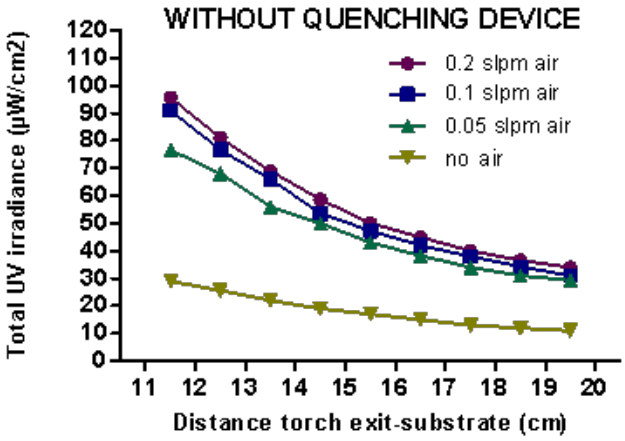

Figure.56 UV irradiance (150-350 nm) as a function of the axial distance between the torch outlet and the UV sensor (having in mind a parallel with results of figure 55, where the 7.5 cm long quenching device is present), for different operating conditions without quenching device. The flow rate of air in the sheath gas is reported for each condition.[12]

A similar analysis of the total UV radiation was carried out by different groups for other plasma sources usually adopted for biomedical applications [16-19], with the aim to select the operating conditions that result in UV irradiances compatible with *in vivo* treatments. The values measured for the cold ICP source in all the operating conditions tested are below the value (5 mW/cm^2) reported by Weltmann et al.[17]; moreover, for every distance higher than 5 cm and 6 cm, respectively for the 0.05 slpm and for the 0.1-0.2 slpm of air conditions, the measured values are found to be also below the ones collected by Morfill et al. for their plasma source (80μW/cm^2) [16]. Under these conditions, a therapeutic application of the presented plasma source without exceeding the ICNIRP exposure limit of 3mJ/cm^2 per day is regarded as feasible [18]

3.4. *Nitric oxide emission measurement*

Measured concentrations of NO and NO_2 for various axial distances and various flow rates of air in the cold ICP torch sheath gas are reported in figure 57.

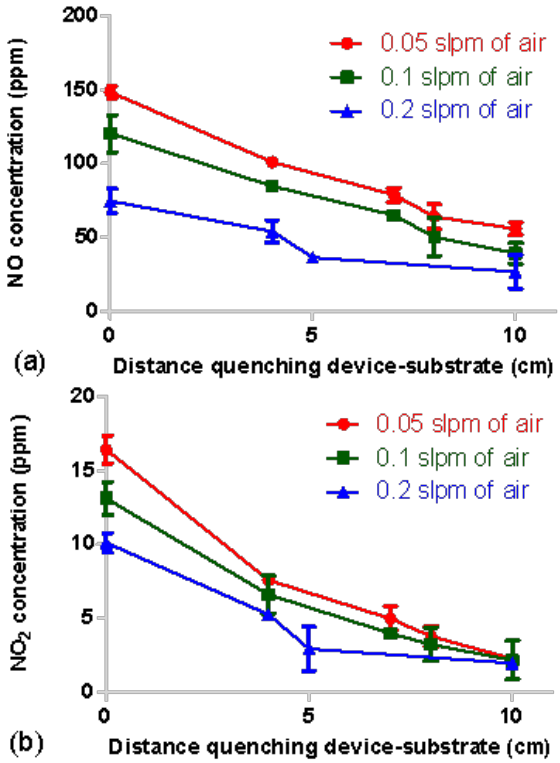

Figure.57 NO (a) and NO_2 (b) concentrations in the effluent of the ICP with quenching device as a function of axial distance for different operating conditions. The flow rate of air in the sheath gas is reported for each condition.[12]

The concentration of NO_X decreases almost linearly with the distance from the outlet of the quenching device. Measurements show that by reducing the air content in the sheath

gas there is an increase of NO_X concentration at every distance; this could be explained as a lower air content induces a higher mean temperature in the plasma [20], which could foster a higher NO_X production rate. Also, as it has been reported in section 3.2, lower concentrations of air in the plasma move the plasma core more downstream; therefore, NO_X concentrations could be higher as the relative distance between NO_X production region and measurement zone is reduced.

4. Conclusions

Results show that laminar or turbulent flow patterns can be obtained at ICP torch outlet by varying RF power and sheath gas flow rate and composition. Also nitric oxides concentration and UV irradiance can be tuned by varying sheath gas composition and substrate distance.
Using these results, the ICP torch with quenching device has been tested (500 W; central/sheath/quench gas: 2 slpm Ar/14 slpm Ar + 0.2 slpm air/35 slpm air; distance from substrate: 50 mm) on a suspension of Bacillus atrophaeus (ATCC 9372) in 0.9% NaCl, swabbed uniformly across nutrient agar plates; so achieving a suspension's bacterial density of 2.2 10^7 colony forming units (CFU) ml^{-1} quantified by dilution plating. The sample has been plasma treated for 6 minutes reaching a maximum temperature of 39°C; after 24 hours of incubation at 37°C, a circular area (diameter 35 mm) of complete growth inhibition of B. atrophaeus juxtaposed to the quenching device orifice was observed on the treated plate [11]. Further bacteria inactivation experiments have been performed and reported in [12]

References

[1] Reed T B, Journal of Applied Physics 32, 821 (1961).
[2] Boulos M I, Fauchais P, Pfender E, Thermal Plasmas, Fundamentals and Applications - Vol. 1 (Plenum press, New York, NY, 1994).
[3] Boulos M I, Pure and Applied Chemistry 68, 1007 (1996).
[4] Boulos M I, High Temperature Material Processes 1, 17 (1997).
[5] Hiroyuki T and Kazuhiro I, US2009/0186167 A1 (23 July 2009).
[6] Bottin B, Carbonaro M, Chazot O, Degrez G, Vanden Abeele D, Barbante P, Paris S, Van Der Haegen V, Magin Th, Playez M, Contributions to Plasma Physics 44, 5 (2004).
[7] Freeman R, Agnew S, Anderegg F, Cluggish B, Gilleland J, Isler R, Litvak A, Miller R, O'Neill R, Ohkawa T, Pronko S, Putvinski S, Sevier L, Sibley A, Umstadter K, Wade T and Winslow D, AIP Conference Proceedings 694, 403 (2003).
[8] Montaser A and Golightly D W (Editors), Inductively Coupled Plasmas in Analytical Atomic Spectrometry (Wiley press, New York, NY, 1992).
[9] Montaser A (Editor) Inductively Coupled Plasma Mass Spectrometry (Wiley press, New York, NY, 1998).
[10] Boselli M, Colombo V, Fridman A, Ghedini E, Gherardi M, Laurita R, Liguori A, Sanibondi P, Stancampiano A, "Device and methods for generating reactive species by means of a plasma at atmospheric pressure", WO2015019240, Università di Bologna (2015)
[11] Boselli M, Cavrini F, Colombo V, Ghedini E, Gherardi M,. Laurita R, Liguori A, Sanibondi P, Stancampiano A, Plasma Science, IEEE Transactions on **42**, 10 (2014) © 2014 IEEE

[12] Colombo V, Barbieri D, Boselli M, Cavrini F, Gherardi M, Landini M P, Laurita R, Liguori A, Stancampiano A, ”Investigation of the antimicrobial activity at safe levels for eukaryotic cells of a low power atmospheric pressure inductively coupled plasma source” submitted to Biointerphases In Focus Issue on Plasma Medicine (2015) © 2015 American Vacuum Society
[13] Boulos M I, Pure and Applied Chemistry **57**, 9 (1985)
[14] Settles G S, Schlieren and Shadowgraph Techniques: Visualizing Phenomena in Transparent Media, Springer Verlag (2001)
[15] Vaughan S, Gases and Instrumentation **1**, 3 (2007)
[16] Shimizu T, Steffes B, Pompl R, Jamitzky F, Bunk W, Ramrath K, Georgi M, Stolz W, Schmidt H U, Urayama T, Fujii S and Morfill G E, Plasma Processes and Polymers **5**, 577 (2008)
[17] Weltmann K D, Kindel E, Brandenburg R, Meyer C, Bussiahn R, Wilke C and von Woedtke T, Contributions to Plasma Physics **49**, 9 (2009).
[18] The International Commission on Non-Ionizing Radiation Protection (ICNIRP), Health Physics **87**, 171 (2004).
[19] Boselli M, Colombo V, Gherardi M, Laurita R, Liguori A, Sanibondi P, Simoncelli E, Stancampiano A, IEEE Transaction on Plasma Science, Special issue on Atmospheric Pressure Plasma Jets and their Applications **43**, 3 (2015)
[20] S. Choi, T. H. Hwang, J. H. Seo, D. U. Kim and S. H. Hong, Plasma Science, IEEE Transactions on **32**, 2 (2004)

CHAPTER 5
Atmospheric pressure non-equilibrium plasma jet: Schlieren high-speed imaging investigation

1. Introduction

Non-thermal atmospheric pressure plasma jets are rapidly gaining importance as tools for plasma processing of various types of materials because they are environmentally friendly, easy to handle and economical. The possible applications involving the use of plasma jets include thin film deposition [1], surface modification [2], wound treatment [3], sterilization [4] and nanoadditives dispersion enhancement [5]; all subjects of particular importance in the field of plasma medicine. Because of the complexity of plasma interaction with biological and thermo-sensitive materials, diagnostic analysis is unavoidable to evaluate process feasibility and to develop plasma sources optimized for specific applications. Integrated approaches relying not only the effectiveness of the plasma treatment, but also the characterization of plasma sources, are required in order to promote a multi-step optimization of the process. Consequently, the scientific community has dedicated large efforts to characterize different plasma sources for biomedical applications and to identify the most suitable diagnostic techniques [6-12].
In this work, the characterization of the outflow of a novel plasma jet device developed in our laboratory and driven by high-voltage pulses with nanosecond rise time has been carried out using a high-speed Schlieren imaging technique.
The plasma jet is a single electrode plasma jet suitable for the treatment of different substrates such as metals, polymers, glasses and biological materials (figure 58) [13]. The source has two separate gas inlets that can be fed with two different gases at the same time in order to control the composition of the plasma for the production of reactive species (ROS or RNS) or for polymerization; the primary gas is usually Ar, He or air, while the secondary one is generally O_2, N_2, air or a gas-phase monomer. In this work, since the flow rate of the secondary gas is usually much lower than that of the primary, the fluid-dynamics at the outflow has been investigated only for cases with no secondary gas. The plasma jet can be driven by different voltage waveforms, such as repetitive pulses with nanosecond or microsecond rise time or sinusoidal, triangular, square and sawtooth waveforms and it has been previously shown that this parameter strongly affects the effectiveness of the treatment [14]. In particular, in this paper only results for the plasma source driven by high-voltage pulses with nanosecond rise time will be presented.
Low speed imaging is widely adopted in the characterization of non-thermal plasma sources since it enables to identify the macroscopic aspect of the plasma discharge and to have an estimate of the length of the jet [15-16]. Conventional low speed imaging however has a limited efficacy for the description of fluid-dynamic phenomena. A qualitative and very effective study of the fluid-dynamic behaviour of a jet can be generally conducted by Schlieren imaging, which has been applied in this work to investigate fluid-dynamic instabilities, turbulence front propagation and the relative length of laminar and turbulent regions of the plasma jet. Schlieren photography has already been used to investigate turbulence in the plasma generated by different plasma jet sources: as an example, Bradley *et al* used Schlieren photography to investigate laminar and turbulent flows of a microjet generated in He on a polystyrene surface and also to determine the length of laminar and turbulent flow regions [2, 17]. However, the

works presented in literature are based on acquisitions made using common photographic cameras associated with Schlieren technique and do not allow to study the time evolution of the turbulent phenomena.
The novelty of this work is based on the use of a diagnostic setup based on the Schlieren technique coupled with a high-speed imaging camera to visualize the time evolution of the turbulence in the outflow of a plasma jet powered by a high-voltage generator with nanosecond rise time.
High-speed Schlieren imaging was used to investigate the effects of mass flow rate (Q), peak voltage (PV) and pulse repetition frequency (PRF) on the fluid-dynamics of a plasma jet propagating in the surrounding air (free flow jet) and to analyse, for the case of plasma jet impinging on a surface, the propagation of the turbulent front over substrates of different materials. This research has been performed in close collaboration with Romolo Laurita and the results presented in the following pages have been published in [18].

Figure.58 Nanosecond pulsed plasma jet operating in Ar (left) and He (right) [18]

2 Experimental and diagnostic apparatus

2.1 Nanosecond pulsed plasma jet

The plasma source used in this work is a single electrode plasma jet [19] developed in our laboratory and previously reported in [20]; a schematic of the source is presented in figure 59. The high voltage single electrode is a 19.5 mm long stainless steel sharpened metallic needle with a diameter of 0.3 mm; the electrode protrudes from a quartz capillary (outer diameter of 1 mm) by 3 mm. A peculiarity of this source is the possibility of operating with two different gas supplies at the same time. The case, made of DELRIN, presents two gas inlets to introduce a primary gas sustaining the plasma (Ar, He, Air) and to separately inject a secondary gas (O_2, N_2, gas-phase monomer). The primary gas is injected through a 12-hole (0.3 mm diameter) diffuser aimed at ensuring a uniform and laminar distribution of the primary gas flow along the electrode, while the secondary gas can be introduced through twelve 0.3 mm holes, tilted with respect to the plasma jet axis. The gas is ejected through a 1 mm orifice. Figure 60 shows the differences in jet length and radial diffusion in the surrounding air between Ar and He plasma jets at the same operating conditions. The primary gas used in this work is helium (He) with a mass flow rate (Q) of 1, 3 and 5 slpm, whereas no secondary gas was employed. In these conditions the Reynolds number of the jet

without plasma ignition is estimated to be 170, 500 and 840, respectively. The plasma source is driven by a commercial pulse generator (FID GmbH - FPG 20-1NMK) producing high voltage pulses with a slew rate of few kV/ns, a peak voltage (PV) of 7-20 kV into a 100-200 Ω load impedance and a maximum pulse repetition frequency (PRF) of 1000 Hz. A typical voltage waveforms applied to the plasma source during operation is presented in figure 61.

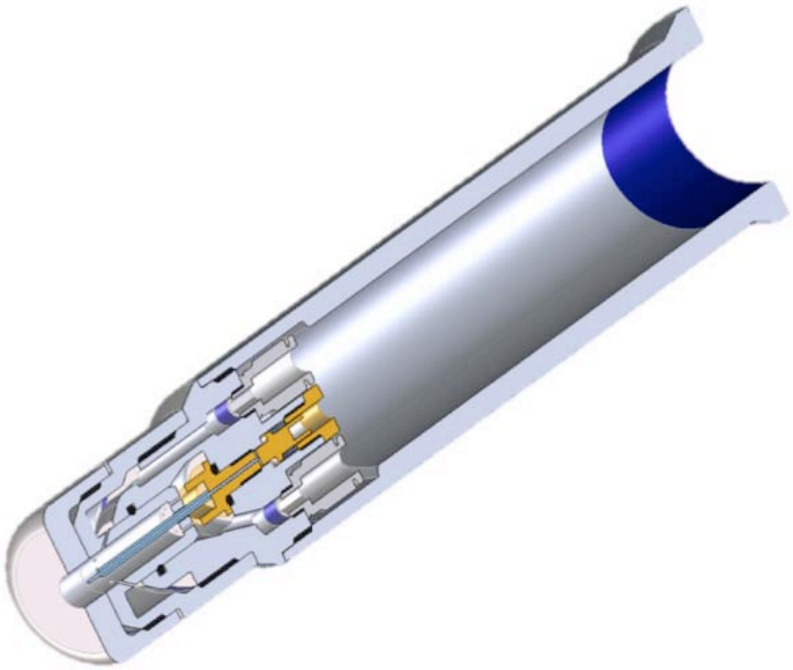

Figure.59 Three dimensional cross-section representation of the plasma source adopted in the experiments [20]

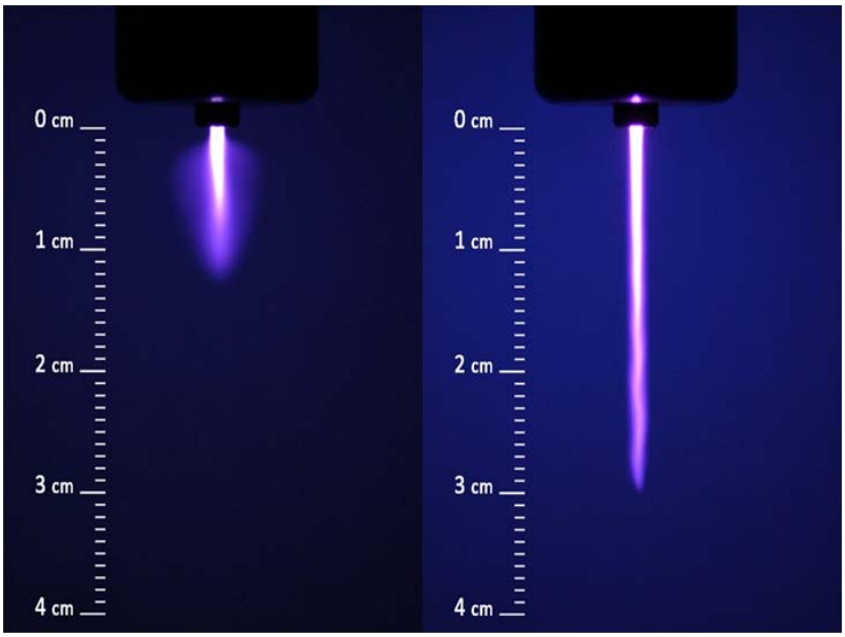

Figure.60 Low speed imaging of the plasma jet operating in Ar (left) and He (right). PV = 17 kV, PRF = 1 kHz and mass flow rate = 3 slpm [20]

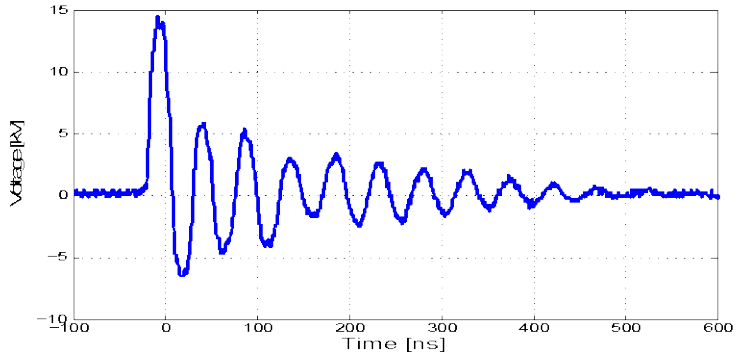

Figure.61 Typical voltage waveform applied to the plasma source during operation in with the following conditions: PV = 14 kV, PRF = 1000 Hz and He mass flow rate = 3 slpm. [18]

2.2 High-speed Schlieren imaging setup

The behaviour of the plasma jet was investigated through a Schlieren imaging setup in a Z configuration (figure 62) composed of a 450 W Ozone Free Xenon Lamp (Newport-Oriel 66355 Simplicity Arc Source), a slit and an iris diaphragm, two parabolic mirrors with a focal length of 1 m, a knife edge positioned vertically and a high-speed camera that records the Schlieren image [1].
The plasma jet has been positioned in the middle of the optical path between the two parabolic mirrors, with a vertically downward direction. A first high-speed camera (Memrecam K3R- NAC Image Technology), with a setup of 4000 fps and 1/50000 s shutter time, has been used to visualize the turbulent region of the plasma jet (results presented in section 3.1), whereas a second high-speed camera (Memrecam GX-3-NAC Image Technology), operating at 4000 fps and 1/200000 s shutter time, has been used to study the behaviour of an impinging plasma jet on different substrates (results presented in sections 3.2 – 3.5). Since the duration of the high-voltage pulse driving the plasma source is less than 500 ns and the time span for each high-speed camera frame is 0.25 ms, during the voltage pulse only one frame is recorded, which has been labelled with t = 0 ms.

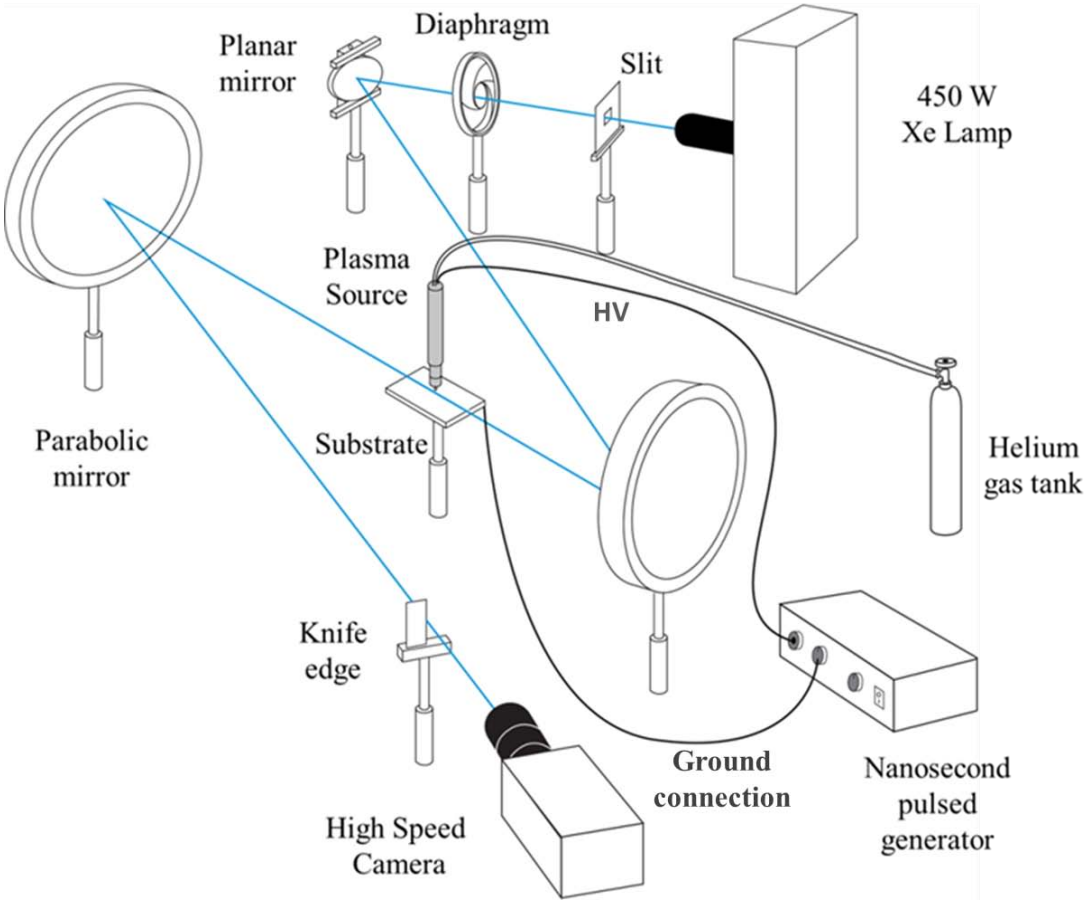

Figure.62 Experimental setup for high-speed Schlieren imaging in an impinging configuration [18]

2.3 Free flow jet and impinging configurations

The plasma jet outflow has been investigated for different substrates and for the case with no substrate. The latter configuration was defined as “free flow jet” as the jet outflow was allowed to expand freely in the surrounding ambient air. In all the other cases, the jet outflow was impinging on a substrate posed at 1.8 cm from the outlet. Three different substrates have been tested: a grounded metallic substrate made of anodized aluminium, the same grounded metallic substrate covered with a dielectric layer (PVC tape 0,15 mm thickness) and a polystyrene Petri dish (DxH 1x4 cm) which is a typical substrate adopted in biomedical studies. As shown in figure 63, for the operating conditions adopted in this paper the substrate characteristics have negligible effects on the voltage waveform applied to the electrode.

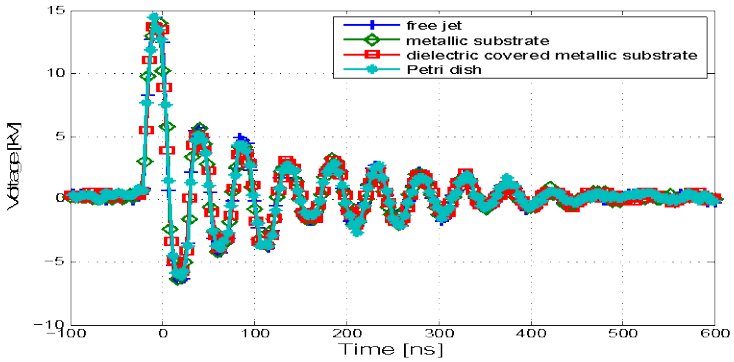

Figure.63 Comparison of the applied voltage waveform for the plasma source operating with PV = 14 kV, PRF = 1000 Hz and a He mass flow rate of 3 slpm when impinging on different substrates at a distance on 1.8 cm [18]

3 Results and discussion

Even though the random behaviour of the turbulent flow induces every acquisition set to be slightly different from any other, the overall phenomenon can be described in a repeatable way selecting frames among a wide range of results obtained for different operating conditions, varying PV, PRF, mass flow rate of the primary gas and eventual substrate materials.

A set of different plasma jet images taken with conventional camera with a few seconds of exposure time (low speed imaging) are presented for different flow rates (figure 64). A flow rate increase from 1 to 3 He slpm causes a length increase in the plasma plume, whereas a further increase up to 5 slpm results in a turbulent behaviour of the plume, due to the increased shear force between the high velocity jet and the surrounding stagnant air, that leads to a shortening of the visible plasma plume. According to [21], a jet is completely laminar for Reynolds numbers below 500. This is the case for the plasma jet presented in this work when operated with a flow rate of 1 and 3 slpm of He, corresponding to a Reynolds number of 170 and 500, respectively. When the flow rate is increased to 5 slpm, the Reynolds number falls inside a transition range (between 500 and 1000) in which the jet becomes unstable at a certain distance from the nozzle.

A direct comparison between conventional and Schlieren frames of a plasma jet in the same operating conditions is presented in figure 65. The complete propagation of

plasma jet in the surrounding air, the effective length of the laminar region and the structure of the eddies of the turbulent zone can be observed in Schlieren frames, whereas they cannot be seen in conventional photography.

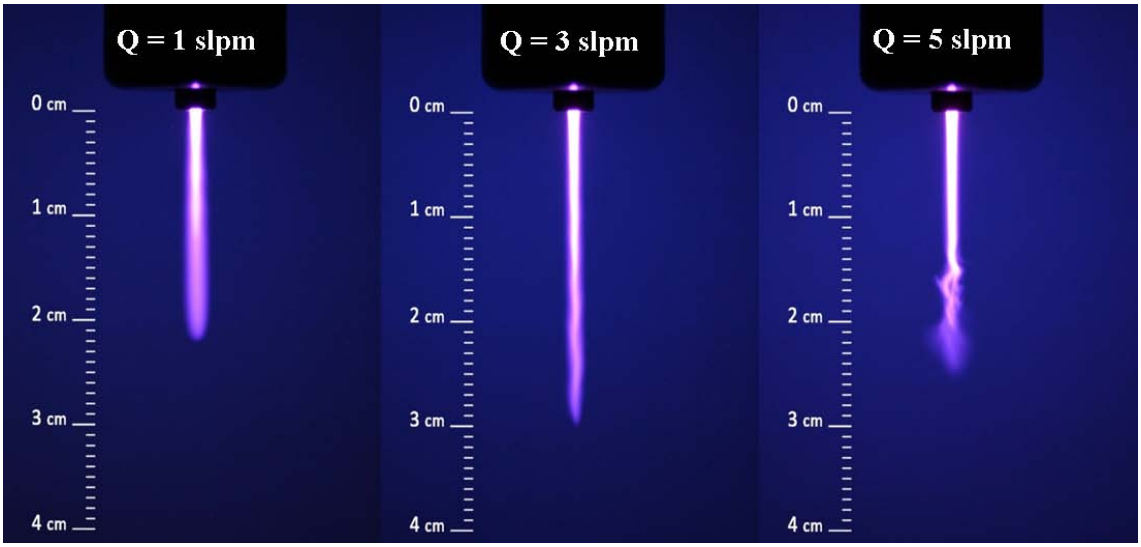

Figure.64 Low speed imaging of plasma jets generated with PRF = 1 kHz, PV = 17 kV and He mass flow rate = 1, 3 and 5 slpm, respectively [18]

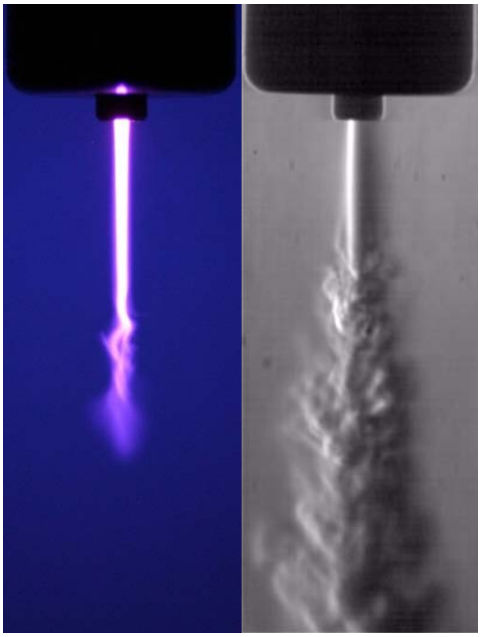

Figure.65 Conventional low speed imaging (left) and high speed Schlieren imaging (right) of a He plasma jet with PV = 17 kV, PRF = 1 kHz and mass flow rate = 5 slpm [18]

3.1 Plasma jet with no substrate (free flow jet)

In this subsection, the fluid-dynamics of the plasma jet is evaluated in free flow conditions.

In figure 66 selected frames that highlight the effects of plasma ignition on the fluid-dynamic structure of the jet are reported. For the cases with no plasma ignition (figure 66a) a transition from laminar to turbulent flow is observed when the mass flow rate is increased from 3 slpm to 5 slpm. In particular, the 3 slpm case shows a completely laminar behaviour in the acquired area, whereas in the 5 slpm case the effluent flow is characterized by a first laminar zone 1.5 cm long followed by an unstable zone with many visible eddies, due to the turbulent mixing of He with the surrounding air.
When plasma is ignited fluid-dynamic instabilities are visible also for 3 slpm, while for the 5 slpm case a length decrease of the laminar region from 1.5 cm to 0.5 cm is evinced, as shown in figure 66b.

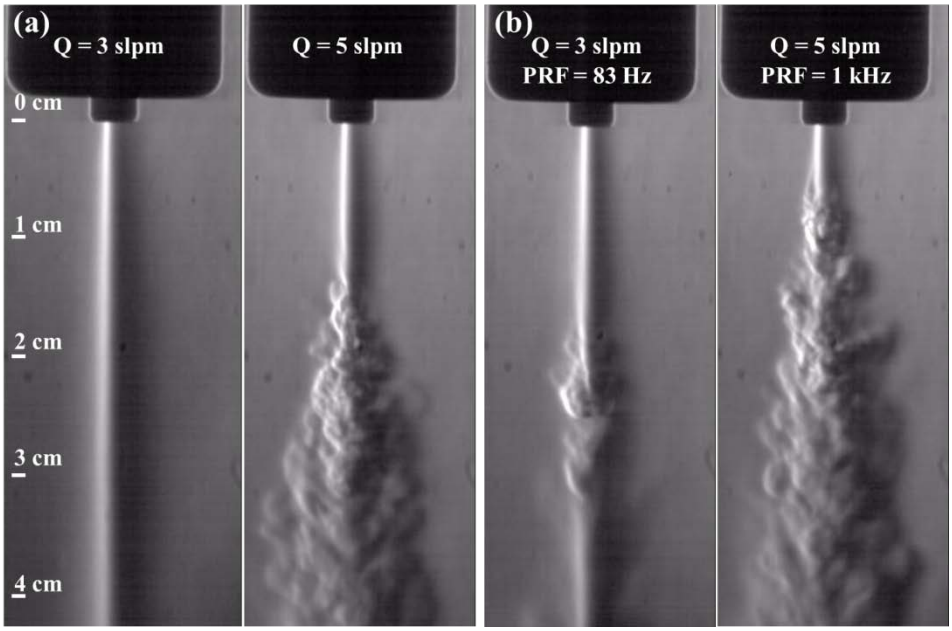

Figure.66 Schlieren imaging of effluent fluid-dynamics at two values of mass flow rate without plasma generation (a) and with plasma ignition (PV = 20 kV) in two different operative conditions (b) [18]

In figure 67, selected frames for the case with PV = 20 kV, PRF = 83.3 Hz and a He mass flow rate of 3 slpm are presented to highlight the temporal evolution of the plasma jet fluid-dynamics in the time span of two voltage pulses, which occur at t = 0 ms and t = 12 ms. At 0.5 ms before the voltage pulse, the jet is mostly laminar. After 1.5 ms from the voltage pulse, a turbulent front is observed which propagates in the downstream region of the plasma jet (see frames at t = 2.5, 5 and 7.5 ms). The observed turbulent front propagation is similar for each voltage pulse: in the frame acquired at t = 14.5 ms, which correspond to a delay of 2.5 ms after the second voltage pulse, the fluid-dynamic structure of the plasma jet is similar to that of the frame at 2.5 ms, with the formation of a turbulent front 1.5 cm downstream the nozzle.
The propagation velocity of the turbulent front along the laminar region was estimated, by analysing the high-speed Schlieren acquisitions, to be about 60 m/s, which is close to the mean gas velocity.

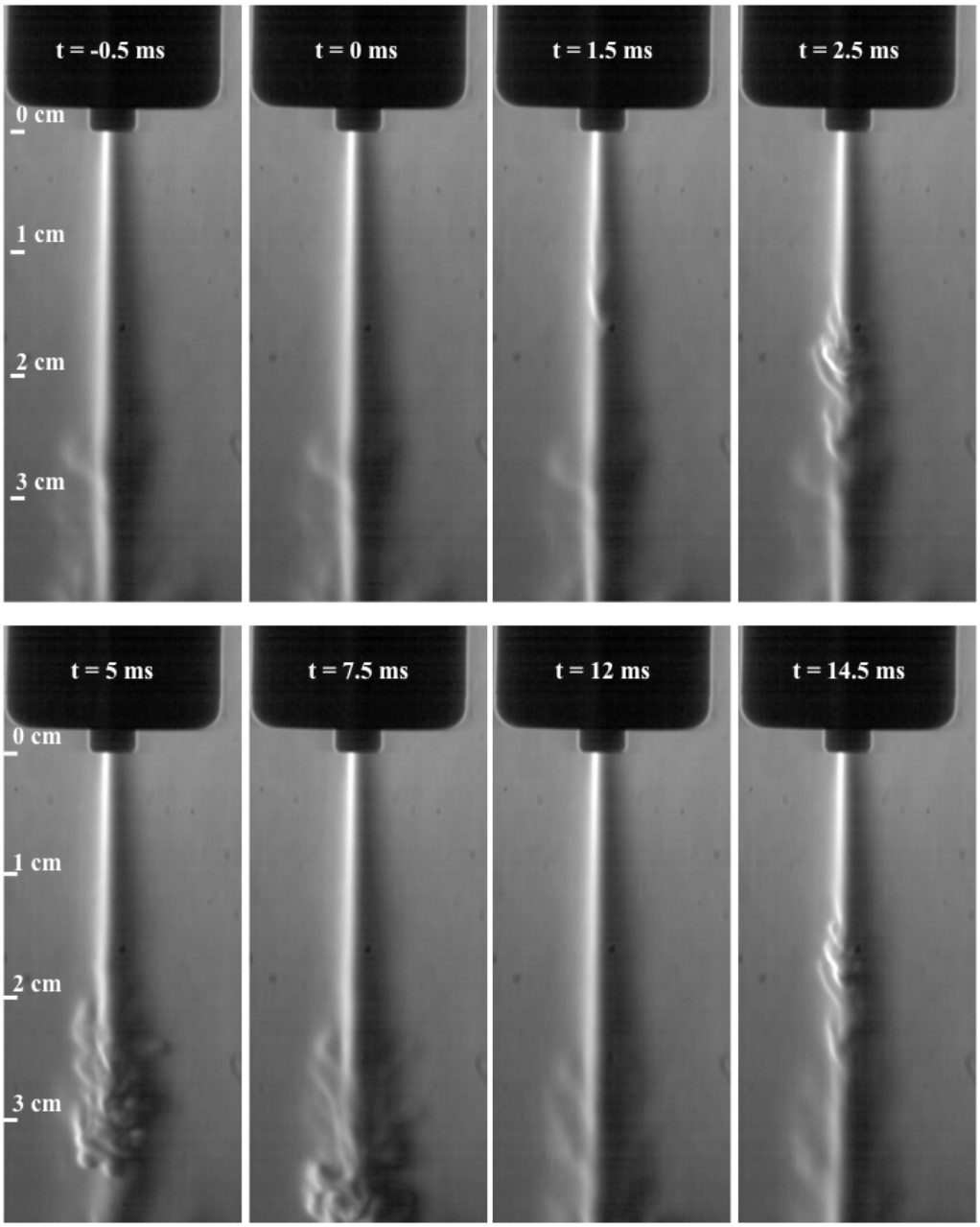

Figure.67 Schlieren imaging of the plasma jet evolution between two voltage pulses, at t = 0 ms and t = 12 ms. PV = 20 kV, PRF = 83.3 Hz and He mass flow rate = 3 slpm [18]

For a plasma jet generated with PV = 20 kV, PRF = 125 Hz and He mass flow rate = 5 slpm, the fluid-dynamic structure 0.25 ms before the voltage pulse (t = -0.25 ms) is characterized by a laminar zone that propagates 2 cm downstream the nozzle, followed by a turbulent zone (see figure 68). During voltage pulse (starting at t = 0 ms), the formation of a turbulent front inside the laminar region can be observed, with no significant change downstream the turbulent zone. The growth and the propagation of the turbulent front can be tracked in the frame sequence from t = 0.25 ms to t = 4 ms, where relevant changes in both the laminar and turbulent regions can be appreciated.

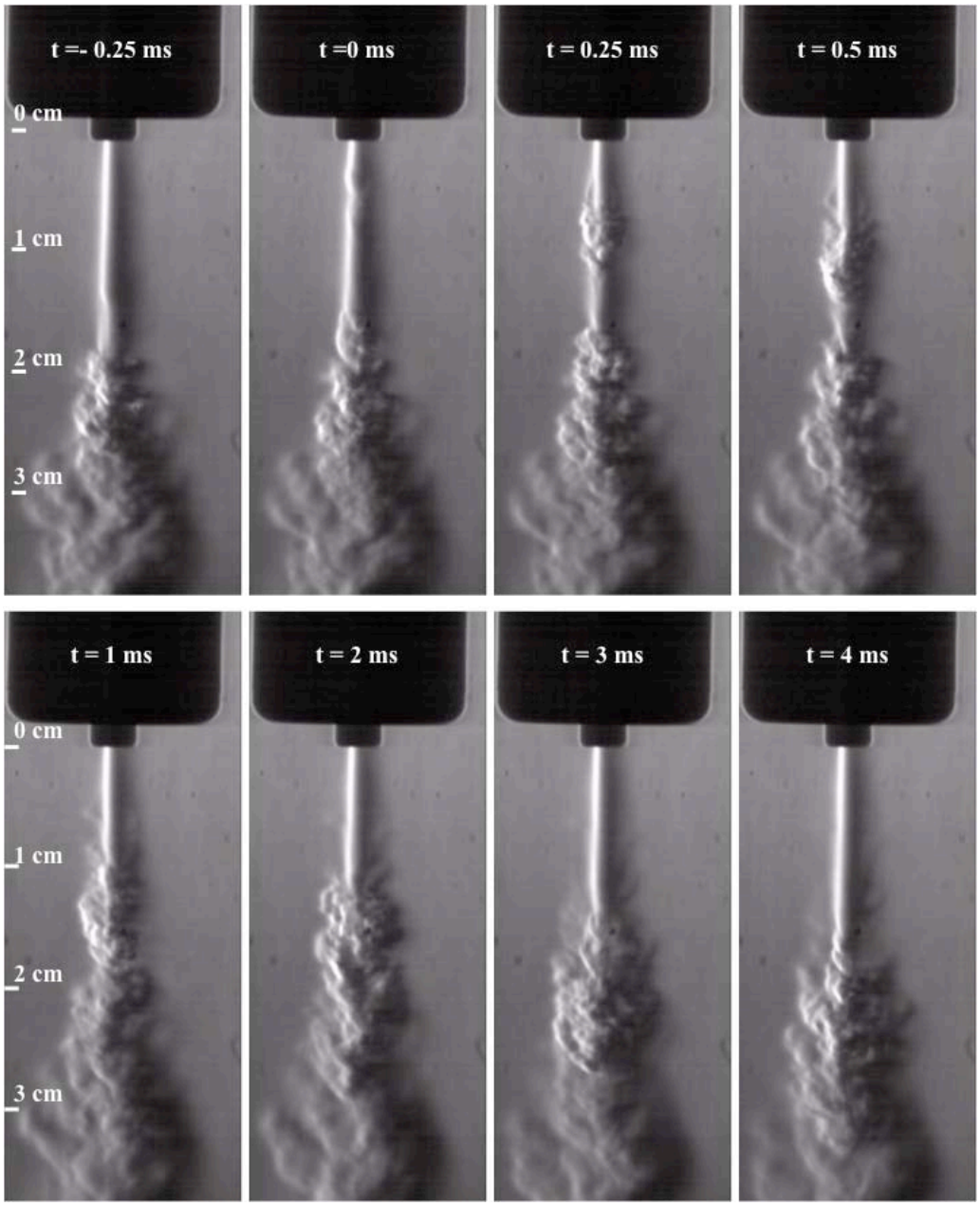

Figure.68 Schlieren imaging of the plasma jet fluid-dynamics during a voltage pulse, starting at t = 0 ms. PV = 20 kV, PRF = 125 Hz, and He mass flow rate = 5 slpm [18]

With a PRF of 1000 Hz, the time required for the turbulent front to travel along the laminar region (around 1 ms) becomes comparable with the period between voltage pulses (1 ms); in this case, no turbulent front propagation can be observed between voltage pulses: as can be seen in figure 69, the Schlieren acquisitions of the jet before (t = -0.25 ms) and after (t = 0.25 ms) the voltage pulse, which occurs at t = 0 ms, are very similar to one another. The effects of the peak voltage on the plasma jet evolution at high repetition frequency are highlighted in figures 69a and 69b. The increase of the peak voltage from 14 kV (figure 69a) to 20 kV (figure 69b) causes a shortening of the laminar region from 3 cm to 1.5 cm. Comparing different time frames in the same operating conditions, no relevant differences for the laminar region length are notable in the plasma jet fluid-dynamic structure before and after the pulse, contrary to what was observed for lower pulse repetition frequency (see figure 67and 68).

From the comparison between figure 66a (He jet with flow rate at 3 slpm but with no plasma ignition) and figure 69, it can be seen that plasma ignition with PRF at 1000 Hz induces the onset of a turbulent behaviour in the tail of the jet.

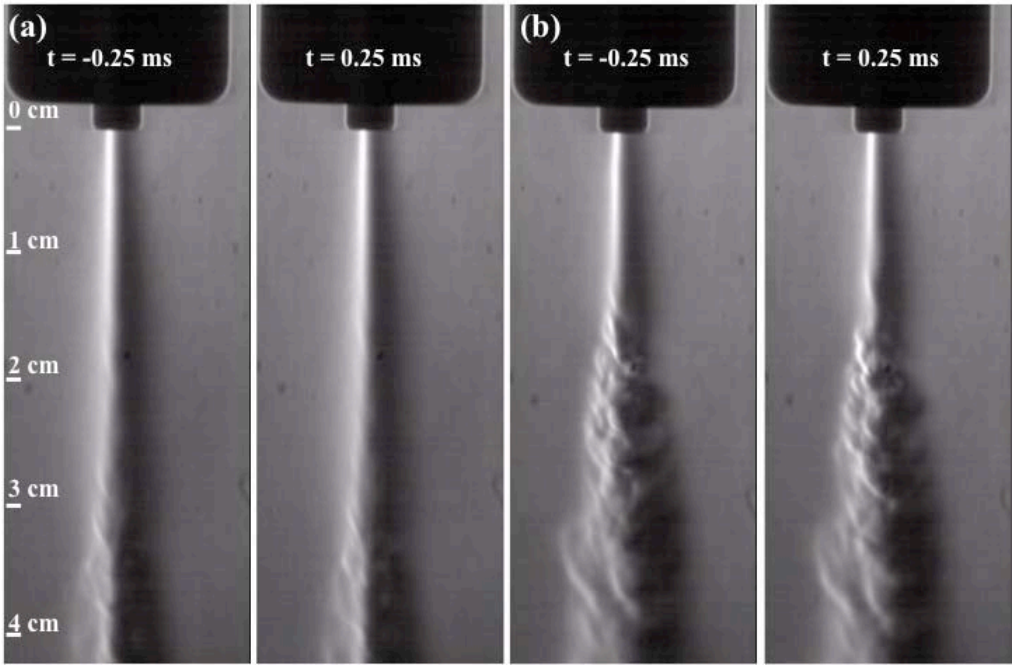

Figure.69 Schlieren imaging of the plasma jet fluid-dynamics with PV = 14 kV (a) and 20 kV (b). PRF= 1 kHz, He mass flow rate = 3 slpm. Voltage pulse at t = 0 ms [18]

3.2 Plasma jet impinging on grounded metallic substrate

The effects of plasma ignition on the fluid-dynamic behaviour of He gas jet impinging on a metallic substrate is highlighted in figure 70. For a mass flow rate of 1 slpm no great difference in the impinging region can be observed comparing the jet without and with plasma ignition (PV = 14 kV, PRF = 1000 Hz). In both cases no relevant turbulence can be observed. For a He mass flow rate of 3 slpm, a slight turbulent behaviour in the external fringes for the case with no plasma can be observed, mainly due to the buoyancy effect of He. More relevant fluid-dynamic instabilities can be seen in the impinging region when plasma is ignited.

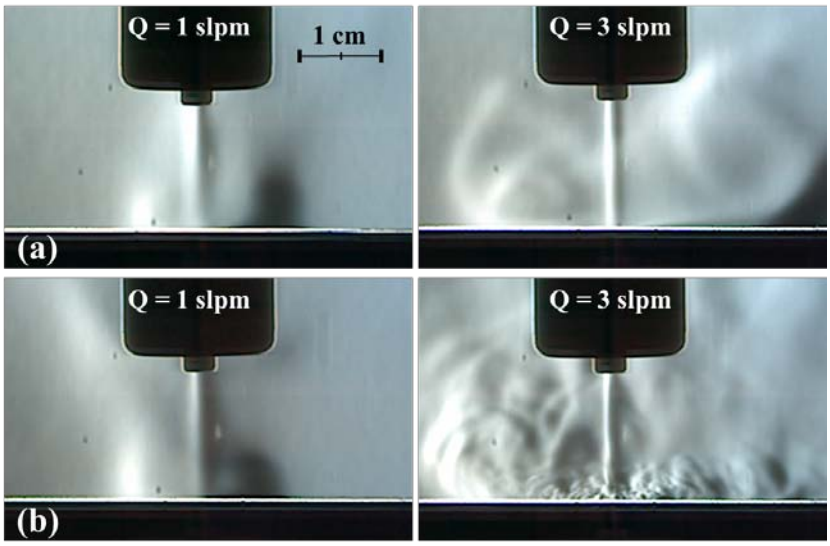

Figure.70 Schlieren imaging of a jet impinging on a metallic substrate without (a) and with (b) plasma ignition. He mass flow rate set at 1 slpm (left) and 3 slpm (right). PV = 14 kV and PRF = 1 kHz [18]

Reducing the PRF to 125 Hz (PV = 14 kV, He mass flow rate = 3 slpm), it is possible to track the propagation of a turbulent wave front along the substrate surface (see figure 71). At t = 0 ms, corresponding to the voltage pulse, no turbulent front over the metallic substrate is visible. The turbulent wave front becomes visible 1 ms after the voltage pulse and it propagates along substrate surface; after 3 ms the turbulent wave front has propagated 0.75 cm from the jet axis.

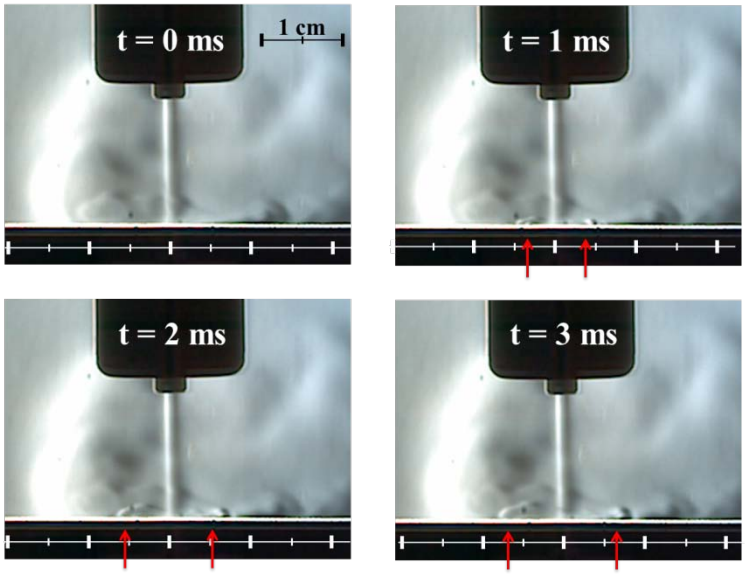

Figure.71 Propagation of turbulent wave fronts (see red arrows) induced by a plasma jet impinging on a metallic substrate. PV = 14 kV, PRF = 125 Hz, He mass flow rate = 3 slpm. Voltage pulse at t = 0 ms. [18]

3.3 *Effects of dielectric layer covering the metallic substrate*

To evaluate the influence of the material of the substrate on the fluid-dynamic characteristics of the plasma jet at the impinging region, Schlieren frames at 0, 0.5 and 1 ms after the voltage pulse are presented for a metallic substrate (figure 72a) and a metallic substrate covered with an insulating layer (figure 72b1 and 72b2). A drastic reduction in turbulent behaviour of the plasma jet at the impinging region can be observed passing from a metallic to a dielectric substrate. For the cases with dielectric substrate, the flow is almost laminar and the time scale of fluid-dynamic instabilities is much longer (several ms) than for the cases with turbulent behaviour (less than 1 ms): for this reason, frames at 0, 0.5 and 1 ms after the voltage pulse acquired during the same recording are very similar to one another (figure 72b1). However, with a higher peak voltage (17 kV) the occurrence of turbulent wave fronts with a time scale of less than 1 ms is observed also for the case with plasma jet impinging on the dielectric covered substrate (figure 72b2).

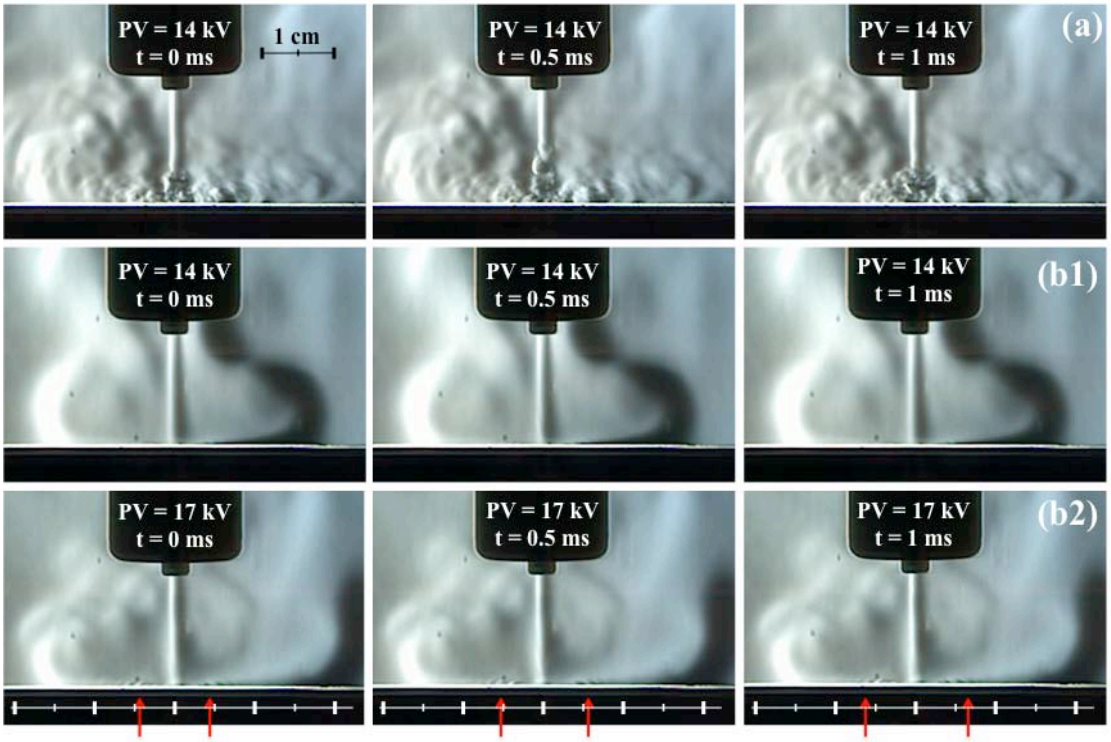

Figure.72 Schlieren imaging of the plasma jet fluid-dynamics without (a) and with (b1, b2) a layer of dielectric material on the surface of a metallic substrate. PV at 14 kV (a, b1) and 17 kV (b2), He mass flow rate = 3 slpm, PRF = 1 kHz. Turbulent wave fronts are tracked by red arrows. Voltage pulse at t = 0 ms. [18]

3.4 Plasma jet impinging on a petri dish

Schlieren frames of the plasma jet impinging on a Petri dish have been reported in figure 73 for two different He mass flow rates (3 slpm and 5 slpm, left and right columns respectively), with and without plasma ignition. In these conditions, the helium flow impinges on the Petri dish and it is subsequently directed upward mainly as a consequence of the buoyancy effect and of the presence of the Petri walls that obstruct the sideway gas flow. For the case with no plasma ignition, since the Schlieren frames at different time steps were very similar to one another, only one frame has been reported in figure 73a1 and 73a2. With plasma ignition, for the case at 3 slpm a flow

motion can be seen in the region outside the plasma jet on a time scale of few hundreds ms (see figure 73b1); with a flow rate of 5 slpm (see figure 73b2), a fluid-dynamic instability can be seen in the jet region in frames at t = 0 ms and t = 25 ms, which is characterized by a time scale of less than 1 ms, whereas turbulence in the surrounding atmosphere above the Petri dish is characterized by a time scale of tens of milliseconds.

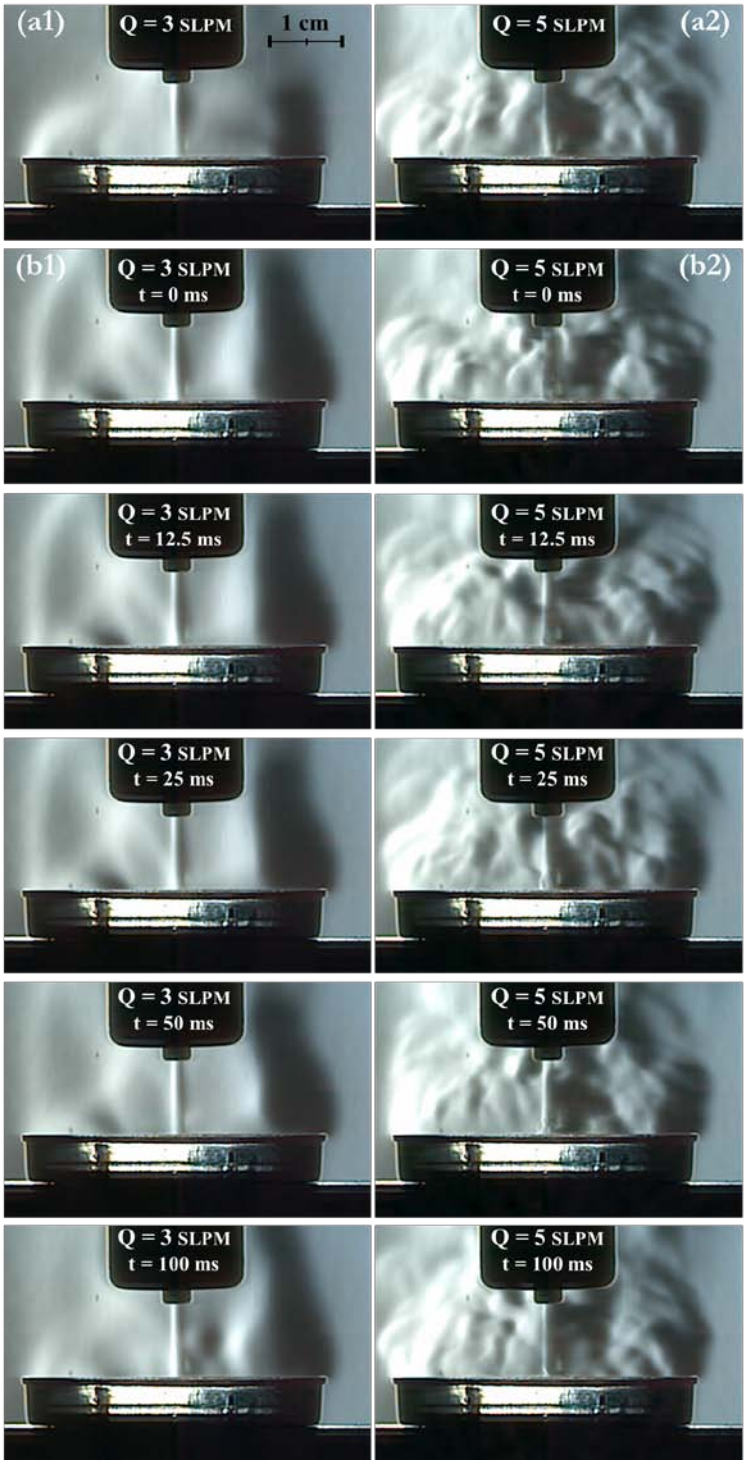

Figure.73 Schlieren imaging of the fluid-dynamics of a jet impinging on a petri dish with He mass flow rate of 3 slpm (a1,b1) and 5 slpm (a2,b2) without (a1,a2) and with plasma ignition (b1,b2). PV = 14 kV, PRF = 1 kHz. [18]

4 Discussion

The results presented in section 3 have shown that plasma ignition triggers the formation of a turbulent front which propagates along the jet; also, the onset of turbulence induces the reduction of the jet laminar region when the period between subsequent voltage pulses is comparable with time required for the turbulent front to propagate along the laminar region of the jet (about 1 ms).
A reduction of the laminar region length due to plasma ignition has been already observed for other plasma jets driven by AC voltage waveforms and nanosecond pulses [17, 22, 23].
The mechanism responsible for the formation of a turbulent front in correspondence of the high-voltage pulse is still poorly understood; possible mechanisms include gas heating, local pressure increase, variation of transport properties of gas or momentum transfer between ions and neutrals. Gas heating during the voltage pulse can induce the reduction of gas density, which in turn results in a localized increase of gas velocity; a pressure peak can also take place near the powered electrode during the voltage pulse as a consequence of local ionization, with a subsequent increase of jet velocity; also, the variation of the transport properties of gas (especially viscosity) in presence of ionized species during the pulse can result in a gradient of gas velocity and in the formation of a turbulent front; finally, when the structure of the plasma jet is characterized by plasma bullets, which are travelling with a velocity of several km/s [19], turbulence onset can be linked to momentum transfer between ions and neutrals.
For dielectric barrier plasma jets [23] it has been concluded that the key mechanism leading to reduction of the laminar region after plasma ignition is gas heating, which in turn induces an increase in gas velocity.
In our experiments it was possible to measure the propagation velocity of the turbulent front, which has been found to be in the same order of magnitude as gas velocity (between 20 and 100 m/s). For this reason, in this plasma jet it can be excluded a correlation between turbulent front propagation and the generation of plasma bullets. However, further investigations are needed to understand the relative importance of the suggested mechanisms.
Results in section 3 have shown that, for the cases with jet directed towards a substrate, a turbulent front is propagating along substrate surface starting from the jet impinging point; this effect is more pronounced in the case of a metallic substrate with respect to the case with a dielectric covered metallic substrate. Indeed, since the adopted plasma source is a single electrode plasma jet, the substrate acts as a counter electrode and in the case of dielectric covered substrate the current is self-limited by charge deposition on the dielectric surface; this induces a less intense discharge with respect to the case with bare grounded electrode and consequently less intense turbulence in the jet.

5 Conclusions

The fluid-dynamic behaviour of a single electrode non-equilibrium plasma source driven by high voltage pulses with nanosecond rise time at atmospheric pressure has been characterized with a high-speed Schlieren imaging technique. This study is a first step in a multi-stage integrated approach that relies on diagnostics and experiments for the tailoring of the plasma source to specific applications, among which also biomedical ones.

The use of high-speed Schlieren technique has allowed us to observe several phenomena for the first time. Plasma ignition causes fluid-dynamic instabilities that are moving in the direction of the jet flow and are correlated with the high-voltage pulses: for low pulse repetition frequency (<125 Hz) it is possible to track the movement of the turbulent front between two voltage pulses, whereas for higher pulse repetition frequency (1000 Hz) the flow is completely characterized by turbulent eddies in the effluent region without relevant changes between the voltage pulses.
Moreover, fluid-dynamic characteristics of the plasma jet at the impinging region for metallic and insulating substrates and the turbulent propagation front have been observed. Turbulent eddies, more visible with the metallic substrate than with the insulating one, propagate over the surface starting from the gas impinging zone.
The results presented in this paper will serve as a basis for the design, optimization and analysis of plasma processes for treatment of biological and biocompatible materials, in which the plasma jet can be used as a source of chemical reactive species, whose generation and transport can be strongly influenced by turbulence.

References

[1] Ito Y, Urabe K, Takano N and Tachibana Kv Appl. Phys. Express **1** 067009 (2008)
[2] Olabanji O T and Bradley J W, Plasma Process. Polym. **9** 929-36 (2012)
[3] Nastuta A V, Topala I, Grigoras C, Pohoata V and Popa G, J. Phys. D: Appl. Phys. **44** 105204 (2011)
[4] Fridman G, Friedman G, Gutsol A, Shekhter A B, Vasilets V N and Fridman A, Plasma Process. Polym. **5** 503-33 (2008)
[5] Colombo V, Fabiani D, Focarete M L, Ghedini E, Gherardi M, Gualandi C, Laurita R, Sanibondi P, Zaccaria M, Proceedings of the 11th IEEE International Conference on Solid Dielectrics - ICSD 11, Bologna, Italy, June 30 – July 4, 2013 (2013)
[6] Weltmann K D, Kindel E, Brandenburg R, Meyer C, Bussiahn R, Wilke C and von Woedtke T, Contrib. Plasma Phys. **49** 631-40 (2009)
[7] O'Neill F T, Twomey B, Law V J, Milosavljevic V,Kong M, Anghel S D, and Dowling D, IEEE Trans. Plasma Sci. **40** 2994-3002 (2012)
[8] Deng X L, Nikiforov A Y, Vanraes P and Leys C, J. Appl. Phys. **113** 023305 (2013)
[9] Xiong Q, Nikiforov A Y, Li L, Vanraes P, Britun N, Snyders R, Lu X P and Leys C, Eur. Phys. J. D **66** 281 (2012)
[10] Hong Y, Lu N, Pan J, Li J, Wu Y and Shang K F, J. Electrostatics **71** 93-101 (2013)
[11] van Gessel A F H, Hrycak B, Jasinski M, Mizeraczyk J, van der Mullen J J A M and Bruggeman P J, J. Phys. D: Appl. Phys. **46** 095201 (2013)
[12] Xiong Q, Nikiforov A Y, Gonzalez M A, Leys C and Lu X P, Plasma Sources Sci. Technol. **22** 015011 (2013)
[13] Boselli M, Colombo V, Ghedini E, Gherardi M, Laurita R, Liguori A, Marani F, Sanibondi P, Stancampiano A, Proceedings of 21st International Symposium on Plasma Chemistry – ISPC21, Cairns, Australia, 4 - 9 August 2013 (2013)
[14] Colombo V, Ghedini E, Gherardi M, Laurita R, Sanibondi P, Fabiani D, Zaccaria M, Focarete M L and Gualandi C, Proceedings of 11th IEEE International Conferences on Solid Dielectrics - ICSD 11, Bologna, Italy, June 30th – July 4th 2013 (2013)

[15] Shao T, Long K, Zhang C, Yan P and Zhang S, J. Phys. D: Appl. Phys. **41** 215203 (2008)
[16] Ayan H, Fridman G, Gutsol A F, Vasilets V N, Fridman A and Friedman G, IEEE Trans. Plasma Sci. **36** 504-8 (2008)
[17] Oh J S, Olabanji O T, Hale C, Mariani R, Kontis K and Bradley J W, J. Phys. D: Appl. Phys. **44** 155206 (2011)
[18] Boselli M, Colombo V, Ghedini E, Gherardi M,. Laurita R, Liguori A, Sanibondi P, Stancampiano A, Plasma Chem Plasma Process, **34** 4 (2014) © 2014 Springer International Publishing AG
[19] Lu X, Laroussi M, Puech V, Plasma Sources Sci. Technol. **21** 034005 (2012)
[20] Colombo V, Fabiani D, Focarete M L, Gherardi M, Gualandi C, Laurita R, Zaccaria M, Plasma Process. Polym. **11** 3 (2014)
[21] Ungate C D, Harleman D R, Jirka G H, Stability and mixing of submerged turbulent jets at low Reynolds numbers, MIT Energy Lab. (1975)
[22] Folletto M, Douat C, Fontane J, Joly L, Pitchford L, Puech V, Proceedings of 31th International Conference on Phenomena in Ionized Gases - ICPIG, 14-19 Jul 2013, Granada, Spain. (2013)
[23] Ghasemi M, Olszewski P, Bradley J W and Walsh J L, J. Phys. D: Appl. Phys. **46** 052001 (2013)

Acknowledgements

Activities presented in this thesis have been performed into the framework of research contracts with companies such as Umicore Research (B), AirLiquide-CTAS (F) and Cebora (IT) within the activities of the Research Group for Industrial Applications of Plasmas of University of Bologna; for the activities of chapters 4 and 5 also with the contribution of AlmaPlasma S.r.l.. They have also been performed into the framework of FP7-NMP European project SIMBA "Scaling-up of ICP technology for continuous production of Metallic nanopowders for Battery Applications", European networking projects MPNS COST Action MP1101 "Bio-Plasma - Biomedical Applications of Atmospheric Pressure Plasma Technology" and MPNS COST Action TD1208 "Electrical discharges with liquids for future applications".

To the people that supported me in all these years: thanks, I owe you one